

Handheld Optoacoustic Probe Facilitating Nearfield Investigations Through a Transparent Detector

Von der Fakultät für Mathematik und Physik
der Gottfried Wilhelm Leibniz Universität Hannover

zur Erlangung des Grades
Doktor der Naturwissenschaften
Dr. rer. nat.

genehmigte Dissertation von

M.Sc. Elias Möller

geboren Blumenröther am 15.05.1987 in Gießen

2020

Referent: Prof. Dr. Bernhard Roth - Hannoversches Zentrum für optische Technologien

Korreferent: Prof. Dr. Uwe Morgner - Institut für Quantenoptik

Tag der Promotion: 23.10.2020

LEIBNIZ UNIVERSITÄT HANNOVER

DOCTORAL THESIS

Handheld Optoacoustic Probe Facilitating
Nearfield Investigations Through a
Transparent Detector

Author:
Elias MÖLLER

Supervisor:
Prof. Bernhard ROTH

*A thesis submitted in fulfillment of the requirements
for the degree of Dr. rer. nat.*

in the

Hannoversches Zentrum für optische Technologien

October 2020

Declaration of Authorship

I, Elias MÖLLER, declare that this thesis titled, 'Handheld Optoacoustic Probe Facilitating Nearfield Investigations Through a Transparent Detector' and the work presented in it are my own. I confirm that:

- This work was done wholly or mainly while in candidature for a research degree at this University.
- Where any part of this thesis has previously been submitted for a degree or any other qualification at this University or any other institution, this has been clearly stated.
- Where I have consulted the published work of others, this is always clearly attributed.
- Where I have quoted from the work of others, the source is always given. With the exception of such quotations, this thesis is entirely my own work.
- I have acknowledged all main sources of help.
- Where the thesis is based on work done by myself jointly with others, I have made clear exactly what was done by others and what I have contributed myself.

Signed:

Date:

"There's a lot of difference between listening and hearing."

G.K. Chesterton

Abstract

Handheld Optoacoustic Probe Facilitating Nearfield Investigations Through a Transparent Detector

Modern medicine relies strongly on measurement devices, enabling the physician to investigate the human body in ever greater detail. In addition to established techniques of optical microscopy, ultrasound, x-ray and magnetic resonance imaging, optoacoustic (OA) imaging is on its path to enter the clinics. The research field of optoacoustics already produced a variety of remarkable setups, from high resolution microscopy to deep penetrating tomography. Through the broad range of wavelengths available for this technique, it is capable of detecting the concentration of endogenous as well as exogenous contrast agents, even blood oxygenation levels can be determined in real time. Depending on the application, different OA setups can be created, customized to best address the specific task.

This thesis is concerned with the development of a handheld optoacoustic setup to determine the thickness of melanoma. Penetration depth is the most important factor in staging of skin tumors. To facilitate near field measurements the detector is designed to be transparent, which allows illumination through the detector. Indium tin oxide electrodes are sputtered on a piezoelectric polymer film to create a circular detector area. Transparency was confirmed using spectrophotometric measurements in the visible and near infrared light spectrum. To characterize the capabilities of the transparent detector, far field measurements on hydrogel samples with layers containing different concentrations of melanin were performed. An OA measurement series on a mole under laboratory conditions showcased the possibility using wavelengths in the range from 432-652 nm with this detector. For logistical reasons, only 532 nm were used in the other measurements.

Near field measurements on a coated glass plate are compared with simulation, confirming the validity of the data processing algorithm to remove the pyroelectric signal and deconvolve the instrument response function from the OA signal. In a small clinical study, suspicious nevi were investigated using the setup developed here. The obtained OA signals are discussed in relation with the histology of the respective nevus. Even though their thicknesses could not yet be determined reliably, the results are promising that further improvements with regards to noise reduction will allow real time measurements of the absorption depth profile.

Keywords: Handheld Optoacoustic Probe, Single Transparent Detector, PVA Hydrogel Preparation, Optoacoustic Near Field Measurements.

Acknowledgements

Ich danke Bernhard Roth für das Ermöglichen dieser Promotion, sowie Uwe Morgner für seine Arbeit als Prüfer. Merve Wollweber gilt mein Dank für die wissenschaftliche Betreuung in den ersten Jahren des Projektes. Arthur, Maik, Jenny und Mikhail danke ich für all die Stunden in den MeDiOO-Meetings, die dabei aufgekommene Auswahl an Diskussionsthemen ist kaum zu übertreffen. Oliver Melchert hat sich durch seine Simulationen in dieser Arbeit verewigt, jedoch werde ich mich vor Allem an diese eine Nacht zu zweit in Paris erinnern. Martin und Sebastian waren ausgezeichnete Kollegen mit denen jeder Mensagang zu einer wahren Currywurstsause wurde. Meinem kleinen fleißigen Masterranden, Jonas, welcher längst kein Masterrand mehr ist, danke ich für die produktive Zusammenarbeit und die zu meiner unterschiedlichen Perspektive. Weiterer Dank gebührt Max und Maher für die Unterstützung bei der Herstellung der Phantome und das Kleben der Folien. Den restlichen HOT-Mitarbeitern danke ich für die netten Jahre, insbesondere Vera und Gabi welche eine positive Konstante in manch turbulenter Zeit darstellten. Meiner Familie und Freunden danke ich dafür, dass sie nicht allzu oft nach dem Stand der Arbeit gefragt haben. Abschließend danke ich Janni, für ein gemeinsames Leben in dem selbst Jammern auf höchstem Niveau aufwändiger Recherche und Vorbereitung bedürfte.

Contents

1	Introduction	1
2	Background	7
2.1	Optoacoustics	8
2.1.1	The Optoacoustic Effect	9
2.1.2	State-of-the-Art	12
2.2	Skin	18
2.3	Melanoma	21
2.4	The MeDiOO Project	23
2.5	Safety and Ethics	27
3	Theory	29
3.1	Generation of OA Signals	29
3.2	Acoustic Near and Far Field	32
3.3	Influence of the Beam Profile on the OA Signal	36
3.3.1	Acoustic Reflection	39
3.4	Signal Deconvolution	40
4	Material and Methods	43
4.1	Polyvinyl alcohol Hydrogel Phantoms	44
4.1.1	PVA Hydrogel Preparation	45
4.1.2	Phantom Preparation	48
4.2	Transparent Ultrasound Transducer	49
4.2.1	Piezo- and Pyroelectric Effect in PVDF	50
4.2.2	Detector Design and Fabrication	51
4.2.2.1	Active Area	53
4.3	Optoacoustic Setup	55
4.3.1	Electrical Preamplifier	55
4.3.2	Energy Calibration and Monitoring	56
4.3.3	Beam profile	59
4.3.4	Optoacoustic Measurement Setup	60
4.3.5	Detector Setups	61
4.4	Signal Processing	64
4.4.1	Subtraction of Electromagnetic Noise	64
4.4.2	Removal of the Pyroelectric Signal	65

5	Results and Discussion	69
5.1	Layered Phantoms	70
5.1.1	Far Field Measurements of Multiple Layers	70
5.1.2	Investigation of Angular Dependence of OA Signals (Angular Study)	74
5.2	Analysis of the Pyroelectric Effect	76
5.3	Deconvolution With IRF - Ink On Glass	80
5.4	OA Measurements on Human Skin	84
5.4.1	OA Wavelength Scans	84
5.4.2	Clinical Measurements	88
6	Conclusion and Outlook	103
A	Clinical Measurements	
	using the SYM Detector Setup	107
A.1	W2-2-1	108
A.2	W2-2-2-1	110
A.3	W2-2-2-2	111
A.4	W2-3-1	112
A.5	W2-3-2	113
A.6	W2-4-1	114
A.7	W2-4-2	116
A.8	W2-5-1	117
A.9	W2-5-2	119
A.10	W3-2-1-1	120
A.11	W3-2-1-2	121
A.12	W3-2-2-1	122
A.13	W3-2-2-2	123
A.14	W3-3-1	124
A.15	W3-3-2-1	125
A.16	W3-3-2-2	126
B	Appendix	127
B.1	Non Beer-Lambert Pressure Profiles	127
B.2	Surface waves	128

Abbreviations

DAC	Data Acquisition Card
(HF)US	(High Frequency) Ultrasound
MPE	Maximum Permissible Exposure
OA(s)	Optoacoustic(s)
OCT	Optical Coherence Tomography
OPO	Optical Parametric Oscillator
PVA(H)	Polyvinyl alcohol (Hydrogel)
PVDF	Polyvinylidene fluoride
PMMA	Polymethylmethacrylat
Pyro	Pyroelectrical effect or signal
ITO	Indium Tin Oxide
ZTO	Zinc Tin Oxide

Chapter 1

Introduction

In the year 2018, worldwide, approximately 60 thousand people died from malignant melanoma [Bra18], also known as black skin cancer. With an overall mortality rate of 20% malignant melanoma are very dangerous [Mac11]. A main cause for melanoma is intensive UV radiation at a young age, especially on sensitive skin. The highest prevalence occurs in white populations living in regions with high sun exposure. A prime example is Australia, where 4-5% of men and 3-4% of all women develop melanoma in their lifetime [Int14]. In regions of lower sun exposure, excessive use of tanning beds and intensive sunbathing during summer vacations in southern countries has been attributed to the rise in incidence rates [Int14]. Even though these risk factors have been known for decades, certain life styles and the social ideal of beauty equating tanned skin with health often counteract preventive measures.

Once a melanoma has formed, early discovery is key to a successful treatment. In the early stages of the cancer, the chances of a full recovery are very high (five-year survival rate >95% [Wan11]). However, if the tumor has grown far enough into the skin to metastasize the survival rate drops significantly [Fri85]. Dermatologists are trained to recognize certain characteristics distinguishing malignant melanomas from benign moles. However, since these assessment criteria can only be applied to the visible features of the lesion, manifestations in deeper regions of the skin can be missed. To reduce the risk of missing a potentially lethal skin alteration, suspicious nevi are removed surgically. From the histopathological examination of the excised tissue, the maximal penetration depth is inferred; this is the single most important variable for the staging of melanoma [Wan11].

On one hand, if the thickness could be determined without excision, it would reduce the number of needless operations. On the other hand, if the operation is necessary, knowledge of the precise penetration depth can be used to decide on the safety margins kept during the surgery, to ensure that all the afflicted tissue is removed already during the first excision.

Various techniques have been considered to offer noninvasive means to investigate the extent of the depth infiltration of skin cancer. Optical methods such as confocal microscopy and optical coherence tomography are capable of resolving structures of a few micrometers in size. Confocal microscopy is even capable of resolving tissue structures with cellular resolution [Raj95]. However, the long measurement duration of more than 5 minutes for a single lesion [Pel07], in combination with the a maximum penetration depth of 350 μm at a wavelength of 1064 nm [Raj99], limits the practicality of using confocal microscopy as a standard tool for melanoma detection. By comparison, modern optical coherence tomography systems, are capable of creating 3-dimensional images with micrometer resolution within less than a minute.

In general, the penetration depth of optical methods is limited by the strong scattering occurring in skin. In contrast, ultrasound waves can travel through several centimeters of living tissue without significant attenuation. Ultrasound devices, such as those commonly used in prenatal care, work with frequencies in the low megahertz range, which allows deep penetration but limited resolution. High frequency ultrasound systems, specifically designed for dermatology, allow high resolution while still maintaining a high penetration depth relative to optical techniques. With a 75 MHz system, a 3 mm penetration depth and a lateral resolution of 21 μm has been achieved [Gui08]. The contrast mechanism in ultrasound imaging originates from changes in the acoustic properties, which cause reflections. Regarding melanoma detection, this contrast is low, due to similar acoustic properties of regular and pigmented skin.

Optoacoustics (OAs) combines optical contrast with acoustic resolution. Discovered in 1880 by Alexander Graham Bell, the optoacoustic effect describes the creation of pressure waves by altering the radiation intensity absorbed by the sample. The phenomenon has experienced a renewed interest since the adoption of powerful pulsed lasers in the 1960s. While in the beginning the field of optoacoustics was mainly confined to gas spectroscopy, its focus has now shifted toward biomedical applications. In the last few

decades, groundbreaking progress in the fields of optoacoustic endoscopy, microscopy and small animal tomography followed. Using fiber-based illumination, endoscopes can be built which are capable of producing, for example, a 100° image, demonstrated on a rabbit colon in [Li14]. OA microscopy can create images of living tissue with a lateral resolution of a few micrometer [Hai14],[Haj15]. By realizing a system which utilizes the pump-probe technique to enhance the axial resolution beyond the bandwidth limitations of the transducer, single bovine erythrocytes can be resolved [Mat14].

One of the unique features of OAs is the large range of wavelengths that can be used. Even without labeling, high contrasts can be achieved through a multitude of intrinsic optical absorption agents, i.e., melanin, hemoglobin, carotene, and so on. Due to the large bandwidth of wavelengths available for use in OAs, individual absorber concentrations can be determined. Most prominent is the example of the differentiation between oxygenated and deoxygenated blood [Li14],[Yao13],[Zha06],[Tzo16]. Even more impressive are results from an OA microscope, which not only produces high resolution images but also yields information like blood oxygenation, vessel diameter, and even blood flow [Nin15].

In optoacoustics, the resolution of a measurement device is defined by the precision with which the origin of the pressure wave can be determined. Only regions which are both in the path of the optical irradiation as well as in the field of view of the acoustic detector contribute to the signal. Thus, in the case of a single detector setup, the resolution is determined by the extent of the optical or the acoustic focus, depending on which is smaller. Most high-resolution OA microscopes can be ascribed to the class of optical-resolution microscopes. They operate near the surface of the sample in a depth of a single mean free path, where optical lenses can create foci much smaller than any acoustic detectors. If, however, the region of interest is deeper within the sample, intense scattering renders optical-resolution devices useless. Acoustical-resolution setups are capable of measuring well beyond the optical diffusion limit; depending on the acoustic frequencies considered, they can reach several millimeters into the skin [Oma13],[Oma14]. Optoacoustic tomography can reach much deeper still. By using multiple detection points and modern image reconstruction algorithms, high resolution can be achieved with neither optical nor acoustical focusing. With that, OAs can cover multiple length scales from organelles to organs [Wan12], working in depths from 1 mm to 12 cm [Upp17].

Along with all the unique advantages of combining optical contrast with acoustical resolution, comes the challenge of incorporating both the detector and the illumination into the setup without one negatively affecting the other. In OA microscopy, this was achieved by guiding the light around the acoustic detector to create an optical focus underneath. However, this method fails if multiple detectors are used, or if a broader illumination area is desired. To circumvent the dilemma of shadows in the illumination altogether, transparent detectors were designed. With these, the optical and acoustical path can overlap without interference.

In [Zha08], a setup is presented which utilizes a Fabry-Perot interferometer to detect acoustic pressure transients directly at the surface of the sample. By positioning the illumination and detection on the same side of the specimen, backward-mode measurements are facilitated, as opposed to forward-mode, which works in transmission. This setup is especially useful for research on skin where the region of interest is accessible from one direction only. While the scanning of the Fabry-Perot interferometer is very fast, the optical detection method is surpassed by traditional piezoelectric transducers with respect to reliability and sensitivity. In 2005, Niederhauser et. al. used indium tin oxide (ITO) as electrode material to create a transparent piezoelectric transducer for OA depth profiling [Nie05]. Even though the technique showed promising results, it was not investigated further.

In this thesis, a transparent transducer with ITO electrodes on piezoelectric polyvinylidene fluoride (PVDF) was developed. The aim was to build a handheld OA setup capable of determining the thickness of melanoma, in-vivo and noninvasively. Except for the knowledge of the principle functionality of an ITO-PVDF detector, this work was done from the ground up. To be able to focus on the experimental aspects, a single detector was used, keeping the scope with respect to data acquisition and processing to a manageable amount. For that reason, no resolution values will be presented. Instead of a focus on imaging this work is concerned with establishing the bases of melanoma thickness determination using a handheld OA setup. We successfully validated the capability of the setup with measurements on phantoms which matched the simulated results. This setup was then used to conduct noninvasive in-vivo measurements in a brief pre-clinical trial. Although this first layout of the setup experienced some limitations, we are confident that, in the future, the technique can be further developed into a useful measurement system.

This thesis is structured as follows: Background knowledge is presented in Chapter 2, to illuminate the OA effect in the context of this work. Additionally, the relevant properties of human skin are explained, as is the MeDiOO project, in which this thesis is grounded. Subsequently, in Chapter 3, the theoretical basics of OAs are described, followed by exemplary curves resulting from simulations to visualize the fundamental signal properties. Chapter 4 contains the experimental facts, from the production of tissue phantoms to the design of the OA detector itself, and the different setups which it was used in. At the end of this chapter, the data postprocessing is described. In Chapter 5, the experimental results are presented and discussed, starting with measurements on tissue phantoms and other self-made phantoms representing the intermediate steps in the progress of the development. The validation process of the phantom measurements also includes the comparison to simulation. Finally, the results of the clinical measurement are presented and discussed.

Chapter 2

Background

In Section 2.1 optoacoustics (OAs) as relevant for this thesis and with respect to the broader meaning in framework of the research field will be elaborated. First the OA effect in general is explained with focus on the dominant processes relevant for the later discussion. Please note that the description here is from the phenomenological point of view. The theoretical description can be found in Chapter 3. At the end of this section the state-of-the-art is presented. In Section 2.2 the human skin is described in broad terms, including an explanation of how the values used for the optical absorption and the speed of sound were obtained. Subsequently, Section 2.3 will provide a few background details about melanoma occurrence and staging. The MeDiOO project in which this thesis was grounded is presented in Section 2.4. At the end of this chapter the way to calculate the maximum permissible exposure (MPE) is shown and compared to the irradiation intensities used in the preclinical trials.

2.1 Optoacoustics

In the modern use of the words, optoacoustics (OAs) and photoacoustics are absolutely interchangeable¹. They both describe the transformation of radiation energy into thermoelastic pressure waves. With the advent of modern lasers this technique experienced great progress over the last decades. Historically photoacoustic setups describe gas filled chambers in which a sample is irradiated by a chopped light beam. In those cases, the sample was either in the gas or solid state. The resulting acoustic waves are conveyed by gas to a microphone. For the measurements on gaseous samples, photoacoustic resonance was used, for which the gas is contained in a resonator and by tuning the chopper frequency, resonance could be observed [Kar84].

Another example for traditional photoacoustic spectroscopy can be found in [Gie86]. The setup consists of two interconnected gas chambers, one of which contains the microphone. The other chamber is cylindrical with an open and a closed side. Through the closed side the chopped light beam is coupled in while the open side is pressed on the sample, in this case a human forearm. Besides the sensitivity of the resonator the chopping frequency determines the probing depth of the measurement. However, photoacoustic spectroscopy only determines the amplitude of the integrated signal and thus only indirectly yields information about the depth profile of the absorber. Modern setups are different in that they do not depend on light choppers, which necessitate working with lock-in amplification, instead they utilize pulsed lasers. Powerful laser systems enable illumination with very short pulses producing stronger and sharper signals. Quickly progressing the method now extends into many fields of science.

We chose to use the word optoacoustics instead of photoacoustics because, historically it represents the generalized world of the optoacoustic effect independent of the setup or nature of the sample. Additionally, there are regional differences. Whereas photoacoustics is usually used in the US, European scientist often use optoacoustics.

¹A thorough history of the nomenclature, including several other names, can be found in [Man16]

2.1.1 The Optoacoustic Effect

The most basic description of the OA effect is the conversion of radiation energy into pressure. In principle any radiation, including particle radiation, can initiate the process. In practice however the vast majority of applications use electromagnetic radiation in the visible or infrared spectrum. A variety of mechanisms can transfer the radiation energy into local deformation of the sample (i.e. pressure). Some of these mechanisms ordered by increasing conversion efficiency are: Electrostriction, thermal expansion, photochemical changes, boiling or ablation, and breakdown or plasma formation [Tam86]. Although the conversion efficiency, that is from radiation energy into pressure, is higher in the latter three, they are impractical for most applications due to their invasiveness. This is especially relevant for measurements on living tissue. Electrostriction is not invasive and produces pressure even in transparent samples. However, the conversion efficiency is far too low to generate a detectable signal. Even in samples with very low absorption coefficients ($\mu_a = 10^{-5} \text{ cm}^{-1}$), absorption-based phenomena dominate [Gus93]. In general, and for this work in particular, the OA effect refers to the thermal expansion only, more specifically to the thermal deexcitation channel of optical absorption.

After light is absorbed the energy can be directly transformed to heat, which is called thermal deexcitation, or it can be deexcited through nonthermal channels such as: luminescence, photochemistry, photoelectricity, and energy transfer [Tam86]. All these phenomena are examples of the photothermal effect. After excitation all these channels subsequently transfer parts of the energy into heat. Depending on the channel this happens with a delay. While photoelectricity acts on time scales in the order of nanoseconds, photochemical chain reactions are capable of delays several magnitudes longer. This would produce spurious OA signals. Fortunately, these effects are negligible in comparison to thermal deexcitation.

If we imagine OAs as a two-step process, it can be divided into the optical irradiation and the subsequent propagation of the resulting pressure wave, in other words, we distinguish the optical and the acoustic domain. The optical irradiation introduces thermal energy, distributed according to the absorption profile. This heat distribution is then partly transferred into pressure by thermal expansion. The mathematical description can be found in Section 3.1. It is important to note, that only the energy converted to pressure is present in the OA signals discussed later. This conversion is more efficient when the

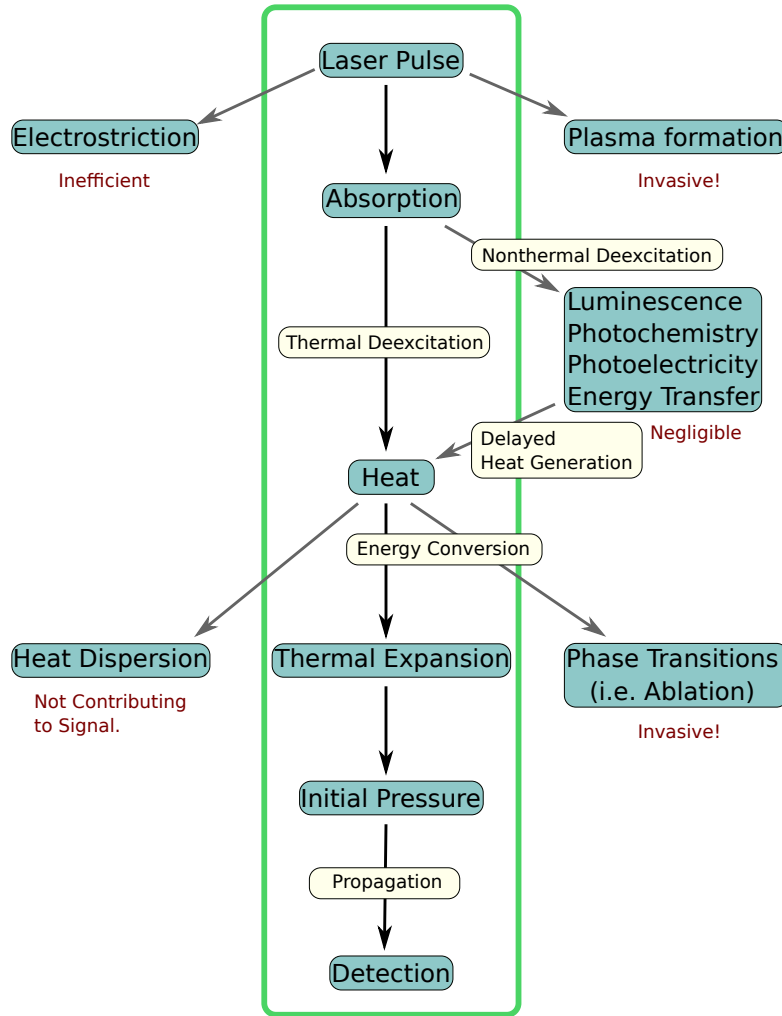


FIGURE 2.1: Diagram of OA pressure generation. In the center the process relevant to this work is framed in a green rectangle. The red descriptions underneath the blocks indicate the reasons why this aspect is not included. Inspired by [Tam86] and [Loh98]

irradiation time is short, which again is a reason for the fast developments in the field after introduction of commercial high-power lasers with pulse lengths in the nanosecond range. For a descriptive understanding we here assume instant irradiation, which as will be elaborated later is a valid approximation. Thus, after creating the initial OA pressure profile the optical irradiation has no further influence on the process and only the acoustic processes are considered. Most of this work focuses on the propagation of this transient pressure wave. From here on out, any description of waves, reflection or propagation is referring to purely acoustical effects if not denoted otherwise.

The initial pressure distribution resembles the optical absorption profile in the sample. With the speed of sound of the surrounding medium, the pressure transient propagates in all directions. Two modes of OA detection can be distinguished. The forward mode is

defined by the detector being on the opposing side of the illumination. From a practical point of view this has the advantage that the path of the illumination to the sample is separated from the path of the stress transient to the ultrasound detector. For the dermatological application desired in this work, however, the forward mode is impractical. The idea is to design a measurement setup that investigates a suspicious lesion without harming the patient. To realize the forward mode, either the ultrasound sensor or the illumination source would have to be implanted under the skin. Alternatively, the detector could be placed on the other side of the considered body part. Unfortunately, intermediate structures with vastly different acoustic properties than skin, such as bones, ligaments or air cavities (lungs) constitute impenetrable barriers for the signal. Thus, the only way to design a device that can be used noninvasively is for it to work in the backward mode. In the backward mode illumination and detection are placed on the same side of the sample. With regular ultrasound transducers², which are opaque, this poses another challenge. Any optical equipment in between ultrasound detector and sample would disturb the OA signal and vice versa, the detector would produce a shadow in the illumination. To solve this conundrum optically transparent detectors are used.

All measurements in this thesis are performed with a transparent piezoelectric transducer, the design of which is elaborated in Section 4.2. Using a transparent detector allows for the detector to be placed on axis with the illumination. Due to issues with the backing layer, that is the layer used to better match the acoustic impedance of the detector with its surrounding, not all measurements are on axis even though the transparent detector would allow it. When the illumination is not directed through the active area of the detector, it is necessary to position the detector far enough from the sample to allow the light beam to pass underneath. If the distance between detector and sample is large compared to the lateral extend of the acoustic source, it is called far field condition. When the detector is placed directly on the sample, it is called near field condition. The meaning of near and far field conditions will be explained in detail, with examples of simulated signals in backward mode, in Section 3.2. The approach to OAs presented in this section is reduced to the mode of operation used for the measurements presented in this thesis. However, the field of OAs is much broader, even if only transparent transducer setups are considered. To give an overview of different approaches and applications the state-of-the-art is presented in the subsequent section.

²The words transducer and detector are used interchangeably.

2.1.2 State-of-the-Art

As stated before, the OA effect was discovered by Alexander Graham Bell in 1880. However, progress was slow until the development of lasers which could produce high power pulses with durations in the nanosecond range. Only in the 1990s did the extraordinary evolution accelerate. Since then the topic expanded from a promising technique to a distinguished field, including its own scientific journal. While in the beginning the main idea was to use OA spectroscopy to determine the contents of gasses, nowadays biomedical imaging applications dominate the field. For the medical use, three categories for the modern OA setups can be designated: 1) Endoscopy 2) Microscopy 3) Tomography.

The main criterion an endoscope must satisfy is miniaturization. Especially in small animals, bodily orifices can be very narrow. Optical endoscopes are widely used in multiple medical fields to visualize the interior of the colon or esophagus. However, optical endoscopes only work very superficial. OA endoscopy on the other hand is capable of reaching depths of several millimeters [Upp17]. In [Li14] an endoscope with a diameter of 12.7mm is presented which can create images with an angular field of view of 100° , demonstrated on a rabbit colon. A major obstacle in establishing OA endoscopy in medicine is the fact that any gas volume in between the detector and the sample prohibits the OA transient to be measured.

The distinction between microscopy and tomography is hard to define. Roughly speaking, the capability of a microscope is defined by the focus it can achieve inside of the sample. Whereas the tomographic images are mostly produced by postprocessing of the data through elaborate algorithms and are not as defined by the hardware limitations. While most OA setups utilize some kind of focusing, it is the central feature of any microscopic setup.

OA microscopy produces high resolution images by creating a tight focus in the sample. In most cases both the optical illumination as well as the acoustic detector are focused. Depending on which focus is smaller we speak of optical-resolution or acoustical-resolution microscopy. There are two major techniques used to overlay the foci. One is to surround the detector with a ring-shaped mirror to guide the light around the OA detector and to ensure that the foci overlap [Zha06], [Wan09]. The other method is to use a prism which is optically transparent but has an acoustical border inside off which the pressure waves reflect [Yan14]. Both techniques are capable of producing images

with a resolution of a few micrometer [Wan12], however the penetration depth is limited, especially for the optical-resolution microscopy.

In any case, the OA microscopes are quite cumbersome and must scan mechanically over the sample to create a 3-dimensional image. Most high-resolution OA microscopes comprise a single detector which is fixed relative to the illumination. That way the whole detector head or the sample must be translated to scan the region of interest. While optical scanning can be implemented in a fast and elegant way using a galvanometric scanner, the acoustic scanning requires the focus area of the detector to be moved by mechanically translating the detector itself. In [Qi17] the scanning effort was reduced by somewhat separating the optical from the acoustical scanning. The galvanometric scanner guides the illumination pulses on straight lines over the sample, each line going through the center by a different angle. In the beam path an angled cover glass is placed not changing the optical but only the acoustical path. The pressure waves, diverted away from the optical beam path by the cover glass, are detected by a cylindrically focused transducer. The big advantage of the cylindrical focusing is that a whole line scan is in the field of view and can be recorded without moving the detector. After each line the acoustic transducer is rotated so the field of view matches the corresponding path of the optical scanning. Due to the elongated transducer focus this technique is determined by the optical-resolution, resulting in the limited penetration depth. Because of their rather superficial imaging capabilities of a few millimeter both OA microscopy and endoscopy are limited in their medical utility [Upp17].

By contrast, OA tomography is capable of imaging deep into scattering samples [Deá13]. In [Xia13] a system is presented able of 3D tomography of a human breast. With a field of view of $170 \times 170 \times 170 \text{ mm}^3$ the whole breast can be imaged in a single measurement. However, there are several issues that would have to be resolved for the 3D scanner to be applicable in medicine. The detector array, containing 8 transducers, is scanned in 2° steps over a total of 240° in circle around the sample. This means that in combination with the illumination, the whole space around the sample except for the side the breast would enter, is occupied by the setup. In addition, the space in between the sample and the detectors must be filled with water, further aggravating the execution of the measurements in-vivo. By contrast, measurements on small animals allow the experimentalist to sedate the specimen and to place it inside the setup. The animal is placed in a membrane

to shield it from the water but still allow the light to enter and the ultrasound waves to leave the sample.

In [Bue10] the perfusion of a mouse kidney is imaged with video rate. The mouse was injected with Indocyanine Green (ICG), a dye used in medical diagnostics, which is highly absorbing in the near infrared. Exogenous contrast agents are very useful to improve penetration depth and image contrast. The agent must be a strong optical absorber while being nontoxic and biodegradable [Upp17]. If a stable contrast agent fulfilling these requirements could be found, it might revolutionize the field of OAs. Already, concentrations in the order of μM can be detected [Tar15]. For research areas where contrast agents cannot be used due to lacking means of transporting them to the desired location or the applications are impeded by health concerns, the measurement setups must function with low contrast. This makes the transducer design especially important for OA tomography. Depending on the application it is used for, other requirements have to be met as well. In Figure 2.2 a table is depicted, comparing the three major types of ultrasound detectors. They are distinguished by the physical means with which the pressure is translated into a measurable signal.

	Piezoelectric	Optical	Capacitive		Good
Bandwidth	o	+	+		+
Sensitivity	+	o	-		Medium
Miniaturization	o	+	+		o
Cost efficiency	+	-	+		Poor
Parallelization	+	-	+		-

FIGURE 2.2: List for the comparison of different acoustic detection technologies used in optoacoustics. Based on [Lut13]

In the following the properties of the three categories are discussed, briefly. Because in this work a piezoelectric transducer is used, most comparisons are focused on that category.

Optical detectors, that is, those which use optical means such as interferometry, surpass piezoelectric detectors with respect to the bandwidth. The acoustic bandwidth is relevant for high resolution, because sharp changes correspond to high frequencies. Nonetheless, commercial piezoelectric transducers are available up to 100 MHz of center frequency, corresponding to a resolution of around $10\ \mu\text{m}$. As will be discussed later the bandwidth of the piezoelectric transducer itself is not the limiting factor in the context of this thesis. In terms of miniaturization, optical setups are far superior to piezoelectric

setups, particularly regarding endoscopic applications. Not included in the list above is reliability which is highly important for medical applications. Especially in combination with the accustomed use of regular ultrasound device in the clinics, the medical field might prefer piezoelectric transducers. In addition, the cost efficiency of the optical detection technique must be improved for it become viable in widespread use. Regarding mass production possibility, capacitive detectors are advantageous [Ome02]. Large arrays can be produced with micromachining, they are called capacitive micromachined ultrasonic transducers (cMUTs) [Cal05]. cMUTs have been proposed as an alternative to piezoelectric detectors in OA imaging almost a decade ago [Vai09]. However, the lack in sensitivity limits the utility, especially for biomedical applications where samples often provide low contrast.

Transparent Detectors and Melanoma Investigation

The central motivation for the setup developed in this thesis is its potential use in dermatological examinations. Therefore, backward-mode measurements are required³. As is often discussed in this thesis, OA setups working in the backward-mode can be improved by using transparent detectors. While the research of transparent piezoelectric transducers is far behind their optical counterpart, they might compliment them in the future. For now, the optical detectors are dominating the OA field regarding the capabilities of imaging human skin and cutaneous vascular networks. Subsequently, devices are described which are representative of the potential utility of transparent detectors. Afterward the current state of melanoma investigation using OAs is presented.

The most advanced technique is using a Fabry-Perot interferometer [Zha08],[Zha11]. It utilizes the interferometric effects caused by the OA pressure waves deforming a thin polymer layer. The local deformation of the Fabry-Perot interferometer is recorded by optically scanning over the whole surface. The combination of all those depth profiles results in a 3-dimensional image. In 2008 Zhang et al. presented their setup capable of 3D imaging soft tissue. Widened laser pulses from a tunable OPO illuminated the sample through the interferometric layer. A wavelength range of 600-1200 nm allows targeting of many contrast agents and a deep penetration into biological specimen. Due

³For a visualization of the forward and backward mode please refer to Figure 3.1.

to delays in the data acquisition each measurement step took 1s. In principle this technique of optically scanning an interferometric surface can be very quick, limited only by the runtime of the acoustic waves. An optical technique, which is very interesting but at an early stage of research, is using micro ring resonators as transparent OA detector [Li14]. In [Don14] this technique is used in an endoscopic device showcasing the utility of transparent detectors and the necessity of investigating different approaches for their design.

There are very few cases of transparent piezoelectric transducers described in literature. Even though, the poled PVDF foil often used as the piezoelectric layer in OA detectors is transparent, the electrodes are not. Only few materials are transparent as well as electrically conducting. In [Jae05] it was shown that even a sodium chloride solution is sufficiently electrically conducting to function as electrodes. Far superior with respect to conductivity is indium tin oxide ($In_2O_3 : Sn$, ITO). ITO is a wide-bandgap oxide semiconductor, which is both optically transparent in the visible and infrared wavelength range and electrically conducting [Gra02]. In contrast to water, ITO can be attached to the piezoelectric layer without the need of a waterproof tank to be built around it.

Preceding this work only a single publication used an ITO coated PVDF film as a transparent OA transducer. In a research paper from 2005 Niederhauser et. al. presented their setup capable of recording the depth profile of the optical absorption in a layered dye sample in backward-mode [Nie05]. While the main focus of the article lies on the measurement results and the principle advantages of the setup, instead of its specific design, some of the described features can be found in the setup developed here. Centerpiece was a 40 μm thick piezoelectric PVDF film upon which 200 nm ITO was vapor deposited on both sides. The active area was circular with a diameter of 3 mm. It was not specified how the active area was connected to the electrical amplifier. As backing layer, a 2 cm thick PMMA sheet was used. A clingfilm was placed on the ITO layer for mechanical protection. Glycerin was used as adhesive, to achieve an acoustical connection between the active area and the backing layer as well as the protection clingfilm. Even though the setup was described to appear quite rudimentary it could record the OA depth profile of the dye solution well enough that the absorption coefficient could be determined from the resulting curve. The principle functionality of the setup presented here is similar to the setup presented in [Nie05]. However, in contrast to our setup, it was neither handheld nor constructed sufficiently robust to be used in clinical measurements.

There are some experiences with the use of OAs for measurements on melanoma. In [Oh06] an OA microscope, utilizing a ring mirror to focus the illumination into the sample underneath the ultrasound transducer, was used to image a melanoma inoculated into a nude mouse. By working with both near infrared and visible wavelengths (764 nm and 584 nm) the tumor-feeding blood vessels as well as the tumor itself, up to 0.5 mm deep into the mouse, could be visualized. Also working with melanoma in nude mice, [Zho14] investigated the merits of illuminating through the skin next to the tumor instead of directly through the tumor itself. This approach has the advantage of the reduced absorption of regular skin in comparison to pigmented skin, allowing for deeper penetration. However, while it produced valid results in nude mice, it is questionable if it is applicable to humans. Melanoma are often wide spread, which reduces the light bypassing around the tumor to illuminate it from below.

Preceding this work only a single study could be found which tested the usefulness of OA measurements to determine the thickness of melanoma in-vivo. In total 15 lesions were examined, for 9 of those the histologically determined thickness was compared to the thickness measured by OA imaging [Cho15]. Even though the values agree well the results are not enough to establish the setup as precise enough for medical use. For the measurements a commercial device was used (Vevo Lazr 2100, Visualsonics Inc.). The setup is described in [Zho15] where a handheld OA probe was created to detect both melanoma depth and volume at high speed. The transducer array resembles the standard piezoelectric transducers used for medical ultrasound imaging. At the long side of the array illumination fibers are placed allowing to create a 2D image with each laser pulse. Unfortunately, the authors do not share the details about the image reconstruction they used. Thus, their results cannot be compared to ours. Even though they determined the thickness by analyzing the images which is not possible with the setup presented here, it shows that melanoma thickness determination using OA is feasible.

2.2 Skin

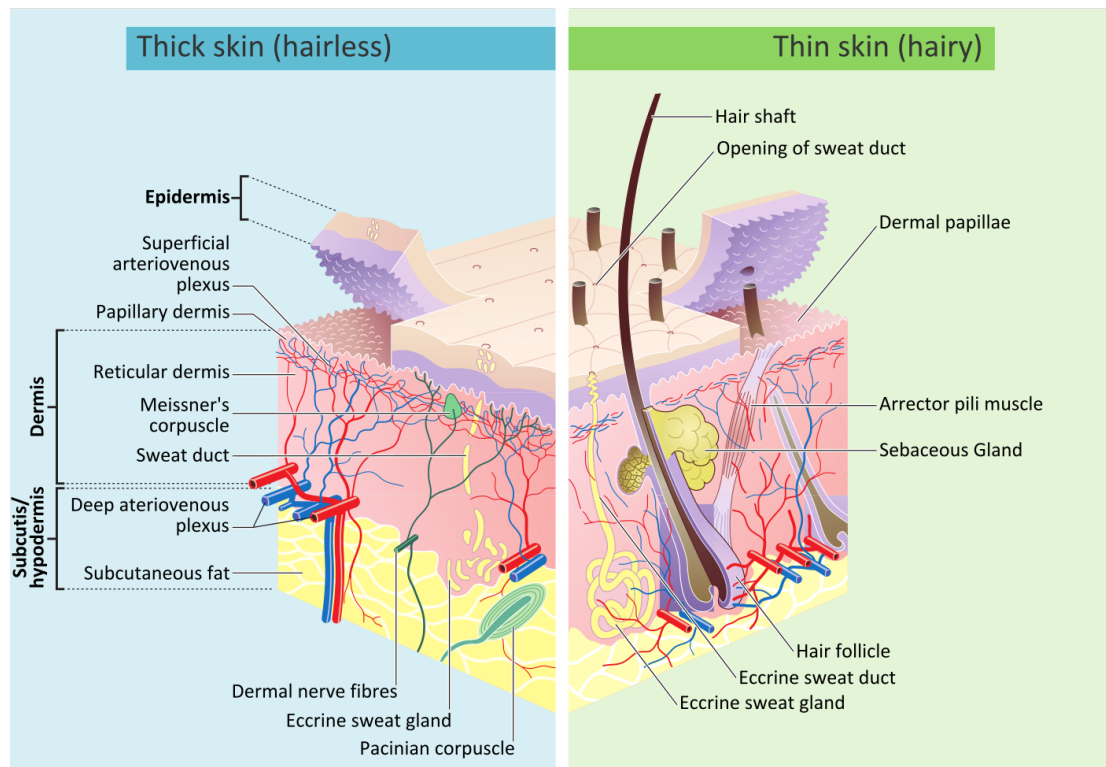


FIGURE 2.3: Schematic of the human skin. [WikiSkin]

Structure

Human skin can be divided into three layers namely the epidermis, the dermis and the subcutis. The deepest of those is called the subcutis or hypodermis and comprises the subcutaneous fat layer. On the abdomen this loose connective tissue can be several centimeters thick. Next in the direction of the surface is the dermis, a 2-4 mm thick layer mostly consisting of collagen fibers [Cos07]. The dermis is responsible for the structural integrity and flexibility of the skin. On top of the dermis lies the stratum basale or basal layer which is the deepest part of the epidermis. Depending on the thickness of the epidermis the basal layer is at depths ranging from 0.05 to 0.1 mm for hair skin (arms, chest, face...) and up to tenfold this depth for glabrous skin (palms and soles) [Dre04].

Melanoma emerge in the epidermis, for that reason we will focus manly on this layer of the skin. Even though keratinocytes constitute most cells in the epidermis they are of no relevance in the context of this thesis. At the basal layer the melanocytes reside which

produce the melanosomes containing the melanin mainly responsible for skin pigmentation. Together with the other cells produced in the basal layer the melanosomes rise to the skin surface. At the beginning of their life cycle, the melanosomes have a diameter of approximately 400 nm and the melanin grains contained in them have a diameter of about 159 nm [Bas00]. Because melanoma is the central motivation for this work, they are described separately in Section 2.3.

Absorption in Human Skin

While for the absorption in the dermis hemoglobin dominates, melanin is the main endogenous absorber in the epidermis [Smil1]. Two kinds of melanin are distinguished in mammals, eumelanin and pheomelanin [Mag77]. In human skin the volume ratio of eumelanin to pheomelanin is estimated to be 20:3, favoring the brown over the red appearing type [Kar12]. This ratio is different in red haired people, which is of no concern in this context because we are only interested in the contrast in absorption which correlates with melanin concentration indifferent of its type.

The melanin concentration in skin is difficult to determine and varies strongly, the weight percentage of melanin in human melanoma was found to range over more than an order of magnitude (from $< 0.0025\%$ to 0.84% by wt.) for dried ex-vitro samples [Wat81]. In 2012 a literature survey of the last decades by Lister et al. [Lis12] showed that in-vitro and in-vivo measurements of the absorption coefficient of the skin scattered significantly. Until today no explanation could be found for these irregularities. Theories about the influence of the skin thickness, for example, could not be verified. One source for an estimate of the absorption coefficient is a summary of optical skin properties by Steven L. Jacques [Jac91],[Jac98]. The calculations are based on the measurement of the absorption coefficient of a single melanosome (μ_a^{mels}), the skin baseline ($\mu_a^{baseline}$) and the concentration of melanosomes (C^{mels}) in the epidermis. The baseline was created from measurements on bloodless rat skin in an integrating sphere and the melanosome concentration was estimated from comparison of normal skin to melaninless vitiligo skin reflectance measurements.

$$\begin{aligned}\mu_a^{baseline} &= 0.244 + 85.3 \times \exp(-(\lambda - 154)/66.2) \\ \mu_a^{mels} &= 6.6 \times 10^{11} \times \lambda^{(-3.33)}\end{aligned}$$

$$\mu_a^{epi} = C^{mels} \times \mu_a^{mels} + (1 - C^{mels}) \times \mu_a^{baseline}$$

Where λ is the wavelength in nm and μ_a^{epi} the calculated absorption coefficient of the epidermis. These calculations are simplified which is obvious considering that they only include melanin as an absorber and do not allow for any differences in individual humans, such as age. Jacques himself declares them as a “starting point”, to get in the right region.

Using the melanosome concentrations from [Kar12] to calculate the absorption coefficient for the epidermis μ_a^{epi} of very fair ($C^{mels} = 0.0255$) and dark skin ($C^{mels} = 0.305$), we obtain for a wavelength of 532 nm, 1.46 1/mm and 16.9 1/mm, respectively. In the context of this work these values are important in two ways. First, they offer an estimate of the penetration depth and second, they give an approximation of the expected contrast in absorption between melanoma and regular skin. Black and Caucasian skin have the same density of melanocytes [Gor13]. The differences in pigmentation results from a varying production rate of melanosomes [Lin07]. Thus, it is reasonable to conclude that the melanin concentration and consequently the absorption properties of melanoma are comparable to black skin. As stated before, these are estimates which lack certain parameters such as hemoglobin and keratin concentration. Therefore, the equations given above yield an almost constant value for the contrast between melanoma and surrounding tissue over a broad range of wavelengths, not allowing for complex contrast changes. According to the literature the highest contrast yet achieved between a melanoma and its surrounding tissue is 68 at a wavelength of 764 nm [Wan08].

Speed of Sound

In OAs runtimes are measured which afterwards are converted to distances. To determine thicknesses using OAs the precise sound velocity of the investigated sample is essential. The length or depth of an object can only be determined as precise as the speed of sound is known. Unfortunately, biological tissue such as the human skin is prone to exhibit a large fluctuation in their properties. Besides OAs the speed of sound is essential for medical ultrasound imaging. Ultrasound imaging is a well-established method in multitude of medical fields, including the examination of fetuses in prenatal care or precisely guiding the needle to the correct nerves for anesthesia. For most purposes the pressure waves are used to penetrate several centimeters into the patient, thus, averaging local fluctuations

in the speed of sound. Dermatological exams on the other hand take place in the first millimeters of the skin rendering local changes in acoustic properties even more crucial. Furthermore, it is much more difficult to determine the precise sound speed of a thin layer as compared to big structures such as kidneys or muscles. In addition to these measurement challenges the speed of sound is influenced by changes in temperature or the ultrasound frequency used. Fortunately, it was found that the frequency plays a negligible role and may be omitted in these considerations [Mor95].

Many articles, especially those treating the fundamental theory of OAs, use a speed of sound of 1500 m/s regarding living tissue including human skin. Presumably this number is based on the sound velocity in water which is 1481 m/s. According to [Aga11], the sound velocity in human skin, not distinguishing between epidermis and dermis, ranges from 1498 m/s to 1710 m/s. Due to the large fluctuations we decided to utilize the mean value calculated from literature in [Mor95] which yields 1595 m s^{-1} for the dermis and 1645 m s^{-1} for the epidermis in human skin. Please note that the measurements in [Mor95] were performed on ex-vivo samples, which may have changed acoustic property compared to living tissue. However, the work presented here is mostly qualitative and does not depend on exact values. If the sound velocity is in the correct region relative to the other materials involved, the predictions are valid.

2.3 Melanoma

Commonly known as black skin cancer, malignant melanoma is a life-threatening disease afflicting the skin. Primary cause of melanoma is exposure to intense UV radiation, at a young age. Thereby, melanocytes which are located at the basal layer between the epidermis and the dermis are altered to produce a tumor. Due to the high risk of metastases it is the deadliest of all skin diseases.

In 2012, worldwide 55 thousand people died from melanoma [Int14]. In the same year 20,800 persons were newly afflicted with the disease in Germany alone, which represents 4% of all new cases of cancer [Rob15]. As can be seen in Figure 2.4 the diagnoses of melanoma rose significantly over the last decade. Reasons for this rise include higher life expectancies and a more comprehensive screening. However, life style changes such as

increasing sun-bathing during summer vacations and excessive use of tanning beds can be linked to the rise in new cases as well [Int14].

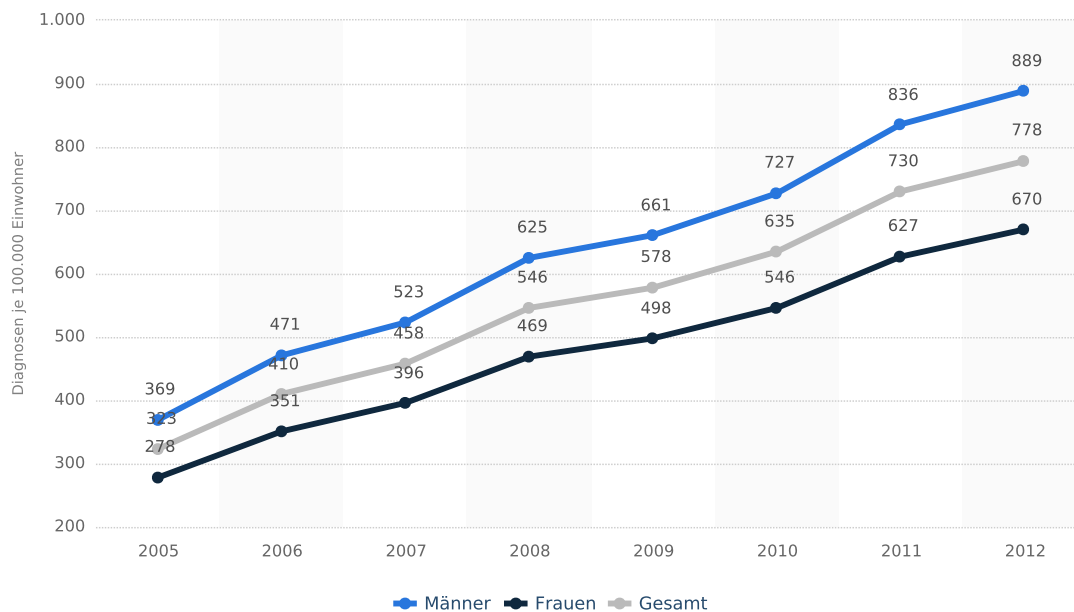


FIGURE 2.4: Number of diagnoses per 100.000 inhabitants of in-situ neof ormation of malignant melanoma in Germany of the years 2005-2012. Men in blue, women in black and the total in gray. [Bar14]

Since the 1980s the so called ABCD method has been applied, to distinguish a melanoma from a regular mole in a medical examination [Rig05]. Four features are investigated: **A**symmetry, **B**order irregularity, **C**olor variation, **D**iameter [San16]. In 1985 it was suggested that patients check themselves by the ABCD method [Fri85], however the criteria are still too complex for laypersons to judge the sincerity of a lesion. Later, an **E** was added, which stands for evolving or enlarging. However, this criterion is hard to screen, because the physician only obtains a snapshot of the lesion. When a lesion is determined to be suspicious the dermatologist either takes a biopsy which is common in the USA, or the lesion is excised which is the preferred method in Germany. After the excision the nevi can be staged. With increasing knowledge, the staging process of melanoma was revised over time from the Breslow thickness in the 70s [Bre70] to more complex staging since ([Bal01], [Rub10]). One constant over time was the relevance of the penetration depth or thickness of the tumor. While 5-year survival rates are around 99% for thin melanoma which have not penetrated the epidermis, the rate drops to 15% for later stages of the disease [Her12].

2.4 The MeDiOO Project

This work is almost entirely rooted and conducted inside the framework of the MeDiOO project. MeDiOO stands for *Melanomdickenbestimmung mittels Optoakustik und OCT* which translates to: "Melanoma thickness determination via optoacoustics and OCT". OCT is short for optical coherence tomography and is a purely optical method to obtain 1-3D images. In the project a commercial OCT (Telesto-II, 1300 nm central wavelength, Thorlabs GmbH, Germany) was used to obtain high resolution tomographies of melanocytic lesions [Var17]. In the same clinical studies the data for this thesis was taken.

Aim of the MeDiOO project was to create a device that combines the modalities of OCT and OA to measure simultaneously. In addition, a third modality was added, Raman spectroscopy, which instead of imaging enables us to obtain information about the chemical composition of a sample. Both Raman and OCT are purely optical methods which simplifies their combination and we decided to create a Raman-OCT and a separate OA device. However, as a proof of principle we show the possibility of performing an OCT through the OA detector film presented in this thesis. In Figure 2.5 the comparison of two OCTs is depicted. In Figure 2.5a) an OCT image of the measurement standard (APL-OP01, Arden Photonics Ltd) is visible. The pattern belongs to the part of the silica phantom used to investigate the lateral resolution of OCT. The phantom is traversed by lines with changing distances which appear as dots in the plain of view considered here.

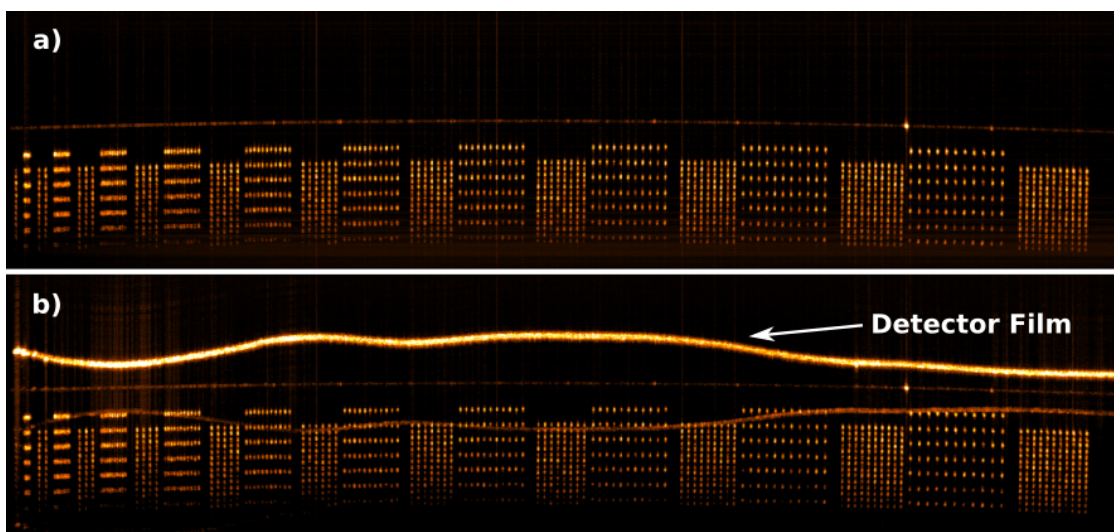


FIGURE 2.5: OCT image of a measurement standard with and without detector film.

In the OCT image of the phantom by itself several features can be distinguished. The horizontal line in the middle marks the surface of the phantom, its curvature results from focus effects. Underneath several arrays of dots are visible showing the cross section of the lines with the plane of observation. The individual points can be resolved for every but the two leftmost blocks. For Figure 2.5 b) depicting an OCT image of the same phantom, this time with the OA detector film on top, the resolution is comparable. In addition to the brightly visible detector film, its reflections off the sample surface overlay the phantom pattern. In both figures vertical lines appear which are produced by high intensity areas where sensor saturation yield image processing artifacts. Without the detector film only few of these artifacts are produced with the most prominent example being on the sample surface on the right-hand side. The same artifact is visible below the OA detector film in Figure 2.5b). However, the most artifacts of this kind are produced by the detector film, especially in regions where the film is orthogonal to the OCT beam. The reflections from the detector film reduce the signal strength of objects underneath. By comparison of the intensity values of the lateral resolution pattern with and without the detector film, we found a signal decrease of approximately 10%. Thus, it is possible to conduct high resolution OCT through an OA detector film. However, if the detector film would be employed by itself, internal acoustic reflections would distort the OA signal. To reduce these reflections a backing layer is needed.

For this work PVA-hydrogel and PMMA were used as backing layers, both created to much signal loss or distortion to create valuable OCT images. Nonetheless only the detector itself is essential for OA measurements while the backing layer could be adjusted or in principle even omitted. Consequently, it should be possible to create a backing layer that allows OCT to work unimpeded. However, the focus of this thesis is the creation of a functioning OA setup, therefore the OCT and OA setup were build up and tested separately. The clinical measurement procedure with the three modalities is presented in the subsequent section.

Clinical Procedure

For the MeDiOO project measurements in the clinic of dermatology in Rostock were carried out. As described earlier, OCT and Raman are purely optical, non-contact methods whereas OA necessitates skin contact for transmitting ultrasound. Following

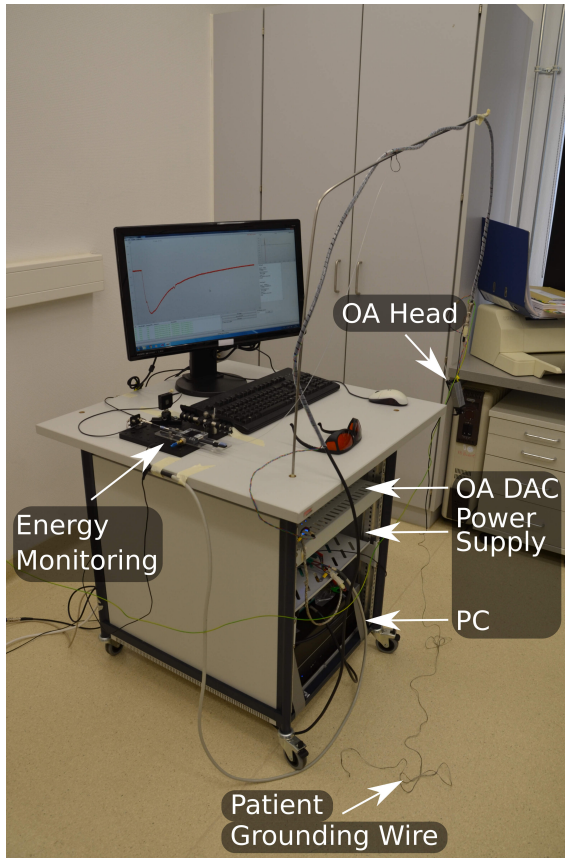


FIGURE 2.6: Photograph of the OA setup as used in the clinical study. The cart is mobile and can be wheeled. Except for the laser source, which was removed to reduce parasitic signal pickup, all equipment is included. The high-speed data acquisition card for the OA measurements as well as the power supply and the PC are located in the body of the rack. The energy monitoring setup is placed on top of the table to facilitate the needed energy calibration before the measurements. The loose-end wire on the floor is used for patient grounding. Hanging from a bend metal rod the OA measurement head can be swiveled to any position within the reach of the signal cable.

this distinction, the clinical measurements were performed by a combined OCT-Raman probe and a separate OA handheld setup.

For the combined measurements, first the patient was examined by the dermatologist to assess whether any suspicious lesions are present. In case of a positive result the patient signed an informed consent agreeing to take part in our study. Afterward the medical doctor drew a sign around the lesion marking where the incision would happen. The lesions were documented by regular photography and dermatoscopy, which is a specially designed closeup photo technique. First of the three modalities to be used on the lesion was OCT. After selecting the appropriate self-build spacer ring for the individual lesion, a fast OCT image was acquired to verify the correct positioning. This was followed by a high-resolution OCT for later evaluation. Subsequently, without moving the OCT-Raman probe a Raman spectrum was obtain of the lesion. For reference measurements the probe was then positioned approximately 2 cm next to the lesion on a spot of regular skin.

In preparation for the OA measurements the patient was then grounded. The grounding wire was placed as close to the lesion as possible. If the concerned body part allowed for it,

the wire was wrapped around several times. To maximize the area of contact aluminum foil was connected to the wire and used as grounding pads. For the OA measurement a drop of distilled water was poured on the lesion using a squeeze bottle. Only a small amount is needed to create an ultrasound conducting layer between the lesion and a circle of approximately 3 mm in diameter around the detector. By eye the OA detector was positioned above the middle of homogeneous or small (1-3 mm \varnothing) lesions. For bigger lesions or ones with irregular pigmentation multiple positions were chosen at distinct locations such as the darkest region.

Finally, a commercial ultrasound system was used for reference measurement which was compared to the OCTs. The ultrasound device DUB100-12 Bit from TPM is specially designed for dermatology. The most crucial difference to typical ultrasound devices is the very high central frequency of 100 MHz, resulting in a high resolution but shallow penetration depth. Exact positioning of the ultrasound head was complicated because it covered a skin area much larger than the lesion. To validate that the lesion was included in the scan, the ultrasound image was observed in real time. At the end of the measurements, the subtle imprint left by the ultrasound head was used make sure once more, that the position and orientation matched the presumed plane of the histological cut, indicated by the surgical drawing.

Immediately after the measurements the patient was brought to the operation room for the excision. The medical staff responsible for the analysis of the suspicious lesion proceeded in the regular way but made sure the orientations of the histological cuts were in accordance with our measurements. Especially for the OCTs it is prudent to know the orientations because unambiguous features are rare and if the orientation is unknown it is not possible to match the histology to the correct slice of the OCT. For a detailed description of the OCT-Raman probe, please refer to the dissertation of Arthur Varkentin.

2.5 Safety and Ethics

In this work in-vivo measurements on human skin were performed which necessitates certain ethic commitments. Most importantly, every person examined in the clinic signed an informed consent after being thoroughly informed by a medical doctor. At any time during the procedure, the patients were free to quit the study. To protect the eyes appropriate laser goggles were handed out to the patients before the measurements. For the measurements themselves, it is necessary to direct the laser directly at the skin, for which the maximum permissible exposure (MPE) needs to be considered. The MPE levels can be found in the BGI832 (Berufsgenossenschaftliche Informationen für Sicherheit und Gesundheit bei der Arbeit) or the ANSI Z136.1 (American National Standards Institute). For lasers with a pulse duration between 10^{-9} to 10^{-7} seconds and a wavelength 400-700 nm the MPE is as follows:

For a single pulse:

$$\text{MPE}_{\text{single}} = 200 \text{ J m}^{-2} = 0.2 \text{ mJ mm}^{-2}$$

For a single pulse in a train of pulses:

$$\text{MPE}_{\text{train}} = \text{MPE}_{\text{single}} \cdot N^{-0.25}$$

To make sure that the intensity is well below the MPE values, the pulse energy is carefully monitored, and the illumination area is chosen large enough. For simplification the area was determined by illuminating a sheet of plotting paper and observing the diameter by eye, through the safety goggles. By including only the part of the beam which is bright enough to be seen, it is ensured that the area is underestimated in the calculations. This procedure yielded an illumination area of at least 27 mm^2 (diameter of circular beam was about 6 mm) which means a maximum allowed pulse energy of at least 5 mJ. In principle, the pulses used in the experiments described here could be considered as single pulses because each measurement needs only a single pulse and the time in between measurement can be chosen freely. However, to save time and be on the safe side we consider the 10 measurements performed at each position as a train of pulses which gives us an explicitly underestimated MPE of 2.8 mJ per pulse. As can be seen later all energies used stayed well below the very restrictively calculated MPE values given here.

Chapter 3

Theory

3.1 Generation of OA Signals

In OAs two major regimes are discriminated: thermal confinement which considers illumination durations that are short compared to the thermal conduction and stress confinement which is the stronger condition that describes illumination times that are much shorter than the time scale of stress relaxation. Due to the availability of lasers with pulse durations < 10 ns, most current OA setups satisfy stress confinement as does the one considered in this work. Thus, in our case, the OA effect can be divided into the optical excitation and the subsequent propagation of the acoustic waves. By irradiating the sample with high intensity electromagnetic waves, heat is introduced to the system.

The heat equation describes the distribution of heat for a closed system, without energy loss through radiation or change in particle numbers.

$$\rho c_p \partial_t T(\vec{r}, t) - \alpha \nabla^2 T(\vec{r}, t) = H(\vec{r}, t) \quad (3.1)$$

Here, ρ represents the mass density, c_p is the specific heat at constant pressure, T the temperature, α the thermal conductivity, and H the heating function. As we consider a setup in stress confinement, thermal confinement is fulfilled by default. That means that the change in temperature caused by heat transfer is negligible on the time scale of the considered illumination.

Thus, equation 3.1 is reduced to:

$$\rho c_p \partial_t T(\vec{r}, t) = H(\vec{r}, t) \quad (3.2)$$

The introduced heat is partially converted into pressure, which is denoted as p_0 to represent the initial pressure profile of the OA transient [Gus93].

$$p_0(\vec{r}, t) = \Gamma H(\vec{r}, t) \quad \text{with} \quad \Gamma = c\beta^2/\rho c_p^2 \quad (3.3)$$

Γ , called the Grüneisen parameter, represents the efficiency with which thermal energy is converted into mechanical stress or pressure. c is the speed of sound, β is the thermal expansion coefficient. This rise in pressure is the source of the OA signal and solves the inhomogeneous wave equation, which describes the wave propagation with a non-zero source term. By assuming stress confinement, the source term for the inhomogeneous wave equation can be factorized into a purely temporal and a purely spatial factor. In the case of the nanosecond excitation pulse the temporal term can be expressed as a delta function and thus simplify the equation greatly [Bur07]:

$$[\partial_t^2 - c^2 \nabla^2] p(\vec{r}, t) = \partial_t p_0(\vec{r}) \delta(t) \quad (3.4)$$

Except for $t = 0$ the problem is reduced to a homogeneous wave equation with p_0 as starting value.

With help of the Green's function this partial differential equation can be solved to obtain:

$$p(\vec{r}, t) = \frac{1}{4\pi c} \partial_t \int_{S(\vec{r}, t)} \frac{p_0(\vec{r}')}{|\vec{r} - \vec{r}'|} dS'(\vec{r}, t). \quad (3.5)$$

S denotes the integration surface for which $|\vec{r} - \vec{r}'| = ct$ [Dea12]. This way the pressure at the detection point \vec{r} is related directly to the initial pressure $p_0(\vec{r}')$.

Initial Pressure Profile

In the preceding section the heating function $H(\vec{r}, t)$ is introduced to describe the energy distribution in the OA sample. Assuming stress confinement or at least thermal confinement the temporal evolution of the energy distribution can be neglected. Thus, the distribution is defined only by the absorption profile and light distribution. For simplicity we only consider the depth profile and assume a homogeneous absorption of $\mu_a(z) = \mu_a$, with μ_a as the absorption coefficient. To determine the light intensity I in the depth z the light attenuated in the layers above has to be taken into consideration. In general scattering contributes to the attenuation coefficient as well, yielding the attenuation coefficient $\mu_{att} = \mu_s + \mu_a$ with μ_s as the scattering coefficient. To determine the intensity distribution $I(z)$ when illuminated with I_0 , we start by dividing the sample into intervals with a thickness of Δz

$$I(z = 0) = I_0 \quad (3.6)$$

$$I(\Delta z) = I_0 - I_0(\mu_{att}\Delta z) \quad (3.7)$$

$$I(2\Delta z) = I_0 - I_0(\mu_{att}\Delta z) - (I_0 - I_0(\mu_{att}\Delta z))\mu_{att}\Delta z \quad (3.8)$$

$$= I_0(1 - \mu_{att}\Delta z)^2 \quad (3.9)$$

$$\vdots \quad (3.10)$$

$$\Rightarrow I(n\Delta z) = I_0(1 - \mu_{att}\Delta z)^n \quad (3.11)$$

$$\Rightarrow I(z + \Delta z) = I(z)(1 - \mu_{att}\Delta z) = I(z) - I(z)\Delta z\mu_{att} \quad (3.12)$$

$$\frac{I(z + \Delta z) - I(z)}{\Delta z} = -\mu_{att}I(z) \quad (3.13)$$

$$\Rightarrow I'(z) = I(z)(-\mu_{att}) \quad (3.14)$$

$$\Rightarrow I(z) = I_0e^{-\mu_{att}z} \quad (3.15)$$

This behavior is called Beer-Lambert law [Dem07]. Assuming non-uniform attenuation it can be expressed as follows.

$$I(z) = I_0e^{-\int_0^z \mu_{att}(\theta)d\theta} \quad (3.16)$$

Here, the included scattering coefficient is used to express the fraction of light which is redirected and thus not part of the beam anymore. Therefore light scattered back from deeper in the sample is not considered. In any case, this formula can only be used to approximate the light distribution in complex samples, such as biological tissue. If, however, scattering is very low in comparison to the absorption or mostly forward scattering occurs the absorption coefficient can be used instead of the attenuation coefficient. This way the energy distribution, and thus, the initial pressure depth profile can be determined through the absorption coefficient alone.

$$p_0(z) \propto \mu(z) e^{-\int_0^z \mu_a(\theta) d\theta} \quad (3.17)$$

3.2 Acoustic Near and Far Field

The terminology of the far field is often used in physics and is synonymous with having a viewpoint which is very far away from the object of interest so that the dimensions of the processes involved are negligible compared to the distance. One of the most popular examples is the dipole whose radiation patterns are regarded as spherical in the far field even though the dipole itself possesses a different symmetry. In OAs the term carries a slightly different meaning.

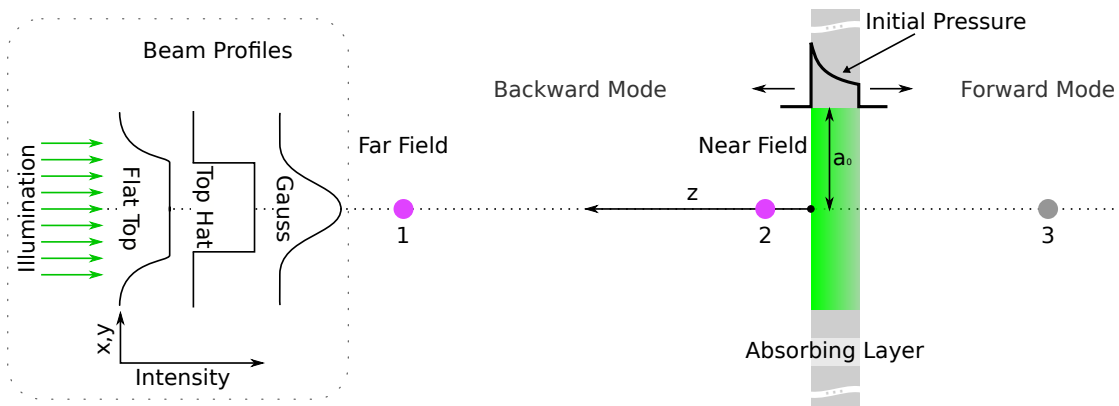


FIGURE 3.1: Sketch of simulation setup. On the left-hand side, the illumination is depicted including different beam profiles. On the right-hand side, the absorbing layer is presented where the illuminated part, with radius a_0 , is colored in green. At the top of the absorbing layer the initial pressure depth profile is indicated, horizontal arrows represent the relevant directions of propagation. Exemplary detector positions are denoted with 1, 2 and 3. Detector positions 1 and 2 are in the far- and near field, respectively, and in the backward mode regime, that is on the same side as the illumination. The forward mode regime is on the opposite side of the absorber where the third exemplary detector is located.

Regarding the propagation of ultrasound waves acoustic diffraction is essential for its understanding. First, we consider the near field condition in its simplest form. We assume an optically thin absorbing layer which extends infinitely in the xy plane and has a thickness of B in the z direction. The layer is illuminated homogeneously and instantly, thus the OA pressure can be represented by a box function. In this scenario, independent of the point of view, that is the position of the detector, all that can be detected is a plane wave. That way the detected pressure profile is always the box function of width B/c , c denoting the speed of sound, and is unchanged for any distance. This changes if the lateral dimensions of the OA source volume become finite and the plane wave symmetry is broken. From the borders of the source volume diffraction affects the profile. In the extreme case, where the distance between layer and detector is much larger than the lateral extent of the source volume, acoustic diffraction dominates the measured profile to resemble the derivative of the original pressure distribution.

In between these extremes the appearance of the resulting curve becomes quite unintuitive and needs to be simulated. The dimensionless diffraction parameter $D = \frac{2|z|}{\mu a_0^2}$, with z being the distance between detector and sample, μ the absorption coefficient and a_0 the beam radius, describes which regime is valid for a specific setup [Kar96],[Pal00]. In the case of an absorbing region (sample) which is smaller than the irradiation beam, a_0 becomes the radius of the absorbing material. If $D \ll 1$ near field conditions apply and diffraction is negligible, while $D \gg 1$ on the other hand describes far field conditions and diffraction dominates the wave form.

In Figure 3.2 various simulated examples for different values for D are presented. For the simulation, the source code developed by Oliver Melchert¹ was used, with minor modifications. In the simulation an absorbing layer was illuminated from the direction where the detector is located, i.e., in backward-mode. In this case the beam radius and absorption coefficient were kept the same, while the distance between detector and sample was changed. The beam profile in this case was chosen to be a flat top with steep slopes, making it quite similar to a top hat. Later in this section the effects of different beam profiles are discussed. With increasing distance, the pressure amplitude attenuates. To show the changes in the shape of the curves the simulations are normalized to their highest value. Also, to increase comparability, the run time delay resulting from different distances was removed, positioning all starting slopes to zero time.

¹<https://github.com/omelchert/SONOS/>

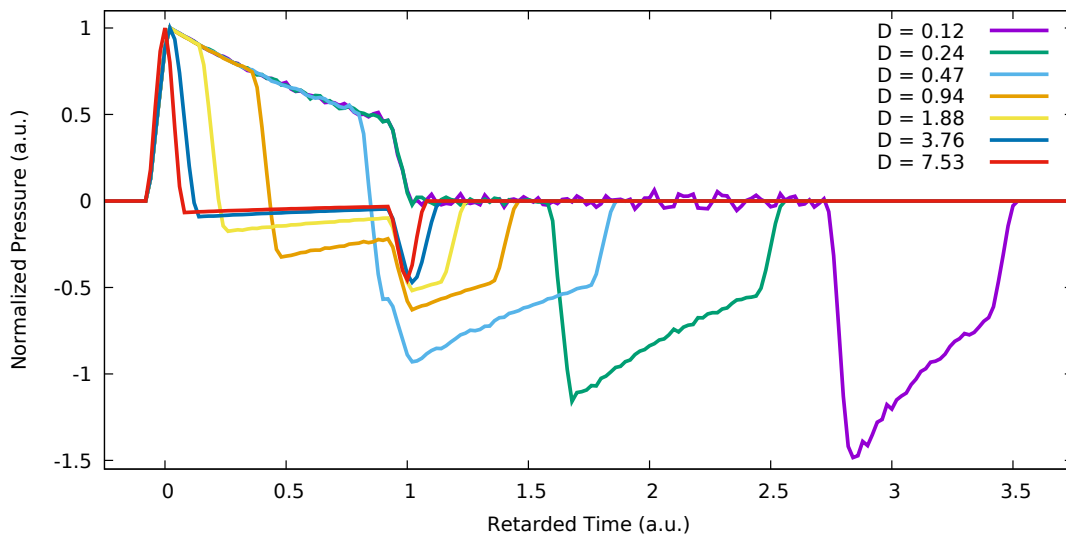


FIGURE 3.2: Simulated data to visualize the transition from near- to far field conditions in backward-mode. The diffraction parameter ranges from 0.12 in purple (near field) to 7.53 in red (far field) and is changed by increasing the distance between sample and detector. Further increase of the distance, and thus D , only slightly narrows the features and is omitted for clarity. Near field conditions recreate the original pressure profile (between 0 and 1 in retarded time) and the negative pressure feature of the acoustic diffraction follows with delay. In the far field the diffraction overlays with the absorption profile, finally yielding a curve resembling the first derivative of the initial pressure profile (red curve).

The purple curve ($D = 0.12$) represents the closest detector position which is well inside the near field regime. From retarded time 0 to 1 the curve matches the absorption profile, broadened by the assumed thickness of the detector. Following the first slope which represents the beginning of the absorbing layer the amplitude decays according to the Beer-Lambert law. The end of the layer is determined with the signal dropping to zero.

At approximately 2.7 retarded time the diffraction signal arrives. The form resembles the original absorption profile with inverted sign. For the detector position second closest to the OA source (green curve), the signal from 0 to 1 on the retarded time axis is unchanged. And after some delay the diffraction signal follows this time resembling the original profile even more. The further the detector is removed the closer the diffraction signal follows behind the initial pressure signal.

The light blue curve ($D = 0.47$) shows the beginning of the intermediate regime between the near and the far field. The diffraction signal reached the main signal and affects its form which now differs from the initial pressure profile. Note, even though the tail of the signal is altered the rear slope marking the end of the absorbing layer is still visible,

though hardly distinguishable. Further towards the far field ($D = 0.94$ to $D = 1.88$) the diffraction signal cuts further into the main signal until the rear end of the layer is marked by a dip and the curve drops into the negative values earlier each time. In this intermediate regime the form of the curve is unintuitive, even in this simple example.

When the real far field is reached the curve resembles the first derivative of the original pressure profile. Here $D = 7.53$ is the highest value presented. Higher values were omitted due to little additional changes, which can be inferred from the signals $D = 3.76$ to $D = 7.53$. At those values the diffraction has almost fully caught up with the signal leaving only a positive peak at the beginning of the layer and a negative dip at the end. In the far field the thickness of the layer can be determined easily by measuring the distance between these two features. Please note, that the width of the peaks would be infinitesimally small for an ideal point detector in the extreme far field.

3.3 Influence of the Beam Profile on the OA Signal

Besides the influence of the detector on the measurements, which in parts will be discussed in the subsequent section, the beam profile is essential for the form of the curve. As mentioned earlier, diffraction is an effect which is localized at the radial fringes of the irradiated sample. For that reason, there is no diffraction when an infinite plane is considered as source volume (extreme near field).

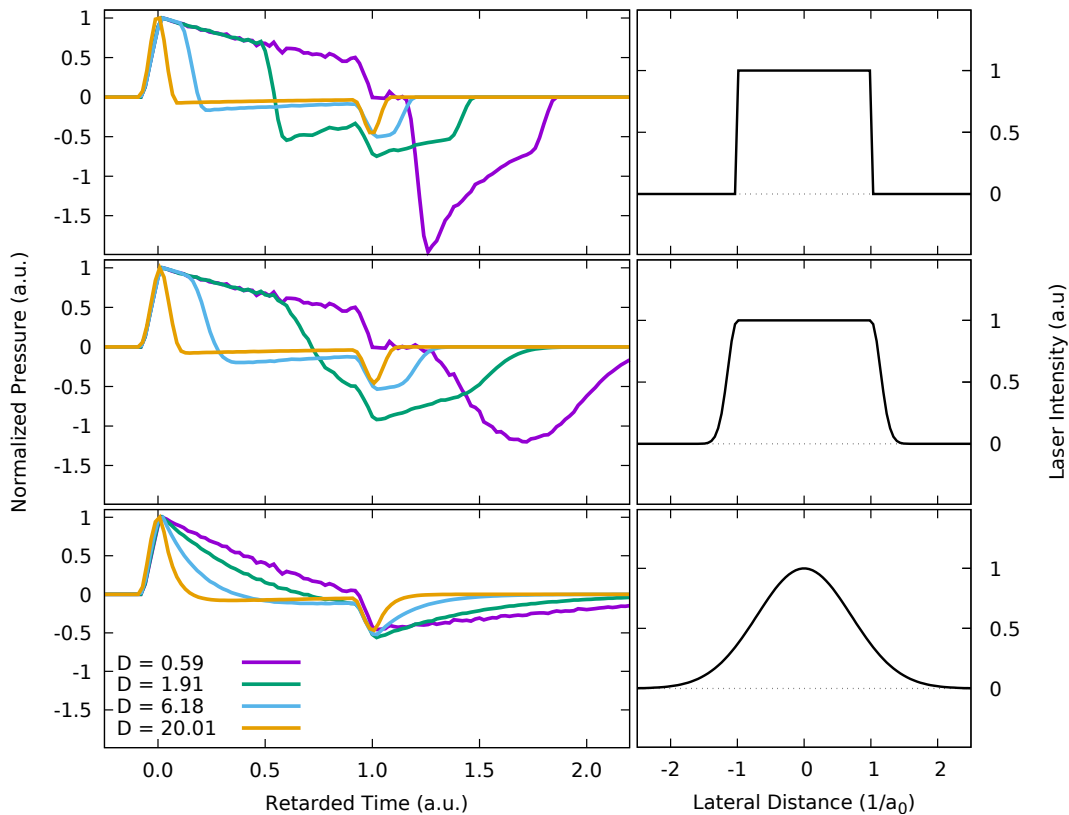


FIGURE 3.3: Visualization of the influence of the illumination beam profile on the OA signal. On the left side simulated OA measurements are presented. On the right side the related beam profile is shown. For comparability all measurement curves are normalized and shifted in time to begin at zero time. The same diffraction parameters used for all three beam profiles and the curves are colored accordingly.

In Figure 3.3 the OA signals for three different beam profiles and different values of D are presented. On the left the measurement curves are shown and, on the right, the respective beam profiles. As with the simulation for the far and near field discussion earlier, all curves are normalized and shifted in time for comparability. From top to bottom they are top hat, flat top and Gaussian. The top hat is the most intuitive with relatively sharp features. Because of the clear cut in the beam profile the onset of the diffraction is also very localized, see purple curve in top panel of Figure 3.3. The form of the diffraction

transient is similar to the original absorption profile. A very different appearance shows when the illumination occurs with a flat top profile. Here, the diffraction signal, visible with delay after the main signal (see purple curve in middle panel), differs strongly from the initial pressure distribution. Instead of the Beer-Lambert behavior the diffraction signal rather resembles a bell curve.

The far field measurements on the other hand are very similar which can be explained by the nature of the far field conditions. The central assumption for the far field is that the distance of the observer is large compared to the intrinsic length scales of the process. In that case the signal is reduced to its main features which for the flat top is the constant part of its profile. The Gaussian beam profile produces a different signal even in the far field (yellow curve in bottom panel). Instead of a symmetrical initial peak where both flanks resemble each other, the falling edge appears with a smoother exponential decay. The same holds true for the dip. In the near field the difference becomes more prominent. Except for the rising flank of the initial peak and the beginning falling flank of the dip all other parts of the curve are obviously different to the other beam profiles. Also, one must be careful when discussing near field conditions regarding Gaussian profile, because its curved shape is changing on any scale. Which is why, in contrast to the top hat, the parameter for the beam radius relevant for the diffraction is more complex. Here a_0 for the Gaussian beam profile is defined by the lateral distance where the function is reduced to $1/e$ of its maximal value. The lateral distance of half the maximal value could be used as well. However, in the context of this thesis the Gaussian beam profile is of limited interest, because all experiments are performed with a beam profile close to flat top.

To be more realistic, the simulations discussed here assume a detector of finite thickness which leads to an averaging over time. However, the detector is still idealized in terms of its directivity, that is the dependence of the sensitivity on the detection angle. Real detectors are more sensitive to normal incident waves, which will be elaborated in the subsequent section. Because diffraction is an off-axis signal by definition, the directional response of a detector limits the influence of diffraction.

Directivity or Directional Response

For an ideal isotropic detector, only the ratio of the distance between source and detector to the lateral extent of the source volume is of interest to distinguish between near field and far field conditions. However, the directional response of physical detectors is always anisotropic [Smi79]. There are two main reasons for this, the finite size of the detector and the intrinsic directivity given by the detector material [Pal09]. Often in simulations a point detector is used which is measuring the pressure exactly at one position. If the point is expanded to a disk of finite size, the detector can be simulated by integrating over an array of point detectors arranged in the form of the disk. Even though each single point detector is isotropic, the resulting disk-shaped detector possesses directivity, that is comparable to the optical diffraction at a single slit. For an infinitely extended detector plane, only waves incident in the direction normal to the detector surface would be detected. Real detectors usually extend a few millimeters or less in lateral dimensions which, on its own, is not enough to explain the directivity found [Xia13c].

In addition to the integrating effects the material properties have to be considered. Although material related directivity is present in any piezoelectric material, we will focus on PVDF here (see Section 4.2.1). In the case of PVDF, the polymer is poled to exhibit the required piezoelectricity, which is an anisotropic process that contributes to the detector directivity. For the detectors presented in this work, the PVDF film was biaxially poled. Poling is the process of stretching a polymer while applying a strong electromagnetic field. This leads to an alignment of the dipoles and thus creates piezoelectric properties in suitable materials, such as PVDF. Through stretching biaxially, the piezo strain constants along the plane of the film are similar. However, the piezoelectric response along the direction normal to the surface of the film is much stronger, which is called thickness mode. Thus, even assuming a point detector, made of PVDF, the normal component would be dominant.

Finally, another factor affecting the directional response of the detector is the dependence of the reflection coefficient of the acoustic waves on the angle of incidence. It is rarely possible to match the acoustic properties so that the pressure waves can enter the detector film without any loss due to reflection. With increasing angle, the reflection coefficient increases as well which in turn leads to further directivity.

3.3.1 Acoustic Reflection

Like any propagating wave, acoustic waves are affected at boundaries at which the properties of the medium change. At the boundaries the solution to the wave equation must satisfy continuity conditions, i.e. conservation of energy and momentum. If only plane boundaries are regarded the reflection conditions are simplified by the translational invariance which constitutes an unchanged component of the wave in the direction parallel to the plane. Comparable to the propagation of light this condition leads to Snell's refraction law. The continuity condition at the boundary require that the sum of the reflected and the incident wave equals the refracted wave in pressure. Expressed in terms of the reflection and transmission coefficients R, T we obtain:

$$1 + R = T \quad (3.18)$$

For simplicity we will consider the special case of a wave with normal incidence passing through a plane boundary from medium 1 into medium 2, for a detailed description please see [Bre90]. After solving the wave equation in accordance with the above-mentioned boundary conditions the reflection coefficient takes its most intuitive form:

$$R = \frac{\rho_2 * c_2 - \rho_1 * c_1}{\rho_1 * c_1 + \rho_2 * c_2} = \frac{Z_2 - Z_1}{Z_2 + Z_1} \quad (3.19)$$

with ρ and c being the mass density and the sound velocity, respectively. The indices denote the respective medium to which the parameter belongs. Z describes the resistance of a medium against pressure waves, comparable to the electrical impedance which is a measure of the dynamic resistance to applied electrical fields. Most importantly for later discussions are the different signs carried by the reflection coefficient depending on which medium has the greater acoustic impedance. Two cases are to be distinguished. First, if the wave travels from the high impedance layer into the low impedance layer ($Z_1 > Z_2$) we speak of a soft boundary and the sign changes. Secondly, assuming the wave travels from the low impedance layer into the high impedance layer ($Z_1 < Z_2$) and the reflection coefficient is positive, we speak of a hard boundary. Reflections on a hard boundary preserve the sign which in the extreme case of $Z_1 \ll Z_2$ ($R = 1$) entails that incident and reflected waves are identical except for the direction of propagation. Reflections on a soft boundary, $Z_1 \gg Z_2$ ($R = -1$), switch the sign of the pressure.

3.4 Signal Deconvolution

The convolution of two functions (f_1, f_2) is defined as follows [Baer09].

$$(f_1 * f_2)(t) := \frac{1}{2\pi} \int_{-\infty}^{\infty} f_1(t-u)f_2(u)du \quad (3.20)$$

According to the convolution theorem, the product of the Fourier transformed functions equals the Fourier transformation of the convolution of the functions [Baer09].

$$\mathcal{F}[f_1 * f_2] = \mathcal{F}[f_1] \cdot \mathcal{F}[f_2] \quad (3.21)$$

In practice it is rarely possible to measure only the physical phenomenon of interest. Besides noise and signal pickups from the experimental environment, the measurement setup itself alters the output signal. This becomes obvious when an infinitesimally short pulse is detected, i.e., the input signal is the Dirac delta function $\delta(t)$. The delta function contains all frequencies in equal amplitude. However, the output signal will convey some frequencies stronger than others. Thus, in response to the delta function any real system will produce an output signal specific to its setup, called the impulse response function (IRF). Mathematically speaking, any output signal is the convolution of the input signal with the IRF.

$$f_{out} = (f_{in} * f_{IRF})(t) = \frac{1}{2\pi} \int_{-\infty}^{\infty} f_{in}(t-u)f_{IRF}(u)du \quad (3.22)$$

For the present work, the output signal is given and the IRF can be obtained, or at least approximated, through measurement. To determine the input signal the convolution theorem is used.

$$\mathcal{F}[f_{out}] = \mathcal{F}[f_{in}] \cdot \mathcal{F}[f_{IRF}] \quad (3.23)$$

To determine the unknown f_{in} we deconvolve f_{IRF} from f_{out} which in the Fourier space is efficiently done by division.

$$\mathcal{F}[f_{in}] = \frac{\mathcal{F}[f_{out}]}{\mathcal{F}[f_{IRF}]} \quad (3.24)$$

By inverse Fourier transformation we obtain f_{in} .

The Gibbs Phenomenon

In order to reduce noise or unwanted transformation artifacts it is sometimes necessary to remove high frequencies during the deconvolution process. However, without these frequencies fast changes in the signal cannot be reproduced. This effect is described by the Gibbs phenomenon.

If a function with a jump discontinuity is approximated by the partial sum of the Fourier series, overshoots occur at the position of the discontinuity [Baer09]. To recreate this infinitely sharp feature an infinite series is needed. By cutting of higher frequencies, fast changing features yield so called “ringing artifacts“. Interestingly, the size of the overshoot is not depending on the frequency cutoff but only on the height of the jump. The oscillation of the ringing depends on the cutoff frequency. For visualization of the artifact, three different frequency cutoffs are presented in Figure 3.4.

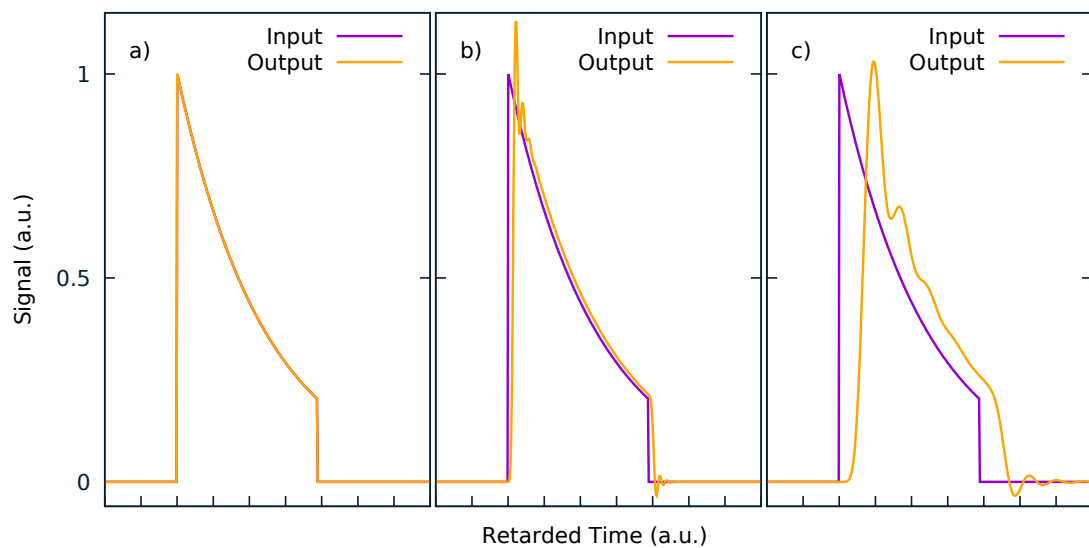


FIGURE 3.4: Beer-Lambert input signal (purple) compared with different output signals. The data was Fourier transformed, parts of the frequencies removed, and transformed back. a) All frequencies are preserved (curves overlap). b) Highest 60% are suppressed. c) Highest 90% are suppressed.

To facilitate the comparison to the OA signals presented later, the signal shape follows the Beer-Lambert law as described earlier. This signal is Fourier transformed, then frequencies above the cutoff are filtered out and finally the signal inverse transformed. In Subfigure a) all frequencies are retained during the transformation, yielding an output signal which is identical to the input sample. If, however, any frequencies are suppressed the ringing artifacts appear. In Subfigure b) 60% of the frequencies are suppressed

yielding distinct artifacts at the discontinuities. Because these filters are representing the effect of a real-life setup they must confirm to causality, which is why they do not affect the signal before the discontinuity. In Figure 3.4c) even more frequencies are removed, thus, differences between input and output signal increase. Note that, the oscillation into the negative after the second discontinuity is equal in amplitude in Subfigures b) and c).

In Section 5.4.2 the clinical measurements are presented. During the data processing a frequency cutoff at 20 MHz was necessary. Taking the Gibbs phenomenon into account, the signal shape can be explained quite well, which helps to relate the unintuitive signal shapes to possible absorption profiles.

Chapter 4

Material and Methods

In this chapter the experimental part of this thesis is presented. It begins with the description of the hydrogel phantoms and the method with which they were created. Subsequently, in Section 4.2 the design, fabrication and properties of the transparent transducer film are explained. This detector film is the centerpiece of all OA setups presented in this work. Section 4.3 contains the details about the general setup used for all measurements, including the energy monitoring, as well as the individual detector setups used. Concluding, in Section 4.4 the signal processing is elaborated.

4.1 Polyvinyl alcohol Hydrogel Phantoms

Phantoms for OA measurements are special in that they are required to have the correct acoustic as well as optical properties. The aim of this work is to investigate melanomas, for which phantoms are needed that mimic human skin. Polyvinyl alcohol hydrogels (PVA-Hs) are suitable tissue phantoms, for their acoustical similarity to soft tissue [Kha03],[Maz10]. As the name suggests, hydrogels consist mostly of water which determines their acoustic properties to a high degree. Thus, both the speed of sound as well as the density are comparable to water. Although, the water concentration in human skin varies greatly ($\sim 20\text{-}70\%$), depending on the regarded skin area, hydration and depth [Suh05],[War88], the acoustical properties are comparable to water and hence hydrogels.

In contrast to water, both hydrogel and soft tissue possess a flexible structure of intertwining fibers made of polymer or collagen, respectively. For the hydrogels this inner structure is created by the polymerization. To bring about polymerization in hydrogels, chemicals can be added, or they could be irradiated with γ -rays or electron beams [Has00]. However, chemicals leave behind toxic residue and irradiating the sample is inconvenient. On the other hand, the *freezing and thawing* method [Has00] provides a convenient way for intrinsic polymerization. PVA consist of polymer chains and when solved in water the chains can move freely, without bonds between the chains. However, when the gel is cooled the chains cross-link, that is, connections between polymer chains are formed, giving the hydrogel a flexible structure. Unfortunately for our purposes, the freezing of the water would cause micro pores in the hydrogel yielding turbidity. As a countermeasure anti freezing agents have to be added. Dimethyl sulfoxide (DMSO) is often used because of its high solubility [Hou15], however, it is hazardous for humans and needs to be removed after the fabrication which is inconvenient. Ethanol on the other hand is fairly harmless and can be left in the phantom even when put in direct contact with skin. The original production recipe was created by Christian Suhr and Merve Wollweber [Wol14]. In this thesis, the phantom preparation was improved regarding the optical clarity and general reproducibility.

4.1.1 PVA Hydrogel Preparation

The basic ingredients for the PVA-H preparation are listed in Table 4.1.

Ingredient	Supplier and product name	Amount
Polyvinyl alcohol	Sigma-Aldrich 363146, Mw 85-124 99+% hydrolyzed	7.2 g
Pure ethanol	Carl Roth, ROTIPURAN $\text{\textcircled{R}} \geq 99,8 \%$, p.a.	20 ml
Distilled water	Inhouse filter system	36 g
Melanin (synthetic)	Sigma-Aldrich, M0418-100MG	0 mg, 4.5 mg, 45 mg, or 90 mg

TABLE 4.1: List of ingredients for the hydrogel preparation.

Clear Hydrogel Layers

In a closed 100 ml screw neck bottle (Carl Roth, X712.1 Rotilabo) PVA granule and distilled water in a weight mixing ratio of 1:5, is placed in a water bath on top of a magnetic stir heater (IKA, RET control-visc). Using the temperature probe the water bath is kept constant at 94°C while the 4 cm stirring bar rotates at 350 RPM. Due to the high viscosity it is important to use a stir heater with a strong magnetic hold on the stirring bar, otherwise constant vigilance and adjusting of the rotation frequency is needed.

After 40 min of stirring the aqueous solution should be homogeneous and completely clear. If visual examination reveals undissolved PVA, the process is to be continued as long as necessary. To prevent the hydrogel from freezing a total of 20 ml of ethanol is added in steps of 5 ml, 5 ml and 10 ml. Using a pipette, the ethanol is trickled on the inside of the bottle to warm it up before it comes into contact with the PVA-water mixture. Nevertheless, white schlieren form at the phase boundary and need to be dissolved. Therefore, after every step the bottle is closed and placed back in the water bath and stirred until the solution is clear again.

The progress can be improved by increasing the rotation speed, so the stirring bar flips over and that way the higher regions of the gel are reached. Before carefully opening the bottle, especially after the ethanol is added, it is important to let it first cool for

a minute to prevent boiling and excessive evaporation. Sometimes schlieren are formed above the mixture and have to be removed by tilting the bottle to rinse the inner walls. When the last 10 ml of ethanol are added and all schlieren are dissolved the bottle is again taken out of the water bath and allowed to cool down. After approximately 3-4 min it has cooled enough so that it can be touched but must be opened carefully because overboiling is still possible.

At approximately 60 °C the hydrogel shows a viscosity comparable to honey and can be

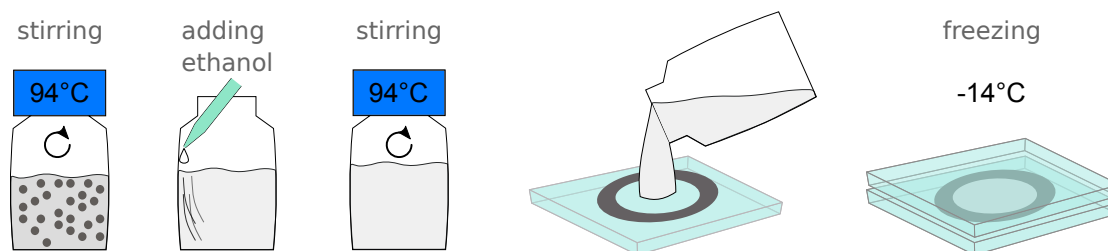


FIGURE 4.1: Process of PVA hydrogel preparation.

poured into the mold. For the layered structures utilized for the experiments presented in this thesis the molds were composed of two window glass plates encompassing a single ring determining the thickness of the phantom. Depending on the desired thickness either a 1 mm thick commercial spacer ring made of steel or a 3D printed acrylonitrile butadiene styrene (ABS) ring with optional thickness is chosen. The ring is placed on one of the glass plates and subsequently filled with hydrogel. To remove air entrapments the ring is overfilled and left to settle until every part up to the edge is filled with hydrogel. Due to the overfilling of the gel over the ring edge the second glass plate first makes contact with the viscous solution, squeezing it into every niche, thus removing any air bubbles left. The material flowing over the ring can be removed easily when the polymerization is finalized. To perform a single *freezing and thawing* cycle the phantom is placed in a freezer at -14 °C for 2 days. After the sample is taken out of the freezer it is kept at room temperature to thaw.

The rest of the unpolimerized gel can be stored in the closed screw neck bottle at room temperature for weeks without notable changes. Only the loss of ethanol through the repeated heating and opening of the bottle might be problematic because it raises the freezing temperature, which in term increases the risk of obtaining turbid hydrogel.

Absorbing Layers

The main aim of this work is to analyze the OA properties of human skin. As mentioned earlier, melanin is the main absorber in the epidermis and is presumably the only relevant contributor to the OA signal. We compared natural melanin from *sepia officinalis* with synthetic melanin and due to the close resemblance of the two and the higher cost efficiency the synthetic melanin was chosen for the experiments (see Table 4.1). The mentioned resemblance concerns the phantom preparation in terms of clustering and distribution in the phantoms. Regarding the absorption, [Bas00] found the absorption coefficient of synthetic melanin to be significantly higher compared to the natural chemical. Owing to the stronger absorption less melanin is needed, which prevents the clustering that occurs with high concentrations. Melanin is an aggregate of molecules robust enough to withstands both the heating and the freezing of our production process.

To ensure a homogeneous distribution of the absorbers without clusters it is added early, together with the PVA. Before weighing, the synthetic pigment is ground thoroughly for several minutes until no grain can be found anymore. The stirring process may be prolonged when melanin clusters are visible. However, some of these clusters are very robust so that even hours of stirring at 94 °C is not enough to break them apart. Thus, if clumps of melanin outlasted the grinding, they were present in the final phantom. The hydrogel layers endured only for a few days after preparation, because of that, individual specimen were not named. Instead they are categorized after the amount of melanin used (see Table 4.1).



FIGURE 4.2: Photographs of PVAH layers after freezing. Left: Clear PVAH with 3 mm thick 3D printed ring. Middle: 45 mg recipe of melanin in 1 mm thick spacer ring. Right: 1 mm thick layer, prepared after 90 mg melanin recipe, held in front of ceiling lamp.

In Figure 4.2 different layers of PVAH are presented, after they have been taken from the freezer. In the left photograph a 3 mm thick layer of clear hydrogel is depicted. The ring for this sample was printed using a 3D printer to enable us to flexibly choose the thickness. To remove slight irregularities and make sure the thickness is precise, the ring was filed down by hand. The thickness was verified by caliper measurements. The photograph in the middle shows a 1 mm thick cylinder of PVAH produced after the 45 mg melanin recipe, producing a deep brown color. The 1 mm metal spacer rings are commercially available; their thickness was verified using a caliper. At the outside rim of the spacer ring excess material is visible, which is pressed out of the ring when the upper glass plate is applied. An excess is necessary to ensure that no gas bubbles are left behind. On the right-hand side, a photograph of a 1 mm thick sample created after the 90 mg recipe shows such a gas bubble. In this picture the layer is held in front of the ceiling light. Here no excess material was poured into the ring. Fortunately, the measurements presented in this work needed only an area of a few square centimeters, thus gas bubbles or irregularities at the edges could be ignored.

4.1.2 Phantom Preparation

Once the samples are thawed, which takes a few minutes at room temperature, they can be combined to create the phantom. The glass plates are removed by hand or in more difficult cases leveraged apart by using a screwdriver or a metal spatula. Depending on the temperature reached at that point, the material has become very flexible and caution has to be applied not to create fissures in the sagging layer. Thicker layers can be loosened from the ring by pressing with the fingers. Especially with the 1 mm samples this would damage the hydrogel layer. In those cases, a scalpel is used to cut the layer off as close to the ring as possible. The detached PVAH samples are temporarily put into petri dishes filled with distilled water. Now the layers are ready to be stacked in the desired order. Throughout the whole process it is important to retain a film of water on the hydrogel to prevent desiccation on the one hand and sticking together of the layers on the other hand. After the OA measurements are performed the layers can be separated and stored again. They can be kept for days in a bath of distilled water, however, after only a few hours the properties begin to continuously change (speed of sound and consistency). Clear layers should be stored separately to prevent them from being stained by the melanin which is washed out of the absorbing layers.

4.2 Transparent Ultrasound Transducer

In this section the transparent detector used for the OA measurements is presented. The centerpiece of the detector is a 9 μm thick polyvinylidene fluoride (PVDF) film (Precision Acoustics, Dorchester, UK), which is biaxially stretched and poled to achieve piezoelectricity (Properties listed in Table 4.2). Upon the PVDF film 50 nm indium tin oxide (ITO) is sputtered as electrodes. The general idea of the detector was developed by Merve Wollweber [Wol06] and Ronald Krebs [Kre10]. In their works metal electrodes are used which are not transparent, but it functioned as a proof of principle for the self-made transducer.

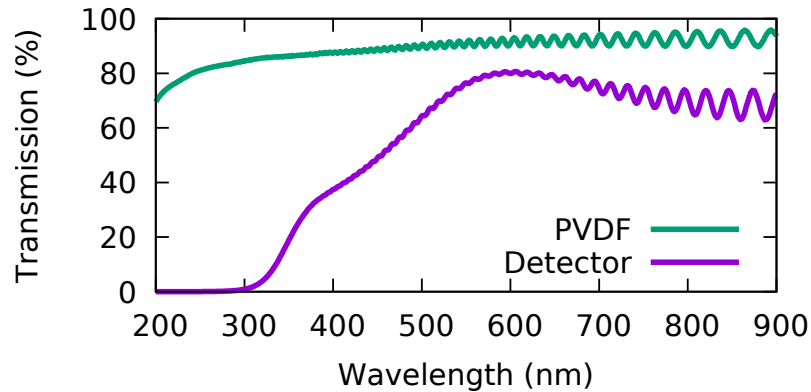


FIGURE 4.3: Transmission spectra of PVDF film with (purple) and without (green) ITO electrodes. ITO reduces transparency drastically below 400 nm, at 600 nm transmission is maximal (80 %) and decreases slowly towards higher wavelengths. At 532 nm transmission is still above 70 %. Oscillations are due to interferometric effects of the thin film.

In contrast, the transparency of the presented PVDF-ITO detector can be seen in Figure 4.3. The green curve represents a spectrophotometer (Uvikon 931, Kontron Instruments) measurement on the same type of PVDF film used for the metal electrode transducers and the purple curve represents the measurement through the PVDF film in addition to both ITO electrodes. Both curves are affected by interferences which produce oscillations especially for the longer wavelengths. Below 400 nm, the ITO layers absorb strongly which reduces the transmission. At 532 nm the transmission is above 70 % allowing illumination through the detector film using that wavelength.

In this section the function principle via the piezoelectric effect will be presented. Subsequently it will be explained how the detector is designed and fabricated. This section ends with an analysis of the actual active area of the detector.

4.2.1 Piezo- and Pyroelectric Effect in PVDF

Polyvinylidene fluoride (PVDF) is a polymer often used as insulation for wires. Like many polymers PVDF is cheap to produce and easy to manufacture in a desired shape. However, unlike any other known polymer it exhibits an extraordinary strong piezoelectricity if treated accordingly, surpassing even some of the traditional piezoelectric crystals. Compared to detectors using lead zirconate titanate (PZT) as base material, PVDF detectors have a higher bandwidth [Xia13c],[Man84] and lack the problem of reverberation [Ora06].

In order to achieve these extraordinary properties, the PVDF film is mechanically stretched while a strong electromagnetic field is applied. This treatment, called poling, creates permanent electric dipoles in the direction of the applied field. When the polymer is deformed these dipoles are shifted, which creates an electrical potential that can be measured as a voltage (see Figure 4.4 right).

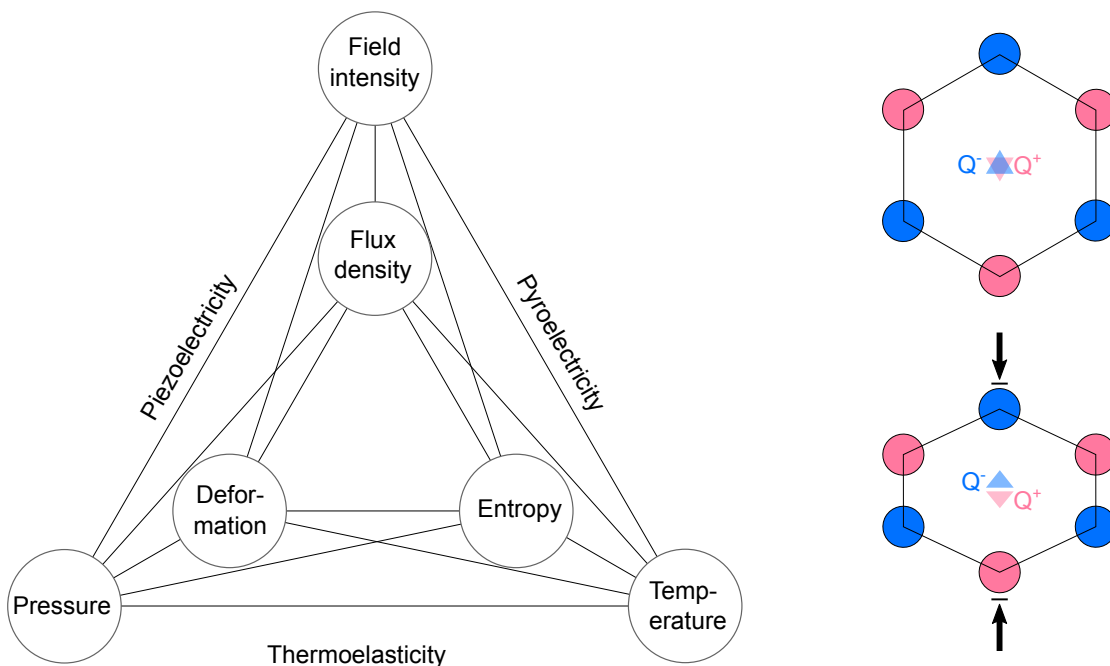


FIGURE 4.4: Left: Heckmann-diagram after [Loh98] visualizing the coupled effects in the piezoelectric detector. Right: Illustration of the principle of piezoelectricity. At the top, both centers of charge, Q^- (blue triangle) and Q^+ (pink triangle), lie on top of each other, indicating neutrality. At the bottom, deformation separates the centers of charge which creates an electric dipole.

Piezoelectricity refers to the conversion of pressure into voltage and vice versa. As the Heckmann diagram suggests, piezoelectricity is connected to thermoelasticity and pyroelectricity (Figure 4.4 left). The dipoles create a voltage regardless of how their charges

are shifted. For example, if the material is heated, the thermal vibrations yield a volume expansion which in turn produces a change in voltage. This effect is called pyroelectricity, sometimes also referred to as secondary piezoelectricity. The main difference between the two effects is that piezoelectricity works in both directions. Piezoelectric transducers produce a voltage when pressure is applied and create pressure when a voltage is applied.

Density	1780 $\frac{\text{kg}}{\text{m}^3}$
Longitudinal Sound Velocity	2250 $\frac{\text{m}}{\text{s}}$
Refractive Index	1.42
Piezo Strain Constant (thickness mode)	-30 $\frac{\text{pC}}{\text{N}}$
Maximum Usable Temperature	75-80 °C

TABLE 4.2: Properties of the biaxially stretched PVDF film. As written on the data sheet provided by Precision Acoustics.

4.2.2 Detector Design and Fabrication

In this thesis, the acoustic detector is made of a piezoelectric film (PVDF, see previous section) with electrodes sputtered on both sides. The form of the electrodes is designed to be smooth. Any sharp corner would yield local spikes in electric field intensity and thus make the detector more susceptible to disturbances, especially for high frequencies. As can be seen in Figure 4.5 on the left, the two electrodes overlap at the tips to form a circular area. This is the active area of the detector which is discussed in the subsequent section. To suppress crosstalk and parasitic effects between the conducting paths leading to the active area, their distance was chosen to be several millimeters.

Usually, electrodes are made from metal to ensure optimal conduction. However, for the design of the detector presented in this work it is essential for the electrodes to be optically transparent. Indium tin oxide (ITO) is one of the few materials which are optically transparent as well as electrically conducting. ITO is a n-type semiconductor with a band gap of $\sim 4\text{eV}$ [Kim99]. Thus, electromagnetic radiation in the visible and near infrared does not have enough energy for a band-to-band excitation, rendering ITO transparent in that wavelength range. At the same time, the carrier concentration is sufficiently high to facilitate electrical conductivity. These two properties make ITO the ideal material for the electrodes of a transparent transducer.

In the production of organic light-emitting diodes, known as OLEDs, sputtering is well established as a means to create a thin layer of ITO for the use as transparent top electrode [Tia11]. Utilizing the existing facilities and know-how of the *Institut für Hochfrequenztechnik* in Braunschweig, ITO was sputtered onto both sides of the 9 μm piezoelectric PVDF film described in the previous part. Sputter deposition is a form of physical vapor deposition where gas ions (here Argon) are accelerated by a magnetic RF field to form a plasma. From this plasma the argon ions are accelerated towards the ITO target by an applied voltage. The ions hit the target hard enough to ablate ITO particles which propagate, almost unhindered by the thin gas, through the chamber onto the sample (PVDF) positioned on the opposite side, see Figure 4.5. Obviously, this is not a directed particle beam, instead anything in that direction is covered by a homogeneous layer. The desired structure is created by a sputter mask that covers everything but the areas, intended to become the electrodes. To ensure that the mask is stable enough to be used in the production of several detectors it was cut out of a metal sheet. Due to the finite thickness of the sputter mask its inner walls throw a small shadow in their near vicinity.

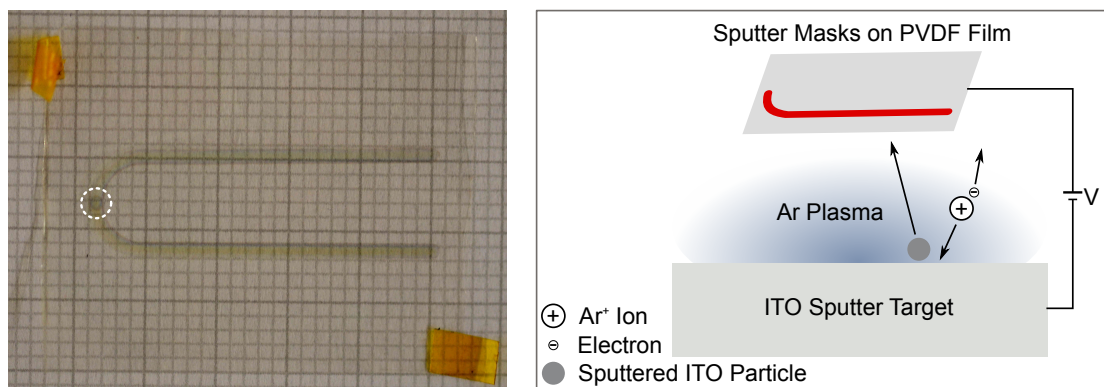


FIGURE 4.5: Left: Photograph of the detector film with enhanced contrast for visibility. The white circle highlights the active area. Right: Sketch of the sputter setup used for the detector production (after [Win11]).

The sputter process is depicted in schematic form in Figure 4.5 on the right. While not being disclosed, the sputter parameter such as gas pressure, sputter duration, and bias voltage were finely controlled following the protocol of OLED production. The temperature rise produced during the process is unknown. It is safe to assume that the temperature stayed below 80 $^{\circ}\text{C}$ which is the threshold where the PVDF film would lose its piezoelectricity.

4.2.2.1 Active Area

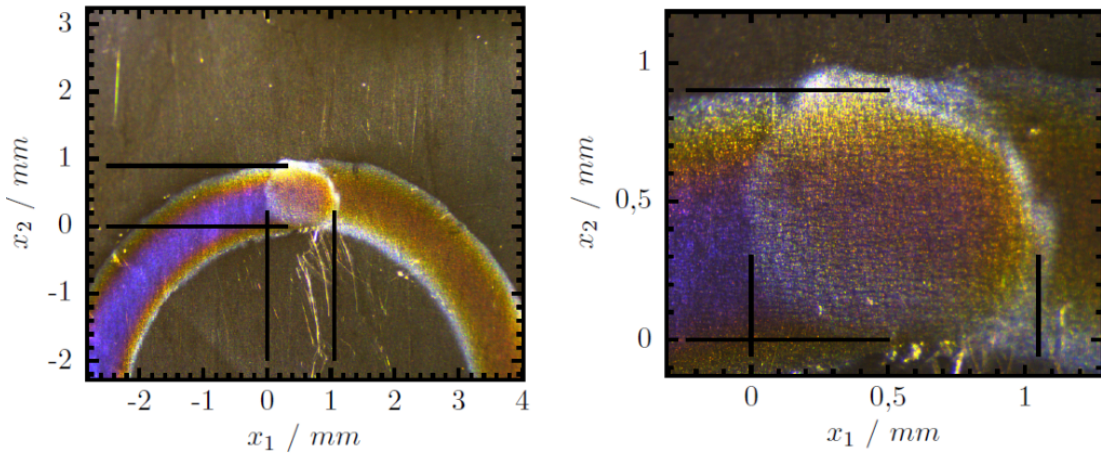


FIGURE 4.6: Microscopic views of the OA detector film at the location of the active area. The electrode overlap almost forms a circle but is slightly elongated in x_1 direction. The black lines represent the findings of the active area mapping measurement elaborated in the text. [Jon16]

To determine whether the active area of the OA detector matches the area where the electrodes overlap, Jonas Kanngießer, in his master thesis investigated the detector systematically. As was explained earlier, every piezoelectric detector that absorbs radiation, functions as a pyroelectric detector as well. By scanning over the detector film with a pulsed laser beam, the localized heating produces a pyroelectric effect at any place with finite absorption. From spectrophotometer measurements we know that the ITO electrodes increase the absorption, however the areas with bare PVDF film absorb as well and thus produce a pyroelectric field. Independently of the amplitude of the pyroelectric effect only the active area should produce a measurable signal. Voltages produced in an area without electrodes, cannot be detected due to the lack of an electrical connection to the data acquisition card. An interesting question was, whether the active area expands to the regions with only a single electrode as well as the possibility of the active area being smaller than the region of overlap.

Using a pinhole the beam diameter of the 532 nm laser pulses (~ 10 ns) from an optical parametric oscillator (OPO) (Ekspla PG122/UV) was reduced to 200 μm and directed at the detector film suspended in air without being attached to a sample. By tuning a 3-axis positioning stage the beam is scanned laterally over the detector film in steps of 100 μm . At each position 10 measurements are taken for averaging.

In theory, the self-designed sputter masks would produce an active area at the overlapping electrodes in the form of a circle with a diameter of 1 mm. The sputter masks are produced out of a metal sheet by laser cutting following a CAD-file design. Therefore, only marginal errors are expected from the masks themselves. However, the masks are placed on both sides of the PVDF film by hand which probably caused the deviations of the area of overlap from the planned design. As can be seen in Figure 4.6 the overlap of the electrodes does not form a perfect circle. In the pyroelectrical mapping of the active area (see Figure 4.7) these positioning errors cause the 0.1 mm elongation of the active area in the x_1 direction.

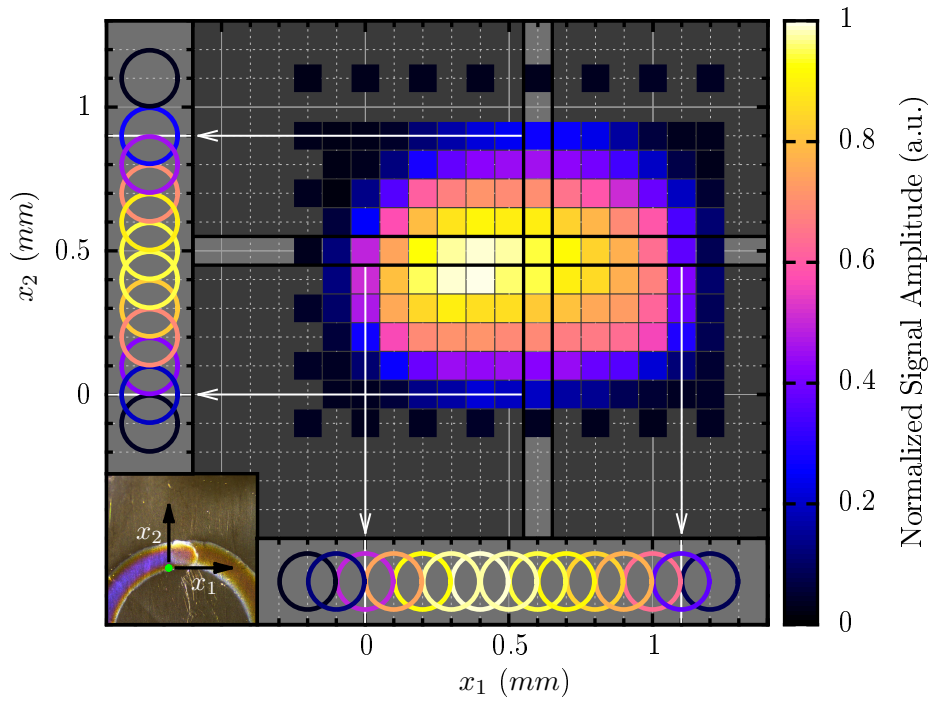


FIGURE 4.7: Determination of the active area of the OA detector: Map of intensity levels created by scanning a $\sim 200\ \mu\text{m}$ wide beam in $100\ \mu\text{m}$ steps over the detector. The overlap of the measurements is indicated with intensity colored rings next to the axis, representing the highlighted row and column in the graph. The active area extends approximately 1.1 mm in x_1 and 0.9 mm x_2 direction. Inset: Photograph of the detector at the overlap of the ITO electrodes, illustrating the scanning axes. [Jon16]

As can be seen in Figure 4.6, the electrodes appear lighter at the edges. This effect is likely caused by the metal masks casting a shadow during the sputter process. It is to be expected that any mask with a finite thickness will affect the sputtered layer in close vicinity to the inner side walls of the structure. Matching these fringe effects, the active area extends only 0.9 mm in the x_2 direction even though the masks appear well

aligned in that dimension. Probably, a combination of a slight misalignment and the fringe effects is responsible for the reduced extend in the x_2 direction.

Overall the active area is in good accordance with the expectations and the deviations are understood and do not affect the OA signal. More importantly this shows that the active area can be determined visually without the need of elaborate measurements.

4.3 Optoacoustic Setup

In this section the OA measurement setup is elaborated. Following the description of the electrical preamplifier, the process and setup for the energy calibration is explained. Finally, the OA setup used in all measurements and the different detector configurations are presented in detail.

4.3.1 Electrical Preamplifier

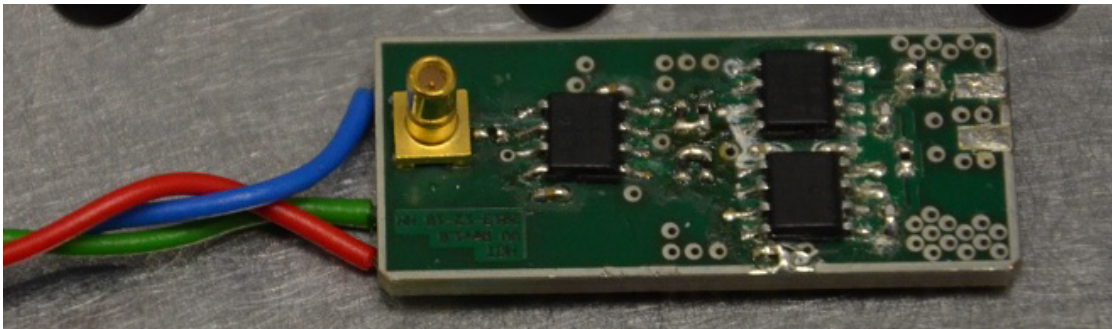


FIGURE 4.8: Photograph of the custom build preamplifier.

To ensure that the preamplifier meets the demands imposed by the setup, we worked in close cooperation with *taberna pro medicum GmbH* (tpm) who developed the signal amplifier according to our specifications. Especially in the beginning of the experimental work the form of the signals and, thus, the occurring acoustic frequencies, were not well known. Although it is possible to determine the frequency response and eliminate its effects in post-processing, we decided to sacrifice high amplifications for a constant amplification over a broad band of frequencies. After developing the circuit board an amplification of 6 dB over a frequency range of more than 200 MHz was determined, which is greater than any expected signal would require.

The symmetric design allowed for the desired functionality independent on the orientation of the detector film. Note that, it is not possible to confirm the piezoelectric orientation of the film before installing it in the OA setup. While the orientation is marked on the film at first it is likely that it will get lost in the sputter process. Fortunately, due to the symmetric design the orientation merely changes the sign which is convenient in the data processing. As can be seen on the left-hand side of Figure 4.9 the input impedance is chosen high ($97.6\text{ k}\Omega$) to ensure a good sensitivity despite high resistivity values of the ITO electrodes. To suppress electrical ringing, 0.5 pF capacitors are included in the feedback loops of the operational amplifiers. A regulated power supply (PeakTech 6210) was chosen to ensure that the signal is not altered by variations in the applied voltage.

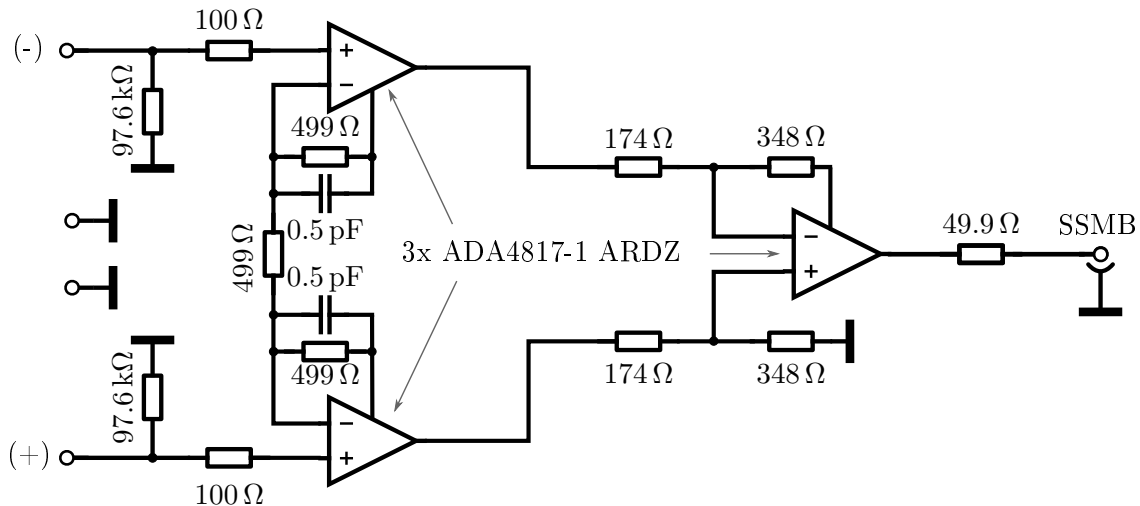


FIGURE 4.9: Layout of the circuit board for the preamplifier as used in this work.

4.3.2 Energy Calibration and Monitoring

Any laser source exhibits energy variations to a certain degree. Depending on the optical components used down the beam path the energy uncertainty is increased further. Especially when aiming at clinical use, it is highly important to monitor the energy in order to stay within the safety limits. As described earlier (see Section 3.1), the amplitude of the OA pressure wave depends linearly on the absorbed energy through the Grüneisen parameter. Thus, the irradiation energy is an important element in the understanding of the resulting shape of the OA signal.

Energy can be measured directly by directing the beam at a calibrated photo diode or a pyroelectric detector. However, it is not feasible to conduct such straight forward energy measurements and illuminate the sample at the same time. To circumvent this predicament a second indirect measurement is implemented that correlates with the output energy but is not impeding the beam from reaching the sample. By measuring the energy directly and indirectly at the same time the indirect measurement can be calibrated.

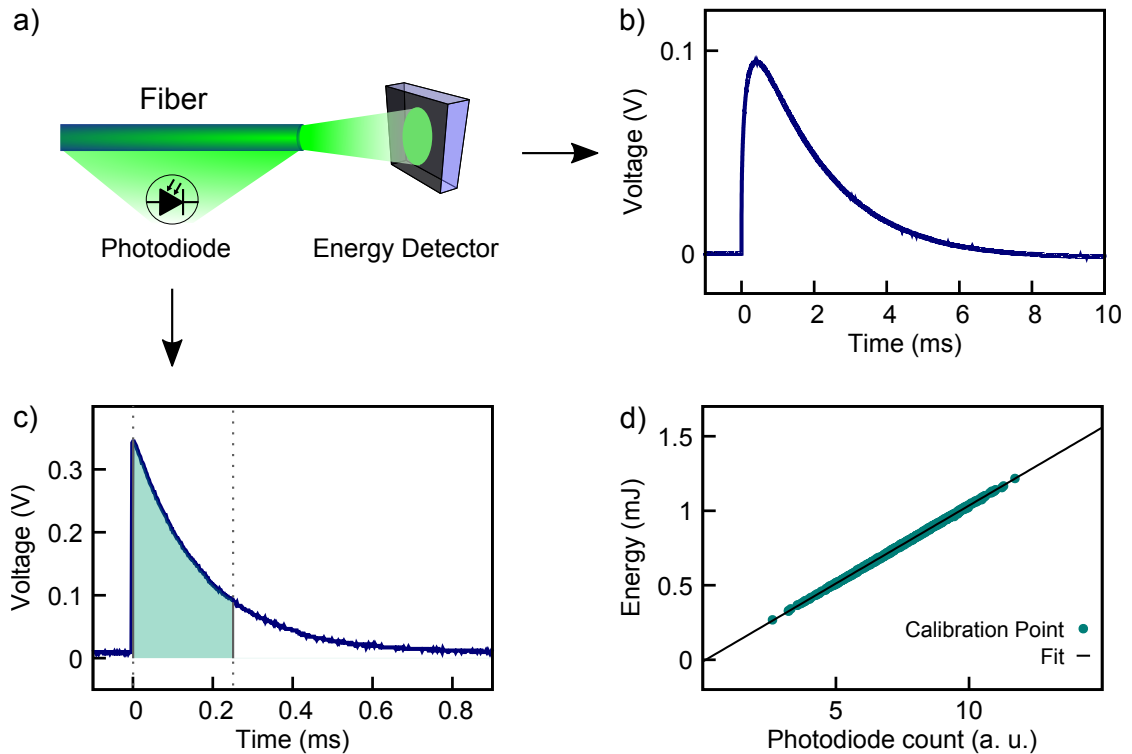


FIGURE 4.10: The energy calibration relates the actual energy leaving the fiber with the intensity of stray light measured by a photodiode next to the fiber. a) Setup for energy calibration b) Maximum voltage measured by the energy detector (pyroelectric absorber) corresponds to the pulse energy. c) Temporal integral over photodiode signal creates reference value proportional to the energy. d) Energy calibration with 1000 measurement points. Fit shows linearity and good agreement.

Energy Monitoring Setup

In our case the illumination is fiber-based which renders the use of beam splitters for the energy calibration setup inconvenient. To obtain an indirect measurement of the pulse energy a photodiode is placed next to the fiber. Through the transparent fiber jacket a fraction of the light is coupled out and detected by the photodiode. The amount of this stray light can be increased by bending the fiber, however, this leads to a dependence

on the room temperature corrupting the precision. By logging the temperature of the laboratory, we managed to remove this effect in postprocessing [Jon16].

Fortunately, the photodiode used (S1336-18BQ, Hamamatsu Photonics) is very sensitive at the relevant wavelength. By running the photodiode with 5 V reverse bias, the signal is strong enough even when working with an unbent fiber. Thus, while working in the visible spectrum we refrain from bending the fiber. Figure 4.10 shows the reference measurements which are used to correlate the diode signal with the actual puls energy leaving the fiber.

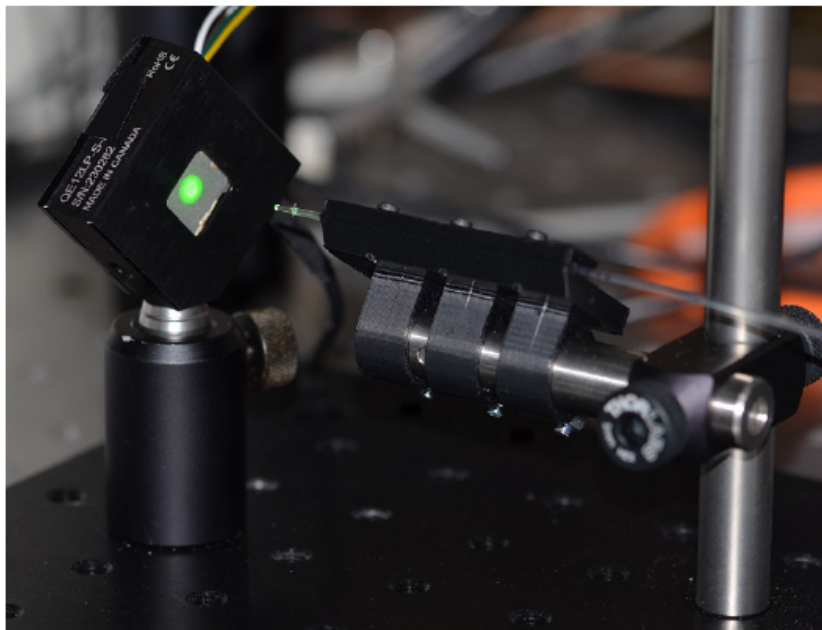


FIGURE 4.11: Photograph of the pyroelectric detector used to calibrate the system.

4.3.3 Beam profile

For the illumination the laser is coupled into a multimode fiber which determines the beam profile. The OPO (NL303G + PG122UV, Ekspla, Lithuania) produces a very unsymmetrical energy distribution with high intensity regions and even local minima. However, due to the long path through the fiber of more than 10 m which leads to mixing of all modes, the pulses become homogenized as can be seen in Figure 4.12. The *Ultra 50* laser source produces a much better beam shape, however, after the long fiber the result is the same. The beam exhibits a flat-top profile. In contrast to top-hats profiles, the flat-top profiles have smooth flanks leveling off from the center of constant intensity. For a detailed description and visualization of the influence of the beam profile on the signal shape, please refer to Section 3.2.

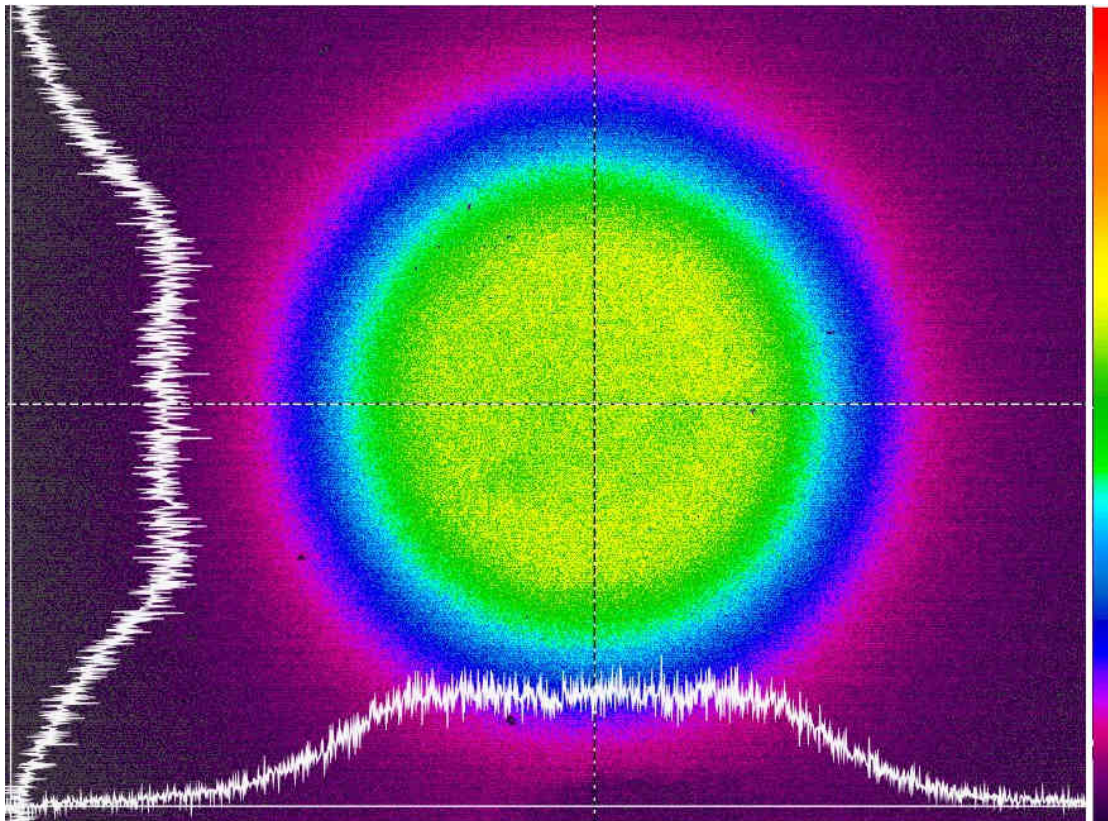


FIGURE 4.12: Beam profile after more than 10 m of fiber, as measured with a beam profiler (LBP2-VIS2, Newport).

4.3.4 Optoacoustic Measurement Setup

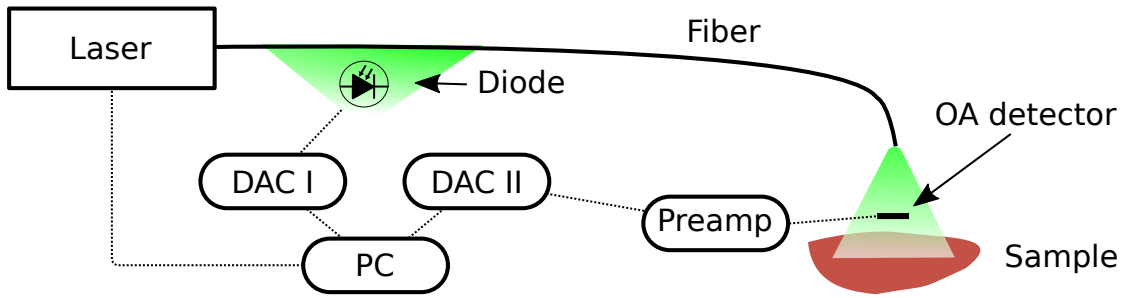


FIGURE 4.13: Sketch of OA measurement setup. DAC stands for data acquisition card. DAC I is used for the energy monitoring as described earlier.

In the process of this thesis multiple setups were created which mostly differ in the specific use of the detector film. Subsequent to this section, the different detector setups will be elaborated. Here, the core elements of the OA measurement setup are presented. Two laser sources were utilized. In the beginning an optical parametric oscillator, OPO (NL303G + PG122UV, Ekspla, Lithuania) was used. For optoacoustics, the visible beam exit producing 3-6 ns pulses in the wavelength range 420-709 nm was used. Depending on the wavelength the energy varied from a few hundred microjoule to several millijoule. To ensure sufficient energy, most measurements were done with 532 nm resulting in energies of approximately 1 mJ after the fiber.

Later, a compact single wavelength laser at 532 nm was utilized (Ultra50, Quantel Laser, France), in particular, for the use in clinical measurements. Independent of the specific setup the laser was controlled by an OA-software, programmed in close cooperation with *SciResolve* and configured exclusively for our hardware configuration. In the PC which controlled the process two data acquisition cards are included, one (DAC-I) for the energy calibration and monitoring as described earlier (ADLINK PCIe 9814) and another (DAC-II) for the recording of the OA signal (Agilent U1065A, up to 8 GS/s). It is noteworthy that high requirements have to be met by DAC-II. The card achieves a sampling rate of up to 8 GS/s which is expected to record any OA signal with sufficiently high temporal resolution. All setups presented in this work are fiber based. Setups using the OPO include a 10 m long fiber needed to guide the pulses from the bulky laser source to the setup. The Ultra50 laser source on the other hand is small enough to be accommodated close to the experiment. Furthermore, a commercial fiber coupling module is attached to the Ultra50 laser source facilitating significantly higher coupling efficiencies compared to the self-built coupling used with the OPO.

4.3.5 Detector Setups

In this section the different detector setups are presented. For all the setups the same design of the detector film with ITO electrodes was used. The data acquisition setup connected to the preamplifier is also the same for all measurements. The main difference regarding the functionality of the detectors is the backing layer. In case of the setup used in the Angular study hydrogel was employed, for the clinical measurements PMMA was used.

Angular Study

To analyze the detectors capability to measure signals arriving from different directions as well as first off-axis measurements in the far-field, a short study was performed in which the source volume was moved underneath the detector film. For this, so called Angular study, a special setup was created using a 3D-printer. All setups have the vertical holder for the preamplifier in common which can be seen in Figure 4.14 (left).

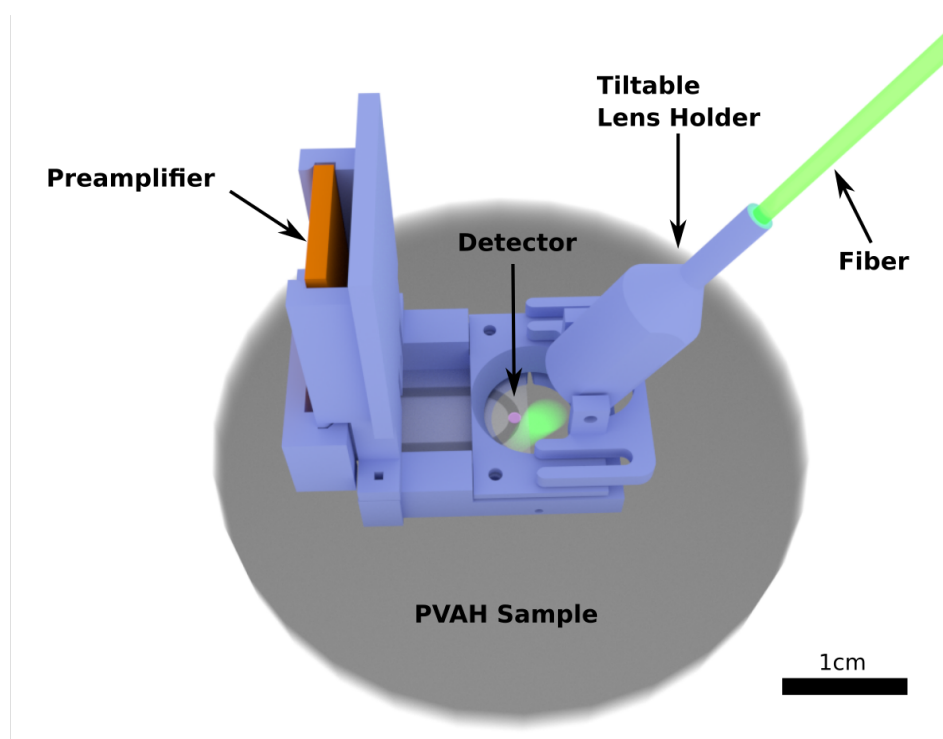


FIGURE 4.14: Sketch of the OA setup for the Angular study to investigate off-axis measurements. Inside of the tiltable part on the right the fiber is directed at a single collecting lens. The active area is highlighted in purple. For clarity the PVAH backing layer on top of the detector as well as the data and power cables from the amplifier were omitted.

The ITO electrodes of the detector film are fixed to the contact pads of the preamplifier by plastic screws covered with softer plastic to prevent damage of the film. A 3D-printed frame is connected to the holder of the preamplifier so the side of the detector film can be fixated. For illumination an attachment was created which facilitates tilting the fiber holder. The hole in the narrow side around the fiber is tight so no further fixation is needed. Inside the holder, the hole widens to accommodate the single collecting lens with a focal length of 10 mm. Due to the finite extent of the fiber facet (800 μm) and the diverging beam path the beam waist is approximately 3 mm in diameter. The actual spot size at the absorbing layer might be deformed by refraction at the sample surface. However, simulation assuming a spot size of 3 mm recreates the measurements well (see [Mel]). The experimental measurements are presented in Chapter 5.1.2.

The necessary backing layer which consist of a piece of PVA-H put on top of the detector is not included in the figure. In theory, the detector film is thin enough compared to the relevant acoustic wavelengths so that it becomes acoustically transparent if brought in between two layers with the same acoustic properties [Jae05]. For measurements on living tissue, PVA-H is a close match in acoustic properties and can be used as backing layer. However due to the high cost in time and effort to create the hydrogel and keep it wet and at the right position during measurements we chose a different setup for the clinical measurements which is presented in the subsequent section.

Clinical OA Setups

For clinical use the detector setup needs to satisfy the following demands, that mostly concern the area of contact with the patient. a) The contact area must not be larger than a few centimeters, otherwise many regions on the body cannot be reached. b) The contact area must withstand repeated use with the associated mechanical strain as well as cleaning with disinfectant. c) All parts of the measurement head must be fixed so they stay in position when measurements need to be taken, for example, from underneath the patient. d) The detector film must be visible at all times, to ensure proper positioning on the nevus. e) The detector setup should be light and small enough to be operated with one hand, which not only simplifies the measurement procedure but reduces the effort of grounding the experimentalist greatly.

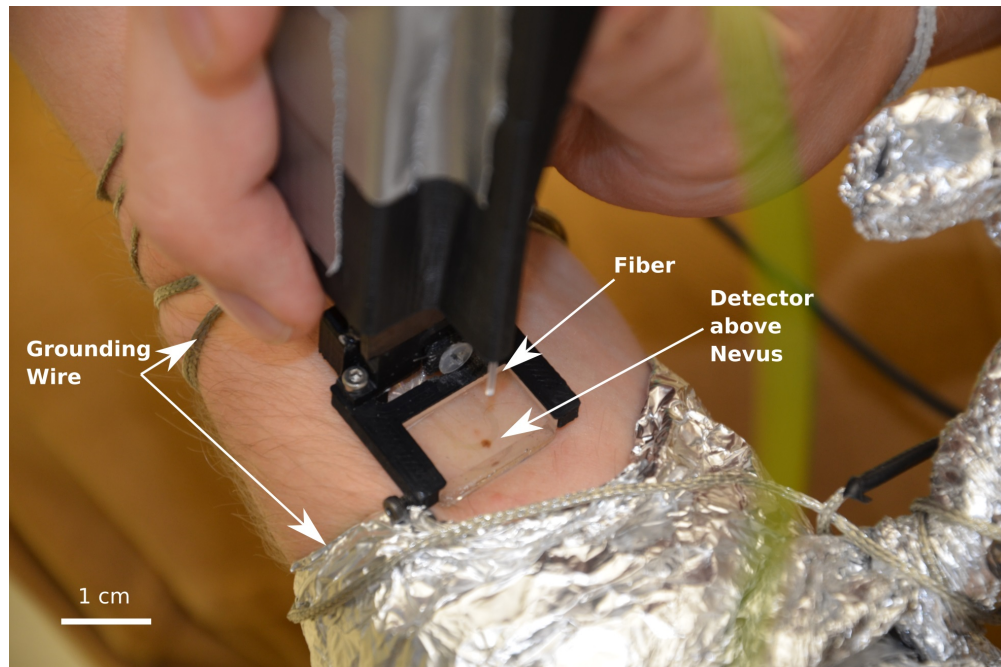


FIGURE 4.15: Photograph of handheld clinical setup. To both sides of the OA setup the patient grounding is visible. Due to its transparency the active area of the detector film cannot be seen above the nevus.

While hydrogels are well suited as a backing layer for their acoustic similarity to living tissue, they are impractical with respect to the actual measurement procedure in the clinic. Due to their consistency they cannot be fixated and need to be kept wet throughout the process. Instead a 5 mm thick piece of PMMA glued on top of the detector functions as backing layer. To protect the detector film from mechanical strains a second PMMA sheet was glued underneath. In all cases the high precision optodic bonding was performed by Maher Rezem [HOT, internal communication] using Norland Optical Adhesive (NOA 85V) which is highly transmissive for visible light. The adhesive was cured using UV radiation at a wavelength of 365 nm over a time of approximately 15 min. Based on similar bonding processes the thickness of the adhesive layer is estimated to be between 10 μm and 50 μm . Although PMMA itself is not ethanol resistant, repeated cleaning and disinfecting had no visible effect on it. During the clinical measurements, a nonalcoholic cleaning solution was used, which was provided by the physician.

In Figure 4.15 the clinical setup is depicted. The plastic case holding the preamplifier and the illumination fiber (880 μm) was produced with a 3D-Printer. Using the backing layer, the detector film was fixed to the setup by being skewed to a frame. The drilling hole holding the fiber was created tight enough to keep the fiber in position at 18 mm above the active area.

4.4 Signal Processing

In this section the processing from raw data to the OA signal is described. Depending on the setup only specific post-processing steps are needed.

4.4.1 Subtraction of Electromagnetic Noise

The Nd:YAG lasers used in this work are pumped by flashlamps and are q-switched. Due to the large currents needed to run the laser, strong electromagnetic noise is emitted. Any sample and especially the human body, functioning as an antenna picks up this signal and conveys it to the OA detector to produce parasitic signals. In the case of the Ultra 50 laser source which is used for the clinical measurements this unwanted radiation is small enough so that proper grounding of the patient and the signal cable in combination with placing the laser in the opposite corner of the room is enough to reduce the noise to an acceptable level.

On the other hand, the Nd:YAG pump laser of the OPO used for the measurements with variable wavelengths produces such massive parasitic signals that it has to be subtracted in post-processing. To achieve that, reference measurements with blocked illumination beam were performed before and after the regular measurements. Unfortunately, the form and amplitude of the parasitic depends strongly on small changes in the positioning and grounding of the patient which signifies that the patient must remain in the same position throughout the measurements. Even slight repositioning of the wires used for the grounding may render the dark measurements unusable for the subtraction process afterwards.

In principle, a single dark measurement would suffice. However, to monitor whether the noise changed over the time of the experiment at least two measurements are needed. Here, we measured the noise with blocked illumination at least twice before and twice after the measurement series to be able to obtain a reliable background. Variations in trigger times, up to half the oscillation period of the parasitic signal, lead to shifts in the background noise which in turn yields significant errors in the background subtraction. To avoid this effect the measurements are synchronized by shifting the background so that the maxima of a specific peak overlap. By comparing the different background signals, deviations were found which cannot be explained by the trigger shift. Possible

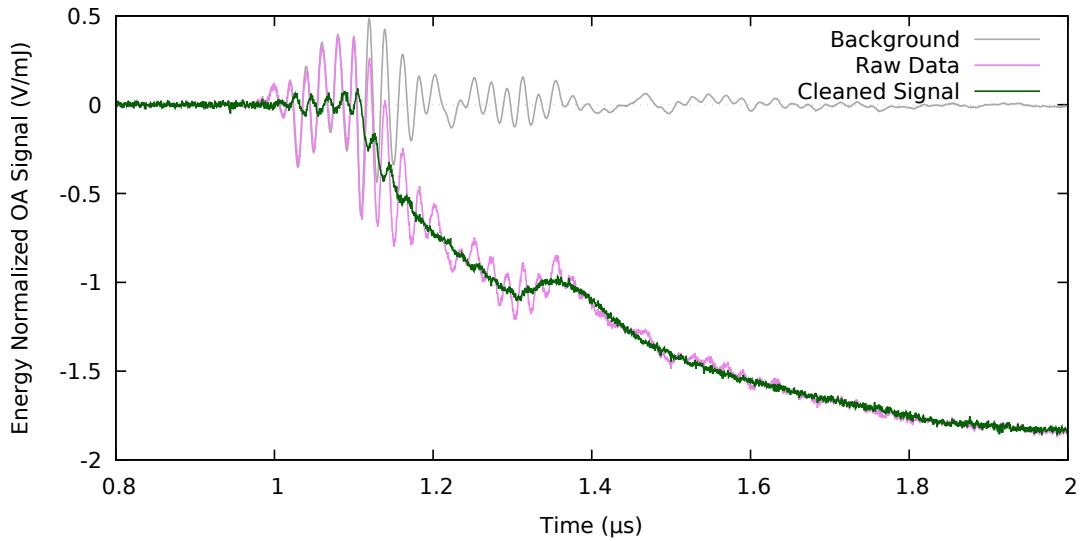


FIGURE 4.16: Exemplary subtraction of background signal created by the OPO system. The noise begins around the trigger time and extends several hundred nanoseconds into the signal. Its magnitude is often bigger than the OA signal at 1.3 – 1.5 μs .

contributors are pulse to pulse differences in the electronic q-switch driver or the flash-lamps. It is important to prevent changes in the grounding in between measurements, as this will change the pickup characteristics which in turn may lead to parasitic signals of various frequencies. Fortunately, even when measuring with the OPO laser source the remaining wiggles of the parasitic signal, after background subtraction, are small compared to the OA signal itself. However, as will be elaborated later, the recorded signals are a convolution of the OA signal and the instrument response function. Therefore, in addition to the noise subtraction, a deconvolution algorithm is used in order to reconstruct the original OA signal. This process is highly sensitive to the wiggles in the parasitic signal and ultimately prevents a comprehensive signal reconstruction for measurements using the OPO.

4.4.2 Removal of the Pyroelectric Signal

To measure in the near field we created a transparent transducer through which the sample could be illuminated without the need of complex optics to guide the laser pulse around, as must be done otherwise [Wan09]. However, any real material has a finite absorption and so does our detector. As described earlier, when piezoelectric materials absorb energy and, thus, are heated, the pyroelectric effect creates a signal, here called Pyro. The Pyro in the case of measurements on human skin far exceeds the magnitude

of the OA signals. Unfortunately, the size and form of this effect depends on several parameters, most of which cannot easily be controlled. For instance, the added capacity of the surrounding material of the active area, such as distilled water, affects the measurements of PVDF membrane hydrophones [Bac82]. The influence of the capacity, in the context of the OA detector presented here, will be addressed later in exemplary manner. This in practice unpredictable behavior necessitates the removal of the pyroelectric effect. Removing it by suppressing the relevant frequencies is sensitive to errors because neither the frequencies of the Pyro nor the OA signal are exactly known, and an overlap exist in many cases.

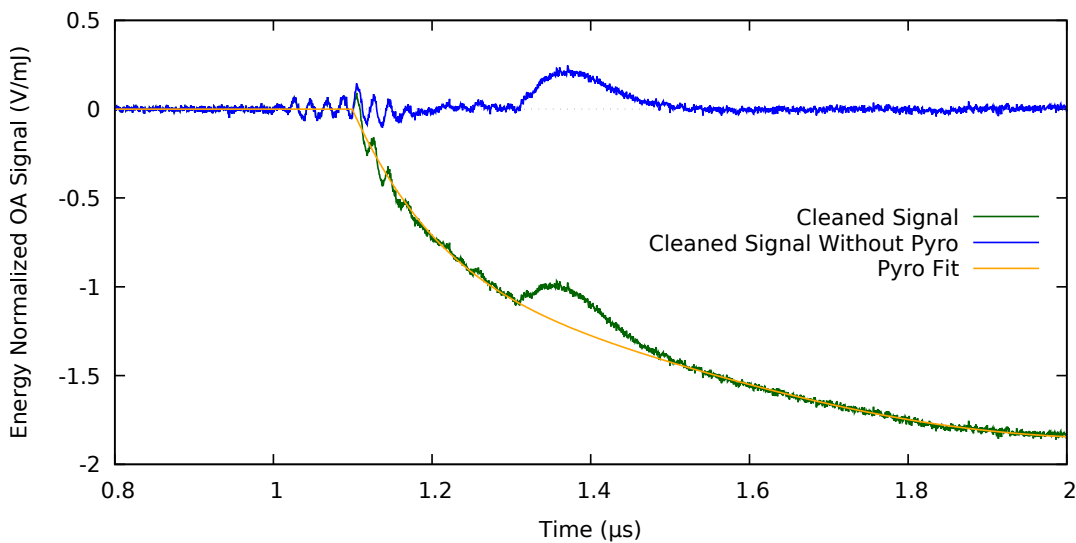


FIGURE 4.17: The pyroelectric signal is removed by subtracting a polynomial fit of 10th order. The resulting data should only include the OA signal.

However, it is possible to fit a curve to the pyroelectric signal, which can be used to subtract it afterwards. Fitting the progression of the pyroelectric signal is facilitated by the use of a fronting layer. This layer defines a time period after the trigger in which the OA signal cannot yet arrive at the detector. In the case of our detector, the first $0.2\mu\text{s}$ of the signal after the arrival of the laser pulse at the sample, only contain the background noise and the pyroelectric signal. Even if the background noise could not be removed completely by the aforementioned method its oscillating behavior is averaged out during the fitting procedure. While in theory the underlying physical effects in first approximation of the Pyro can be described with exponential functions, we found that a universal approach produced much better results. Thus, a polynomial function of 10th order is fitted to the measurement omitting the regions expected to feature pronounced OA signals. To use the time after the OA signal, its endpoint must be determined for the

individual measurement and the sample used. Only the transition time of the acoustic wave through the fronting layer can be used for the process of fitting independent of the sample. The resulting curve after subtraction of the pyroelectric signal can be seen in Figure 4.17

In an earlier setup it was necessary to remove voltage offsets produced by differing grounding levels depending on whether the wall plug or the grounding of the optical tables was used. Even though revised grounding methods superseded those needs, any post-processing software contains lines which determine the level of the pre-trigger signal and subtract it from the complete measurement.

Chapter 5

Results and Discussion

In this chapter the results of the OA measurements are presented and discussed. First, the measurements on layered hydrogel phantoms are shown and compared to simulations based on the code by Oliver Melchert [internal communication]. Afterwards the effect of diffraction is illustrated in an angular study on a single hydrogel absorber layer. Subsequently, in Section 5.2 the impact of parasitic capacities on the pyroelectric signal is visualized. At the end of the section it is shown that the pyroelectric signal amplitude correlates well with the energy absorbed in the detector film. Section 5.3 contains the details and the validation of the deconvolution method used for measurements with the clinical detector setup. Finally, in Section 5.4 the in-vivo measurements on human skin are presented. To show the potential of wavelength scans in OAs an exemplary measurement series using the OPO as laser source is briefly elaborated. However, the utilization of this particular OPO introduces too much noise to the signal so that it was not used in the clinical measurements. This chapter concludes with the presentation of the clinical measurements which were conducted in the framework of the MeDiOO project.

5.1 Layered Phantoms

To validate the intermediate steps toward a handheld OA device for clinical application, earlier versions of the transparent detector were used for measurements on layered hydrogel phantoms (see Section 4.1). PVA hydrogel (PVA-H) has acoustic properties which, due to the high water content, are close to those of living tissue. Additionally, the PVA-H can be created transparent and by adding absorbers it can be used for OA measurements. To match the acoustic properties of the samples, hydrogel was used as backing layer for measurements on PVA-H phantoms. Because the piece of hydrogel placed on top of the active area is not plane, the illumination could not be directed through the detector itself. For the illumination from the side, space between detector and sample is needed which sets the measurement into the far field regime (see Section 3.2).

5.1.1 Far Field Measurements of Multiple Layers

In this section, far field measurements of layered PVA-H phantoms are presented. The samples were created by stacking 1 mm thick layers with different absorber concentrations. To validate the resulting signals, they were compared to simulated data. Based on the Poisson integral in cylindrical polar coordinates, the numerical simulation was customized to efficiently calculate the pressure propagation in layered media. This thesis focuses on the experimental side of these experiments, please refer to [Blu16] for additional information on the numerical simulations.

As depicted in Figure 5.1 the only optical component involved is a multimode fiber (Ceramoptec, Optran WF 800/880N, 800 μm core diameter, NA 0.22) through which the laser pulses from the OPO are guided. At a wavelength of 532 nm the light pulses are visible, and the positioning could be done by hand. The fiber was positioned in a way that allowed the excitation to occur as close to the detector normal as possible without illuminating the active detector area, which means a steep angle and close vicinity. As backing layer, a piece of PVA-H was placed on top of the detector. The surface of the PVA-H piece is irregular. To prevent deformation of the illumination pulse by refraction, the backing layer was aligned to end shortly after the detector edge and to allow the laser pulse to enter the sample through a planar surface next to the detector (see Figure 5.1).

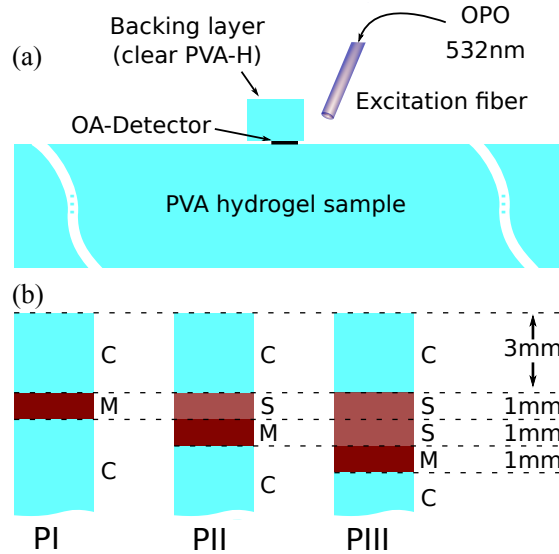


FIGURE 5.1: Sketch of a) the experimental setup and b) the three different tissue phantoms PI, PII and PIII. The label “C” stands for clear PVA-H while “S” represents a low and “M” a high melanin concentration. (As created for [Blu16])

The detector was placed directly on a 3 mm thick clear PVA-H layer. For phantom PI a 1 mm thick layer of PVA-H with a high concentration (45 mg see Section 4.1) of melanin followed. The high concentration layers are labeled with the letter M , representing the “melanoma” part of the skin. Underneath the absorbing layer a thick layer of clear PVA-H is placed to prevent acoustic reflections from the bottom of the sample to interfere with the measurement. In contrast to PI, Phantom PII has a 1 mm thick layer of PVA-H with a low melanin concentration (4.5 mg) on top of the M layer. The low concentration layer is labeled S , representing the “regular skin”.

In the case of PIII this low concentration layer is 2 mm thick. Obviously, it is unrealistic that a melanoma is covered by 1 mm or more of regular skin. However, the idea is to show the capability of measuring changes in absorption in addition to the thickness of a single layer. In theory one could determine the absorption profile of a layer with high followed by a layer with low concentration as well. However, in practice the back-end signal is too small to be detected. Please note that the absorption in the M and S layers is much smaller than in melanoma or skin. Higher concentrations of melanin yield irregular clustering which prohibits a controlled and homogeneous absorption coefficient in the hydrogel. On the other hand, as discussed earlier, synthetic melanin was used which exhibits lower absorption compared to natural melanin anyway. Nonetheless the measurements on these phantoms validate the capabilities of the detector film.

In Figure 5.2 OA measurements on the three phantoms are compared. Using a sound velocity of 1500 m/s the OA signal was plotted over depth instead of time. All signals were shifted so the first absorbing layer begins at 0 cm. In the case of PI where the only absorbing layer is of high concentration this leads to a steep peak followed by a shallow valley and ends with a minor dip. The leading flank represents the onset of the absorption. While the created pressure profile in the M layer would follow the Beer-Lambert law, the detected OA signal is deformed by diffraction. Instead of an exponential decay the signal drops below zero and slowly rises again. The dip at 0.4 cm denotes the end of the absorbing layer. Between 0.5 cm and 0.65 cm a second and much broader dip is visible. Most likely this feature is caused by reflections from inside the backing layer. Due to the uneven form of the backing layer, reflections are spread out and the signal is broadened. The simulated data (blue dashed line) does not include a finite backing layer, thus, it remains at zero after the back-end dip.

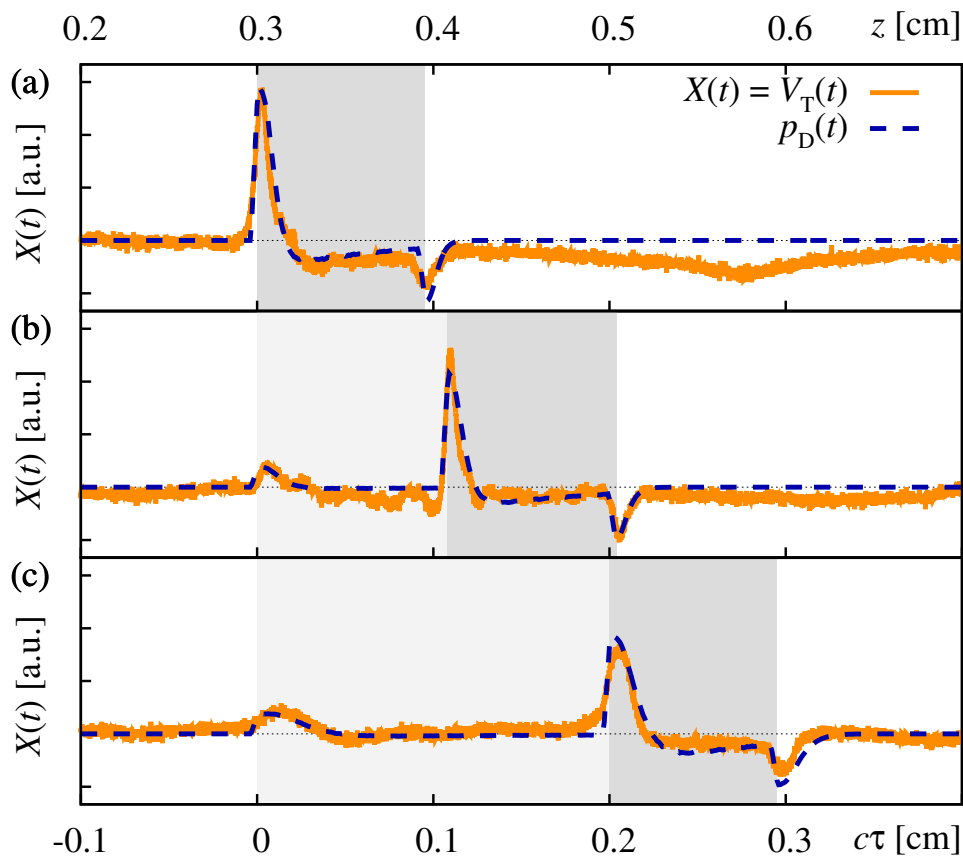


FIGURE 5.2: Comparison of OA signals of a) PI b) PII und c) PII. Experimental (yellow) and theoretical (blue) results agree well in all features of the far field measurements [Blu16]

The leading peak in the measurement curve of PII, originating in the S layer, is much smaller than for PI. As described in Section 3.1, the OA signal amplitude is proportional to the absorption coefficient. At 0.4 cm the onset of the M layer produces a tall peak in accordance with the higher absorption coefficient. Following the small diffraction valley, the dip at 0.5 cm indicates the back-end of the M layer. Please note, that a low frequency oscillation overlays the signal even before the OA signal arrives, in the case of the OPO it is quite substantial in amplitude. This is likely a parasitic signal, picked up from the laser pump or the cooling system. In addition to slight inhomogeneities in melanin distribution the parasitic signal explains the difference between experimental and simulated data from 0.3 cm to 0.4 cm.

Finally, the OA measurement on PIII exhibits a small bump representing the beginning of the S layer followed by a stretch of almost zero amplitude only disturbed by the aforementioned pickup. The peak at the onset of the M layer is bigger than the S layer bump. However, it is small compared to the M layer peaks for PI and PII. The lower intensity of the light passing through 2 mm of S type PVA-H and the further widened beam, both explain the reduced signal. Intuitively, scattering might contribute to a reduction of the light reaching the M layer in PIII. However, scattering is not included in the simulation and the agreement between the two curves suggests that it plays a minor role.

Small deviations from the expected thickness of 1 mm for the individual layers can be explained by compression of the soft samples caused by the weight of the setup pressing from above. Another contribution to the differing thicknesses is the fact that hydrogels may exhibit different sound velocities even when they are produced according to the same recipe. By converting the time-based experimental signal to the depth-based signal as presented here, these speed variations translate to thickness variations.

Overall simulation and measurement data agree very well for this far field experiment. This illustrates the validity of the assumptions with respect to the detector setup. Additionally, it shows that this simple setup is capable of producing signals that represent physical facts without too much noise or parasitic signals.

5.1.2 Investigation of Angular Dependence of OA Signals (Angular Study)

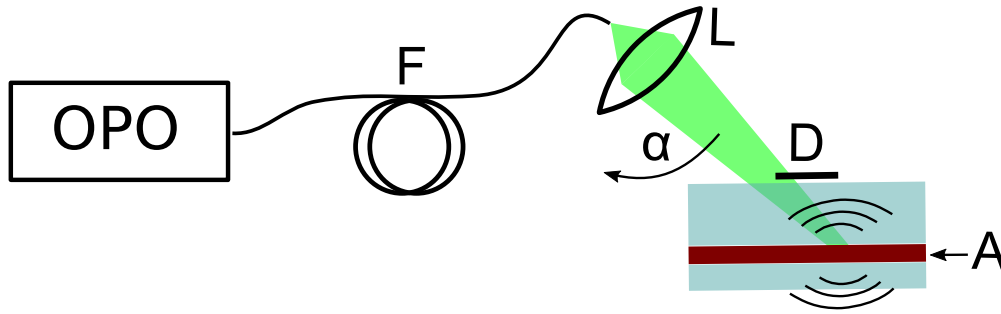


FIGURE 5.3: Sketch of setup for the investigation of the angular dependence of the OA signal. After passing the fiber (F) the laser beam is focused by a single lens (L) into the PVA-H sample. By changing the illumination angle the beam is moved over the absorbing layer (A) containing melanin (see Section 4.1). The detector is labeled D and the rotation angle α . The PVA-H backing layer on top of the detector is not shown to increase clarity.

As can be seen from the sketch in Figure 5.3 the setup includes a single lens which focuses the laser pulses at a wavelength of 532 nm into the sample. A detailed description of the measurement setup can be found in Section 4.3.5. The sample consists of PVA-H layers, starting with 13 mm of clear hydrogel followed by 1 mm of absorbing layer created with 4.5 mg melanin, which leads to comparably low absorption (see Section 4.1). At the bottom the phantom ends with 2 mm of clear PVA-H. The focus of the laser beam pulses is widened by the extent of the fiber end facet as well as refraction at the sample surface. Using fine scaled paper, the beam diameter at the depth of the absorbing layer was determined to be approximately 3 mm. Whenever the distance between detector and source is large compared to the lateral extent of the source volume the measurements are considered to be in the far field. As explained earlier far field measurements are affected by acoustic diffraction, deforming the original pressure profile to resemble its first derivative.

For angles between 60° and 75° the illuminated source volume is underneath the detector and the curves can be compared to the examples of on axis measurements in the preceding section. After a leading compression peak representing the beginning of the absorbing layer a diffraction valley follows. At approximately $0.7 \mu\text{s}$ the small rarefaction dip is in accordance with the lower boundary of the 1 mm thick absorbing layer assuming a sound velocity of $\sim 1500 \frac{\text{m}}{\text{s}}$.

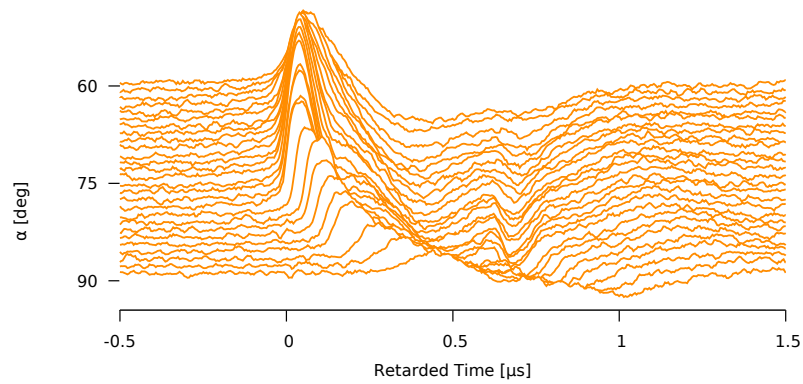


FIGURE 5.4: OA far field measurements showing the effects of acoustic diffraction. Some measurements are shifted in time to compensate for thickness variations of the top PVA-H layer (see text). The leading compression peak represents beginning of the absorbing layer and is followed by a rarefaction valley caused by diffraction. At approx. $0.7 \mu\text{s}$ a rarefaction dip indicates the end of the absorbing layer.

The data for the plot was smoothed and some of the curves had to be shifted to compensate for runtime variations caused by changes in the pressure with which the detector setup was placed on the sample. Unfortunately, it is not feasible to fix the setup to prevent these variations due to the flexibility of the 3D-printed polymer as well as the non-ridged detector film and backing layer.

Nonetheless, after shifting the datasets the systematic changes of the curves with different angles become clear. While at smaller angles ($60\text{--}75^\circ$) the curves are quite similar, towards 90° the appearance of the curves changes. The increasing lateral distance yields a delay of the leading flank. Not only the position changes but the form as well. Off the normal direction of the layer the plane wave components vanish, and the amplitude decreases greatly. This results from the change of the characteristic geometry of the source volume from the perspective of the detector. Simply put, instead of a plane surface underneath the detector observes the source volume from the side.

5.2 Analysis of the Pyroelectric Effect

The central novelty of the setup presented here is the capability of measuring under near field conditions. To achieve that the detector is brought in close vicinity of the sample while the illumination is directed through the active detector area itself. This circumstance introduces a pyroelectrical signal to the measurements. In this section the influence of the sample as a parasitic electrical capacity is described. First, this was done using a metal plate as sample, then the measurements were performed on different persons.

As described earlier (see Section 4.2.1), any piezoelectric sensor is also susceptible to temperature variations which produce a thermal expansion that in turn causes a pyroelectrical signal. When illuminating the sample through the detector, as performed in the clinical study, the OA signal is overlaid with the signal from the pyroelectric effect. Even though it is not the desired signal it can be used to monitor the energy of the laser pulse.

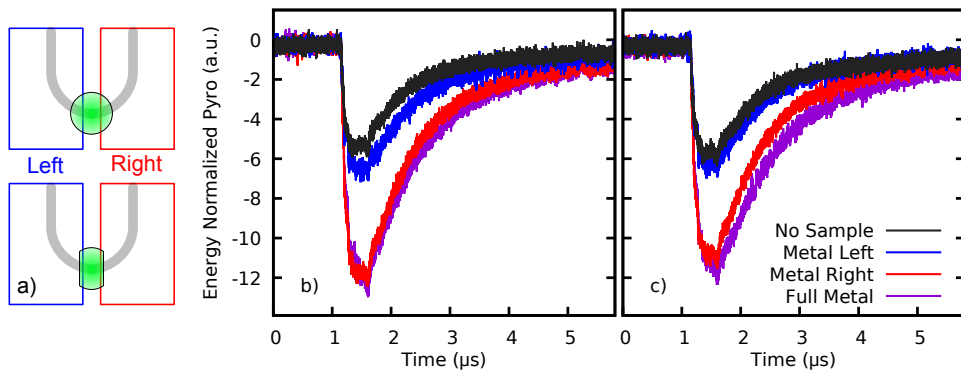


FIGURE 5.5: Influence on the pyroelectrical signal by a parasitic capacity. a) Schematic description of the experiment: The top panel shows full illumination as used in clinical measurements, the bottom panel shows partial illumination narrowed by black tape. Left or right position of the metal plate is illustrated by colored frames. b) Measurements with full illumination. c) Slit measurements. Except for energy normalization the data was not manipulated.

For the setup used in this work the pyroelectric signal is not only depending on the temperature variations but, is affected by the electrical setup such as the preamplifier. Because the input impedance as well as the capacity of the preamplifier are constant, they may be disregarded in the analysis of the pyroelectric signal. On the other hand, the capacity of the OA detector itself, that is the area at which the ITO electrodes overlap, changes when a conducting object is brought into its close vicinity. Figure 5.5 illustrates

this effect with a simple setup in which a metal plate is placed underneath the detector at different positions. In Figure 5.5 a) two different illumination spots are sketched. At the top the full illumination is presented, as it was used in the clinical measurements. Below that the partial illumination is shown. Black tape is used to limit the width of the laser spot to the active area. The comparison to the slit measurements is needed to show that the variations are not produced by changes in the illuminated area but by changes in the capacity only. For each illumination mode four positions of the metal plate were investigated. The metal plate was either far removed (no sample) or partially underneath the electrodes (left and right) or covered the entire detector setup (full metal).

In Figure 5.5 b) and c) the measurement curves are presented, for full and partial illumination, respectively. Note that the colors are matched to visualize which setup corresponds to the measurement. The idea is to obtain an understanding of how the introduced capacity changes the pyroelectric signal. To mitigate the effects of optical reflections, the metal plate was covered by black tape. If the capacity change is not affecting the signal there would be no difference between the measurements, however, this is not the case. By introducing the metal plate, *no sample* to *full metal*, the amplitude increases drastically for both illumination types. In the case of the metal being positioned under the left electrode the effect of the introduced metal plate is comparably small which can be explained by the setup of the detector film. The electrode on the left side of the detector is underneath the film, thus the electrode is on the same side of the piezoelectric medium as the introduced capacitor plate. On the other hand, the right electrode is on top of the detector film and, thus, forms a capacitor with the metal plate and the piezoelectric film in between. This effect is visible for the two illumination configurations. In both cases the *metal left* curves resemble the *no sample* curves as well as the *metal right* curves resemble the *full metal* curves. Slight differences are visible in that the *no sample* and *metal left* measurements almost fully overlap in the partial illumination case while deviating from one another for full illumination, whereas the Metal Right and Full Metal measurements show a more precise overlap in the full illumination. These variations are most likely produced by small placement errors of both the black tape for the illumination slit and the metal plate.

One has to keep in mind that these measurements are conducted with the hand-held setup designed and used for clinical use, limiting the possibilities to this study. There are no facilities to mount the OA detector on an optical table and even if there were the presence

of the large metal object would influence the measurement. To avoid any parasitic capacities the measurements were performed on top of a plastic cupboard and the OA setup was held and positioned by a grounded experimentalist. The introduced metal plate was grounded as well. Without grounding of the metal plate, the measurements showed the same trends, however the noise levels dominated the signal and complicated the comparison.

Due to the similarity of the different illumination spots it can be assumed that only the illumination of the active area affects the pyroelectric signal to a relevant extent, which is consistent with the finding of the active area mapping in Section 4.2.2.1. The illumination of the individual electrodes, that is, removed from the active area, has no detrimental effect. Additionally, it is shown that only capacities introduced under the right electrode are relevant for the magnitude of the pyroelectric signal. This is easily understandable and controllable in the artificial setup. For in-vivo measurements it becomes more complicated, because the electrical properties of the patients cannot be standardized. The problem increases when the patient would move during the measurement.

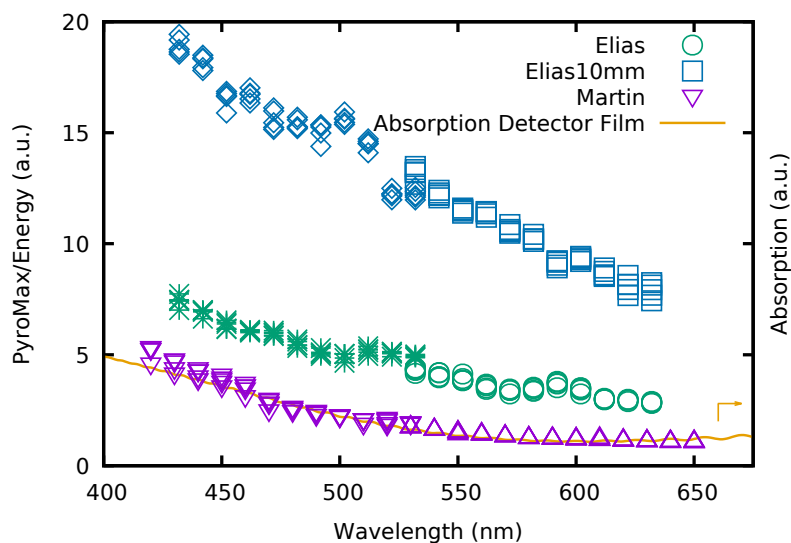


FIGURE 5.6: Wavelength dependence of the energy normalized maximum of the pyroelectric signal. Not only is the ratio of pyroelectric maximum to laser pulse energy influenced by the irradiation profile (compare Elias and Elias10mm) but highly dependent on the subject. The yellow line represents the absorption of the detector film determined via a spectrophotometer. Different measurement series are color coded. Measurements series were divided in two parts, indicated by use of different symbols.

As explained earlier, the effects on the capacity of the OA detector setup by a patient are quite complex so that the pyroelectric signal cannot be used to determine the laser

pulse energy reliably. However, to prove the principle feasibility to use the pyroelectric signal for energy calibration and validate our assumptions about its origin and details, the pyroelectric data for different wavelengths and persons was evaluated. In contrast to OA measurements the focus lies on the pyroelectric signal. Therefore, instead of subtracting the fit of the pyroelectric effect, its maximum amplitude was investigated. Thus, the data presented here can be regarded as metadata of OA measurements. It shows the correlation of the maximal amplitude of the pyroelectric signal with the energy of the incident laser pulse. The same method is used in commercial pyroelectric energy detectors.

Pyroelectric energy detectors exhibit a linear correlation between the energy of incident electromagnetic radiation and the produced voltage. Because the produced voltage is absorption dependent, and in turn wavelength dependent, the conversion factor needs to be determined for each wavelength individually. This relationship is reflected in the comparison of the energy normalized maximum values of the pyroelectric signal fit, to the absorption spectrum of the detector film determined by use of a spectrophotometer. As can be seen from Figure 5.6 the trend of the purple triangles, representing two measurements on the volunteer, corresponds well with the absorption spectrum of the detector film. Note that, out of logistical reasons¹, the high and low wavelengths were investigated separately, as indicated by the changing orientation of the triangles.

Even though it is not possible to exactly reproduce a measurement setup when working with living samples, the two sets of measurements overlap very well. From that we can deduce that the determining factors were reproduced. As described earlier, the detector setup for clinical use features a fronting-layer, determining the distance between detector and sample. The fiber end was positioned 18 mm above the sample. When this setup was used to measure on my forearm the wavelength dependence is shown to be similar, while the magnitude of the pyroelectric maxima was increased. This indicates the complex behavior of the pyroelectric effect, as hypothesized above. It is reasonable to conclude that the two human specimens available for the measurements have different parasitic capacities which in term influence the pyroelectric signal. Finally, to showcase the influence of the light intensity, the fiber facet was moved closer to the sample (see Elias10mm). Again, the trend is similar but as expected the magnitude

¹Most crucial: Safety goggles do not cover the whole spectrum.

increased significantly. The OA measurements in the high wavelength range of that series of measurements, i.e. the blue squares, are presented later.

5.3 Deconvolution With IRF - Ink On Glass

In this section, the validation of the post-processing is shown. More precisely, the deconvolution of the OA signal from a test sample is compared with simulation. The setup used in this experiment is the hand held setup used in the clinical studies (see Section 4.3.5). These results are also published in [Blu19].

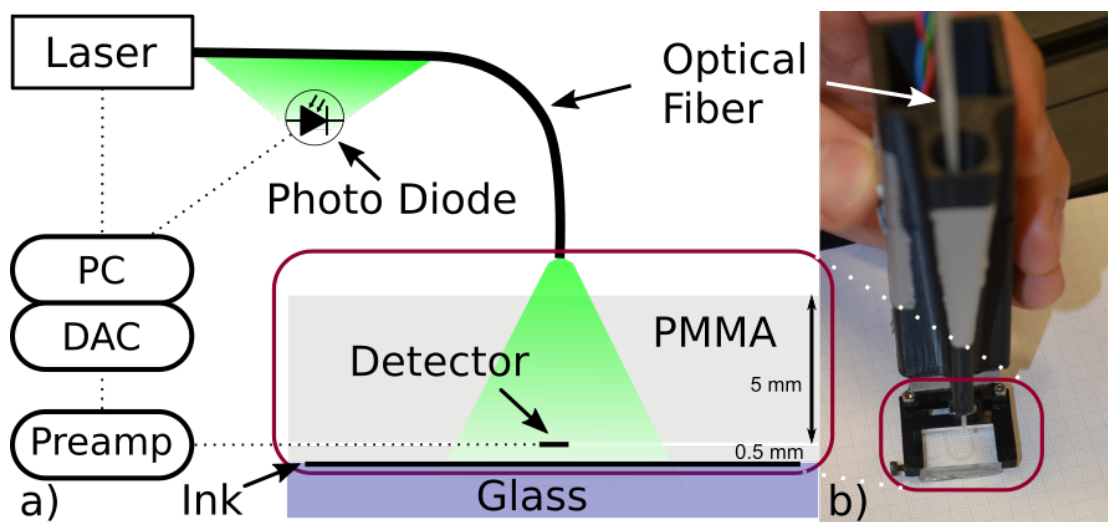


FIGURE 5.7: Handheld setup as used in the clinical studies. a) Sketch of experimental setup. For clarity the adhesive layers, surrounding the detector film, are omitted. b) Photograph of handheld sensor on grid paper. [Blu19]

Point spread functions (PSF) or more generally instrument response functions (IRF) represent the effect the measurement setup induces on the signal. The most straightforward way to obtain the IRF is to measure on a sample which produces a delta function as signal. In the case of our setup, a 1D delta function is needed, or in terms of the optoacoustic source, an infinitesimally thin absorbing layer. Thin layers can be created by coating a glass plate with coal or any other strong absorber. Unfortunately, it is difficult to obtain a thin layer of sufficiently high quality which can sustain both the distilled water as well as the mechanical strain during measurements. It is, however, much simpler to use a thick sample with such high absorption that the penetration depth and, thus, the contributing absorbing layer becomes vanishingly thin. Here, a 1.65 mm thick

piece of black plastic was used. Note that, it is important to use a sample which is thick enough that the acoustic reflections occur outside of the relevant measurement time window. Also, the sample should be acoustically homogeneous to prevent reflections inside the sample.

In general, the resulting pressure wave is not a delta function in its purest form. Nonetheless, it can be assumed as such if the signal duration is shorter than the theoretical limit of the resolution. From the physical point of view, the axial resolution is limited by the thickness of the detector. If the spatial extent of the transient signal is smaller than the detector film thickness, it cannot be resolved. For the detector presented here, the thickness is close to $10\ \mu\text{m}$ corresponding to an absorption coefficient of $100\ \frac{1}{\text{mm}}$ for the smallest resolvable signal length, assuming similar sound velocities of detector and absorber, which is a reasonable value for black plastic (The precise absorption coefficient is too high to be measured). During the data processing of the pure OA signal, frequencies above the acoustic frequency of 20 MHz are suppressed, thus, the achievable resolution is reduced further. This is necessary to prevent amplified noise and transformation artifacts from rendering the signal unusable. With the 20 MHz cutoff frequency and the speed of sound in the plastic, the minimum absorption coefficient, required for a reasonable delta peak sample, can be roughly approximated as follows: 20 MHz signal frequency corresponds to 50 ns signal duration. During that time, the pressure transient travels 0.11 mm at a sound velocity of 2150 m/s (black plastic). In other words, signals created in a depth of less than $100\ \mu\text{m}$ apart cannot be resolved. This means that due to the 20 MHz cutoff the minimal absorption coefficient needed is reduced to $10\ \frac{1}{\text{mm}}$ which is far below the absorption coefficient of the black plastic. Thus, it is justified to use the measurement on the black plastic to deduce the instrument response function.

To showcase that the resulting IRF can be used to reproduce the original pressure signal by deconvolution, we created a simple test sample. In order to display the capabilities of this method the features of the pressure profile have to be thin. Using a permanent board marker, we applied black ink on a 4 mm thick plate of borosilicate glass. Although the thickness of the ink layer cannot be determined by any means available to us, it could be seen by comparison with electrical tape that it is distinctly thinner than $100\ \mu\text{m}$. To ensure acoustic coupling, a drop of distilled water was applied between the fronting layer of the detector setup and the ink. As explained earlier, after measurement of the raw OA signal, the pyroelectric signal contribution was removed from the signal, both for the IRF

measurement as well as from the signal of the ink-on-glass sample. Regarding the IRF, only the main OA signal is relevant, thus the measurement is zero-padded to remove the reflections (see Figure 5.8a). To prevent sharp edges that would yield artifacts in the deconvolution, a time domain Butterworth filter is used.

In Figure 5.8a, it can be seen that the overall form of the IRF and the signal of the ink are very similar in shape, which is to be expected because both result from measurements on black layers. The main difference lies in the change of acoustic impedance from ink to glass which is absent in the black piece of plastic used for the IRF. By means of a fast Fourier transformation (FFT), both signals are converted to the frequency domain for the deconvolution. Most of the frequency spectrum has to be suppressed in order to prevent noise and parasitic signals to dominate the back-transformed signal. As shown in Figure 5.8b, a second Butterworth filter is used in the frequency domain to suppress any contributions to the signal with frequencies above 20 MHz. If the cut-off frequency were chosen only a few MHz higher, the resulting signal would be dominated by noise. Subsequently the FFT of the ink signal is divided by the FFT of the IRF and back-transformed to obtain the processed pressure profile.

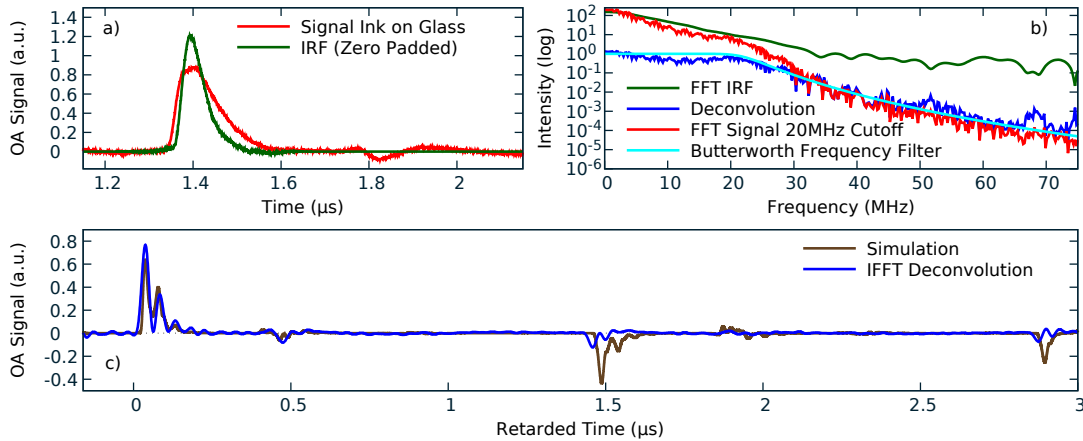


FIGURE 5.8: Visualization of post-processing. (a) OA signal of the instrument response functions (IRF) and ink-on-glass sample after removal of the pyroelectric signal (green and red). IRF was zero padded to prevent transformation artifacts. (b) Frequency spectra of IRF (green) and the ink-on glass-signal with 20 MHz cut-off (red), the Butterworth filter for the 20 MHz cut-off as applied on the signal (turquoise), and the resulting signal after deconvolution (blue). (c) Back transformed signal (blue) and 1D simulation (brown) agree well. All features of the signal can be identified. [Blu19]

To visualize the validity of this approach, the deconvolved signal is compared with a 1D finite-difference simulation of the ink-on-glass setup. The program code and its

description are made available on GitHub². Because acoustic diffraction is a product of propagation in multiple spatial dimensions, it is not present in 1D simulations. The setup is designed to work in the near field, so diffraction is negligible. Diffraction only plays a significant role at long runtimes of the signal. It probably contributes to the differing appearances of signal features at times $> 1.4 \mu\text{s}$ in comparison to the simulation.

In Figure 5.8c the simulated signal is plotted besides the deconvolved measurement of the ink-on-glass sample. For good comparability, the first peak in both curves were shifted to zero in time. Instead of the single broad peak of the unprocessed signal, the deconvolved data curve features a sequence of sharp peaks. The sequence of peaks, starting at $0 \mu\text{s}$, represents the OA signal of the black ink which is subsequently followed by a series of reflections from the inner boundaries of the ink. Shortly before $0.5 \mu\text{s}$, the reflection from the detector film back through the fronting layer to the sample and back to the detector again is visible. Approximately $1 \mu\text{s}$ later, the reflection of the glass–air boundary reaches the detector, again followed by the reflections inside the fronting layer. Finally, in the plot, the second reflection from the glass–air boundary, which is created by the part of the first reflection that is reflected off the glass–ink boundary is visible. The reflection of the backing layer to air surface arrives at $3.61 \mu\text{s}$ and, thus, is not included in the plot.

The simulation is added to the graph to visualize that every feature in the measurement is accounted for in the model of the sample. For simplicity, the density of all layers was set to $1 \text{ kg}/\text{dm}^3$. Due to the generic nature of the sample, we refrained from implementing a multivariable optimization to find the acoustic parameters which perfectly recreate the measurement. The actual speed of sound and thickness of the black layer of ink are not very essential. However, the same deconvolution process can be applied to any measurement data recorded by this detector setup. In the subsequent sections measurements on human skin, using the same detector, are presented. Because the exact morphology of the living tissue specimen is unknown, it was necessary to validate the deconvolution process beforehand.

In Table 5.1 the sound velocities and thicknesses of the different layers are listed. The speed of sound for any polymer strongly varies depending on its specific production and has to be determined for each individual piece.

²Omelchert/LEPM-1DFD. Available online: <https://github.com/omelchert/LEPM-1DFD> (accessed on 8 May 2019)

Layer	Material	Soundvelocity [m/s]	Thickness [mm]
1	PMMA	2777	5
2	Adhesive	2000 ^a	0.02 ^a
3	PVDF	2250 ^b	0.01
4	Adhesive	2000 ^a	0.02 ^a
5	PMMA	2777	0.5
6	Ink	1500 ^a	0.04 ^a
7	Glass	5640	4

TABLE 5.1: Material layers as used in the measurements and simulation. Most values were determined through caliper and acoustic runtime measurements. The data sheet of the adhesive does not include the sound velocity which thus had to be estimated like the thickness of the adhesive and ink layers. Estimated values are labelled with “a”. The sound velocity of the PVDF film (labeled with b) was taken from the data sheet.

5.4 OA Measurements on Human Skin

This section is about the measurements performed on human skin. Contrary to Section 5.2 where at the end the changes of the pyroelectric effect were presented for different human subjects, this section only considers the OA signal. First, wavelength scans using the OPO as laser source are shown. In Section 5.4.2 the clinical measurements are presented. Even though three detector setups were tested in the clinical trials only measurements with one detector produced evaluable results. At the beginning of Section 5.4.2 an overview is given of the lesions measured with the detector setup, those discussed in detail are highlighted with a grey background. Due to grounding problems, not every lesion examined resulted in useful measurements. The patient head, for example, is difficult to ground. Additionally, a lesion was not measured on if ethical argument spoke against it, e.g. the skin was open. Other lesions could not be measured on because of large irregularities of the skin surface. To get reliable signals the surface needs to be somewhat plane when the detector setup is pressed on it. All measurements of the clinical detector are presented in the Appendix A

5.4.1 OA Wavelength Scans

As described earlier, one of the main advantages of using an OPO is the large wavelength range which can be used. This enables us to conduct OA measurements with different wavelengths and from these spectral responses the composition of known absorbers can be inferred, or absorption spectra of unknown absorbers can be created. In

general, the wavelength choice is only limited by the absorption of in the sample. When the absorption is high the penetration depths becomes small, on the other hand, small absorption reduces the signal-to-noise ratio as well as the contrast between layers. For the specific setup used in this thesis the transmission through the detector film imposes another restriction on the usable range of wavelengths. As shown in Section 4.2 the transmission drops significantly below 400 nm. However, regarding skin measurements such short wavelengths yield very small penetration depths and, thus, are useless for OA depth profiling. With the OPO available to us, the wavelength range from 432 nm to 652 nm was scanned in 10 nm increments. At each wavelength 5 measurements were performed (a different evaluation of these measurements was shown in Section 5.2). Due to safety concerns the whole spectrum could not be obtained in a single turn but had to be sequenced. A safety goggle covering the whole visible wavelength range would be highly impractical.

As described in Section 4.4 the OPO introduces much noise which must be removed in post-processing which in turn needs reference measurements that increase the likelihood of errors. Keep in mind that due to the influence of the parasitic capacity the person who is examined has to keep still throughout the whole measurement sequence, including the reference measurements. Therefore, these measurements were only performed on volunteers under laboratory conditions. Nevertheless, the OA signals in most measurements were not prominent enough to allow a thorough evaluation. In Figure 5.9 the best data set is presented. The colors represent the corresponding wavelengths. In this case the measurements were performed on a mole on my own forearm from 532 nm (green) to 632 nm (red) in 10 nm increments and 5 measurements for each wavelength step.

The left plot shows the raw data and the fitting curve used to remove the pyroelectric signal in the same color as the corresponding data set. Note that, the parasitic noise from the laser source dominates the signal significantly. The curve is shifted in time, so the OA signal starts at 0 μ s. After the removal of the pyroelectric signal and the subtraction of the background measurement (see Section 4.4) the signal-to-noise ratio improved, as can be seen in the middle plot. Here, the noise level is below the signal level. By comparing the curves in the region around -0.2μ s, it becomes clear that the parasitic signal varies for each individual measurement and, thus, cannot be completely removed

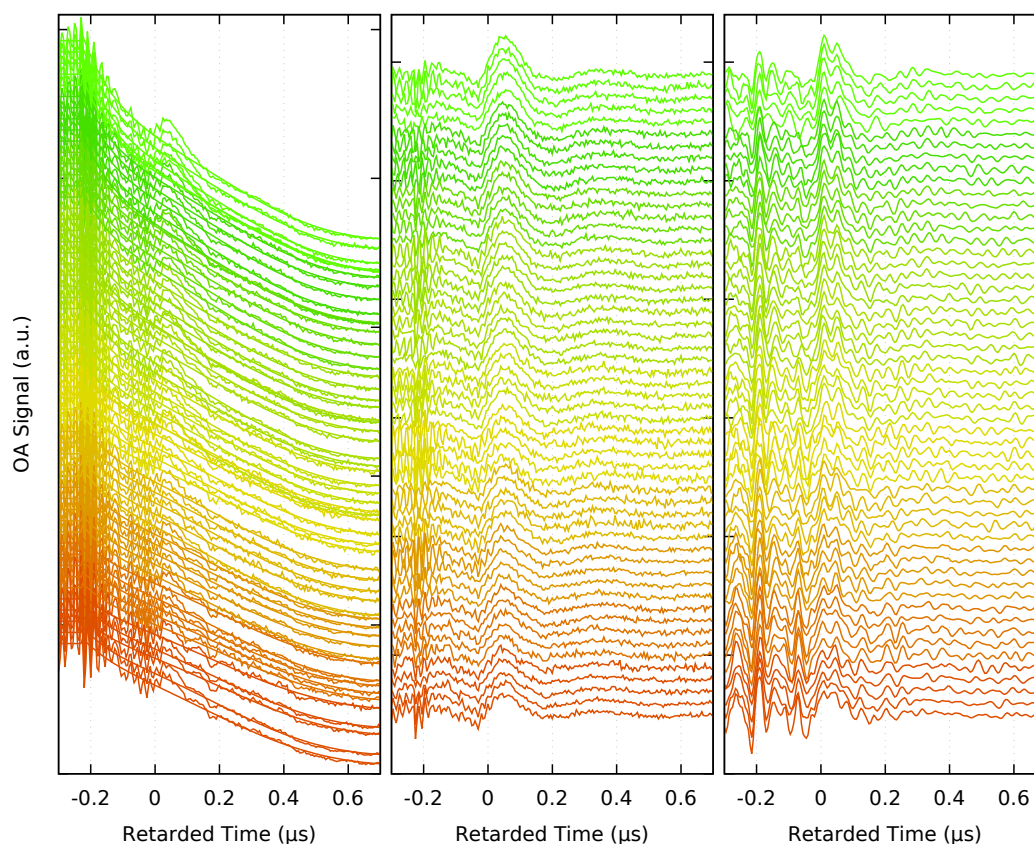


FIGURE 5.9: OA measurements of a mole on the lower arm. Colors represent the wavelength used from 532 nm (top, green) to 632 nm (bottom, red) in 10 nm increments and 5 measurements for each wavelength. To improve visibility and file manageability only every 10th point is plotted. Otherwise the curves would appear thicker with high frequency noise. The left plot shows the raw data in addition to the fit curve of the pyroelectric signal. In the middle, the OA signals after removal of the pyroelectric signal and background are presented. Please note that the remaining parasitic signal at $-0.2\ \mu\text{s}$ differs between curves. The plot on the right depicts the signal after deconvolution with the instrument response function. After the data processing the signal to noise ratio decreased, impeding in depth analysis of the OA curves. A decrease of OA amplitude is visible with increasing wavelength.

by background subtraction. Between $-0.2\ \mu\text{s}$ and $0\ \mu\text{s}$ the curves show a slight downward trend which indicates an imperfect removal of the pyroelectric signal, likely caused by the noise. The OA signal is clearly visible from $0\ \mu\text{s}$ to $0.2\ \mu\text{s}$ for all wavelengths. As expected, the amplitude decreases with increasing wavelength.

On the right-hand side of Figure 5.9 the signals are depicted after the deconvolution with the instrument response function. Again, this process produces a strong elevation of the parasitic pickup, which distorts the signal. Due to the high noise level, a quantitative evaluation is not feasible. However, like in the middle column the amplitude of the OA signal changes inversely proportional with the wavelength. In addition, the falling edge,

starting just after 0 μ s, changes its form. While at 532 nm the OA signal drops quickly the slope in case of 632 nm is comparably flat. These findings are in accordance with the expected evolution of the absorption coefficient of melanin, that is decreasing with increasing wavelength. As discussed in Section 2.2 with a better signal-to-noise ratio the absorption coefficient could be deduced from this slope.

Further improvement is needed to obtain quantitatively usable information. That way it would be possible to directly measure the absorption spectra of melanin or the human skin in general. Probably this is not feasible with the OPO available to us due to the very high noise pollution it produces. For the presented measurements the fiber had to be moved closer to the skin, increasing the radiation exposure as well as compromising the near field conditions. Higher pulse energies would improve the signal to noise ratio but would soon exceed the MPE levels. Additionally, due to the poor beam profile of the OPO, higher energies often burn the fiber facet during the coupling process. Realistically, a different OPO with significantly less electromagnetic pollution is needed.

5.4.2 Clinical Measurements

The clinical measurements took place in the frame work of the MeDiOO project (for description of procedure see Section 2.4). In coordination with the dermatological clinics of the university clinics of Rostock and Goettingen we conducted measurements on suspicious lesions on human skin. The data was processed as described in Section 4.4 for the clinical detector setup and the Ultra 50 laser source. In this section the results of the OA part of the measurements are presented. In contrast to OCT and especially Raman measurements the OA measurements at their current state are not related to the nature of the melanocytic nevus. Thus, it is of no interest whether the investigated nevi are benign or malignant.

The section is structured by lesions in a non-chronological manner. To ensure anonymity all the lesions are named without connection to the patients. The system we chose to encode the samples is sorted by week, day of the week, patient number on that day and lesion on that patient. With that, the second lesion on the third patient on Thursday of the first measurement week would be labeled W1-4-3-2.

For every lesion, first the OA signal is presented and discussed followed by a photograph of that lesion taken by a dermatoscope which is a camera specifically designed to take closeups of skin marks. Additionally, the histopathological slice is presented as used for the regular medical assessment. For completeness, the orientation of the surgical cuts as indicated by the surgeon are presented. The medical staff later used this drawn symbol to determine the orientation of the histopathological cuts. Please note that it is not part of the standard medical procedure to determine the precise location of the histopathological cut, the main interest there is to find the thickest part of the lesion which is indicative of the stage of the cancer in case a lesion turns out to be melanoma. We must be very careful when correlating the histology and specific features in the OA signal. In addition to the uncertainty in the precise location, the different approach of histopathology in comparison with OAs has to be kept in mind. The histology is not designed to determine the absolute concentration of melanin. While relative concentration changes are visible in the histology, the staining process is too complex to infer statements of melanin concentration in any quantitative way.

To showcase possible absorption profiles that could produce these OA signals, simple models are added. Please note that this is not the same as measuring the thickness of

the nevi. These measurements and their analysis are meant to present the potential of the OA setup developed in this thesis. For definitive thickness determination further improvements of the hardware and post-processing would be needed.

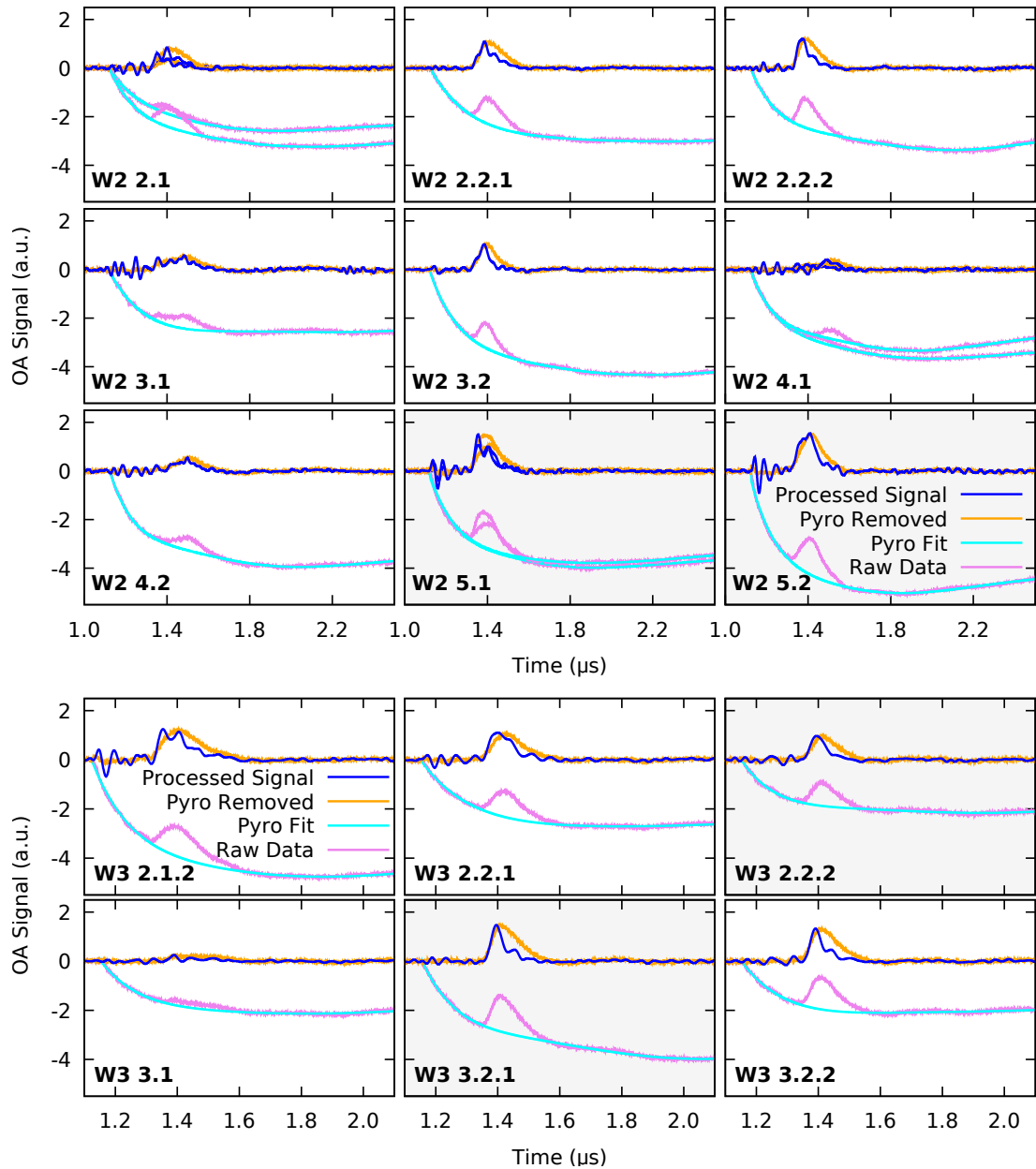


FIGURE 5.10: Overview of OA measurements with clinical detector setup from week 2 (upper panel) and 3 (lower panel): Individual plots are named after the nevus. Violet: Raw data. Light blue: 10th order polynomial fit to remove the pyroelectrical signal. Orange: Signal after removal of the fitted pyroelectric signal. Dark blue: Processed data after deconvolution of the instrument response function. Note: W2 2.1, W2 4.1 and W2 5.1 consist of two measurements each. Multiple measurements were acquired due to visibly different areas on the nevi. Measurements with a light gray background are discussed in detail in the results section. All measurements as well as the corresponding histology and photograph of that lesion can be found in the Appendix A.

OA Measurements of Lesion W3-3-2-1

Lesion W3-3-2-1 was located on the upper leg, which facilitates easy electrical grounding. However, despite proper grounding and other precautions unwanted changes occur, due to the complexity of in-vivo measurements. In Figure 5.11 the parasitic pickup is clearly distinguishable in the time between $-0.2-0\ \mu\text{s}$ when the laser pulse was triggered but no OA signal has reached the detector yet. This pickup likely stems from the flashing of the pump lamps inside the laser system. In this case it has approximately twice the amplitude of the remaining noise at other times. However, this is only due to the good grounding conditions. As will be presented in the subsequent sections, this ratio increases when a proper grounding is impeded. Even though the pickup here is relatively low, it complicates the analysis of the OA signal.

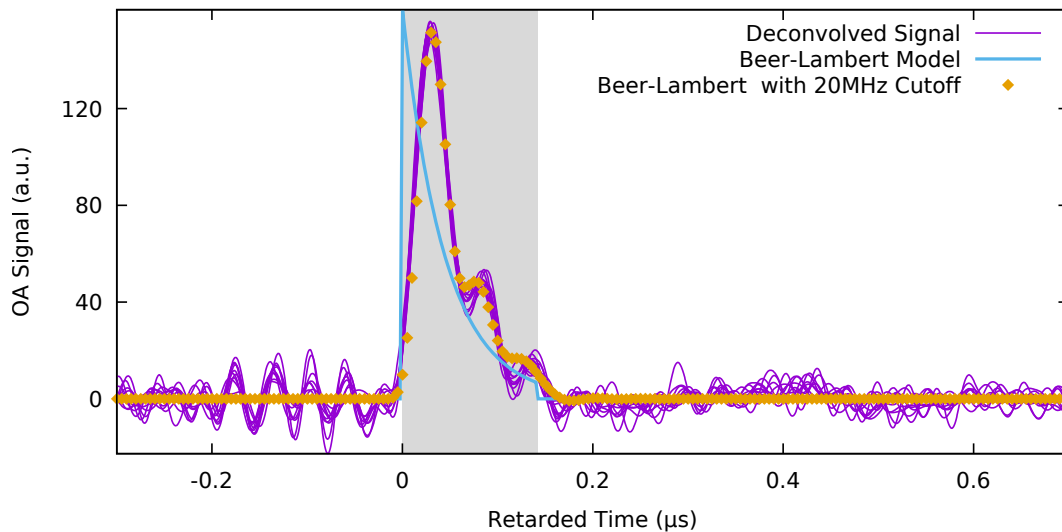


FIGURE 5.11: Post-processed signal form W3-3-2-1 lesion of the third week (purple). Beer-Lambert model of the absorption profile (blue). Yellow dots represent the model curve after a bandwidth cutoff at 20 MHz. Changes due to the Gibbs phenomenon neatly recreate the OA measurements. The ray column in the background corresponds to the histopathological thickness.

The blue curve depicts a Beer-Lambert curve representing the absorption profile in homogeneous media. As thickness of the simulated layer the value from the histology was used ($213\ \mu\text{m}$). Assuming a sound velocity of $1645\ \text{m/s}$ the transit time for that layer yields the gray column in the background of the graph. To match the effects of the Gibbs phenomenon on the measurement data (see Section 3.4) which is caused by the 20 MHz cutoff in post-processing, the simplified pressure distribution profile was subjected to the same frequency cutoff. By reducing the bandwidth of the Beer-Lambert curve to 20 MHz

the yellow dotted path results. Assuming perfect near field conditions and the absorbing layer as homogeneous, this would reproduce the measurements. Obviously, the biological tissue cannot be assumed to be perfectly homogeneous which makes the overlap of the processed curves quite remarkable. Both the purple lines and the yellow dots form a tall peak in the beginning, which falls off and is overlaid by oscillations. After $0.2 \mu\text{s}$ the OA signal has decayed to zero and in case of the measurements only the parasitic noise remains. Due to the homogeneous modeling of the simulated curve a single absorption coefficient can be determined. The simulation as presented in Figure 5.11 yields an absorption coefficient of $15 \frac{1}{\text{mm}}$. In Section 2.2 the absorption coefficient of black skin was calculated to be $16.91/\text{mm}$.

These measurements are very promising with regards to the overall agreement with the model. This indicated, that the assumptions made for the model are valid enough to predict the OA signal for this lesion, that is, when the penetration depth is known. However, concerning the thickness determination without knowledge of the morphology, an overall agreement of the two curves does not suffice. For example, by doubling the assumed thickness in the model, the main peak and the general progress of the measurements are recreated equally well (not shown). This can be explained by the small size of the kink at the end of the absorber, which is the main difference between the models using different thicknesses. An algorithm to optimize for the thickness in the model to match the experiment data should therefore weigh this region more strongly. Unfortunately, other variables would need to be taken into account, such as the absorption coefficient, further complicating the analysis. Adding onto the challenge, the pickup signal overlaying at least the beginning of the OA signal, is highly depending on many factors during the measurement which are hard to control, especially in-vivo, and cannot be removed to a satisfying degree in post-processing. Therefore, a multi-variant optimization to determine the thickness, is sensible only after these other challenges are addressed. Nonetheless, these measurements showcase the potential of the measurement setup and post-processing.

The regarded lesion was located on the thigh which simplifies proper grounding. It is relatively easy to wrap the wire around extremities and especially the upper leg through its high deformability keeps a large contact area to the grounding wire. As Figure 5.12

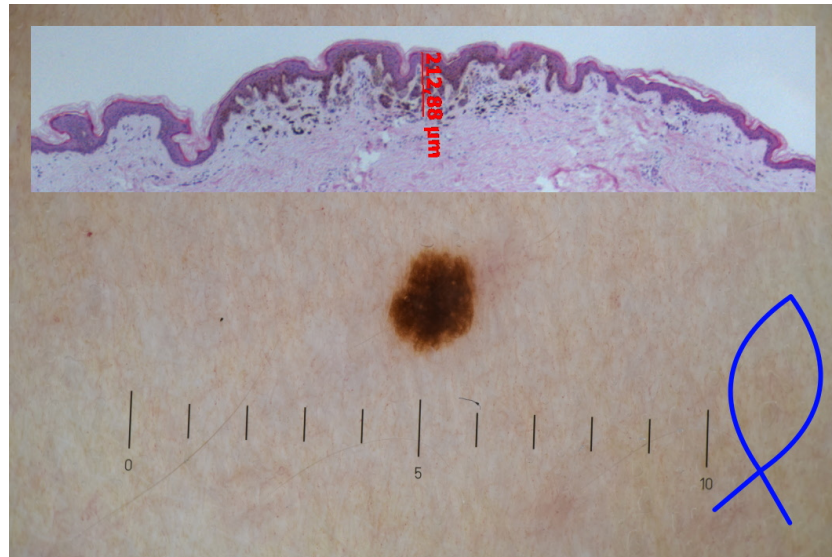


FIGURE 5.12: Histology and photograph of lesion W3-3-2-1. The blue symbol at the bottom right corner represents the drawing of the surgeon indicating the orientation of the cuts and thus the orientation of the histology. In this case the histopathological cut is slightly off the horizontal. The thickness was determined to be 213 μm . Scale in the bottom is in millimeters.

shows, in a visual examination the lesion appears to be quite homogeneous with high contrast in comparison to the regular skin. The precise position of the histopathological cut is not known because it is not of interest for the regular medical procedure. From communication with the medical staff we know that the investigated layer is positioned in the center, because the thickest part is assumed to be in that region. With surface dimensions of approximately $1.5 \times 2 \text{ mm}^2$ for this lesion, the detector covers a big part of it. Thus, it is very likely that the measured region overlaps with the histopathological slice. In the upper part of Figure 5.12 the histology shows a homogeneous penetration into the papillary dermis. Here homogeneous is meant as opposite to an individual region of increased melanin content protruding into the surrounding tissue. In that regard the sample is ideal for our device because narrow absorber structures in the skin would, by default, yield far field signals which need a different approach in the signal analysis.

Lesion W3-3-2-2 is very similar, to the lesion discussed here regarding appearance, thickness, and location on the body. Both were located on the same person. To avoid repetition an in-depth discussion of W3-3-2-2 is omitted. In Appendix A, OA measurements, histology and photographs of each lesion can be found on consecutive pages allowing for an easy comparison.

OA Measurements of Lesion W2-5-2

In contrast to lesion W3-3-2-1 the measurements of lesion W2-5-2 (see Figure 5.13) cannot be explained by a homogeneous absorption. Because of the complexity of biological samples, an optimized fit of the simulated curve to the post-processed measurements would be of little validity. For the fit to yield proper results the simulation would need to include the three-dimensionality of the measurement setup as well as the sample. At the current state this would very likely produce ambiguous results at best³.

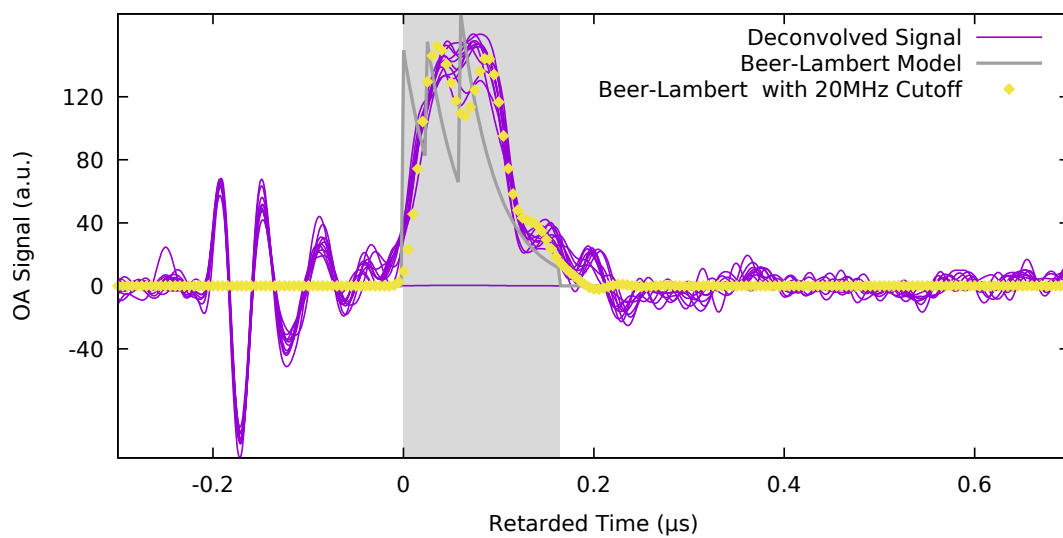


FIGURE 5.13: Post-processed signal of lesion W2-5-2 (purple). In the region $-0.2-0\ \mu\text{s}$ large parasitic oscillations are visible. Estimated Beer-Lambert model assuming inhomogeneous absorption of the lesion is depicted in grey. Yellow dots represent the model curve after a bandwidth cutoff at 20 MHz. Even though the presented model is unlikely to reflect the real conditions it shows that the result can be explained by realistic skin properties without the assumption of erroneous measurements. The gray column in the background represents the thickness of the lesion as determined by histopathology.

Instead of the simple Beer-Lambert model of homogeneous absorption, the model here was extended to allow for the superposition of several absorption coefficients at different depths. This way the varying absorption properties in three dimension are expressed in the one dimensional absorption profile. The reduction of the dimensionality produces unrealistic behavior when regarded as a truly one-dimensional sample. For instance, in the used model the pressure profile exhibits three peaks that increase in altitude. In the 1D picture this represents a strong increase in absorption by a factor of two for the second peak and again a factor of three for the third peak. For the concerned lesion

³This is a matter of current research in our group.

this would mean that the absorption coefficient is almost at 100 mm^{-1} in the third layer which is a factor of six higher than can be expect in African skin. When considering the three-dimensionality of the sample, the emergence of multiple peaks superposing each other can be explained by lateral differences in absorption, which are combined into a single signal by the OA detector.

Another puzzle piece for investigating the specific form of the signal is the topology of the skin surface. This lesion was located on the abdomen of an older person; thus, the skin was not very firm. By applying pressure with the OA head, the surface is flattened to a certain extent but small wrinkles are still possible. Any wrinkle filled with water would lead to a delayed beginning of that part of the OA signal relative to the signal of neighboring locations. This could also explain the slower rise of the first slope beginning at $t=0\text{ }\mu\text{s}$. The model presented here is not conceived to determine the actual absorption properties of the lesion, but to show that it is possible to explain the results without assuming erroneous measurements. In any case, the simulation would need to include a lot more parameters than the one-dimensional absorption profile, to describe the resulting curves in detail.

As mentioned earlier, the field of view of the detector can be imagined as a cone whose opening angle is determined by the detectors directionality and every moment of the OA measurement represents an integration over a conic section area. Thus, comparison of OA curves to the histopathological cuts (histology) have to be made carefully, for histology displays only one lateral dimension. In Figure 5.14 at the top the histology of lesion W2-5-2 is depicted. Even if the field of view of the OA measurement overlaped with this 2D cross-section, features extending orthogonal to the histology plane could not be seen. At the edges of the histology, regions are visible with lower levels of pigmentation. Such features might also explain the occurrence of peaks in the signal beneath the surface of the specimen. In the dermatoscopic photograph at the bottom of Figure 5.14 a net of brighter spots is visible, which match the pattern of the papillae.

Unfortunately, the standard procedure necessitated by medical protocol, does not include an exact localization of the depicted histology slice, thus, we merely know its orientation relative to the nevus and that the slice is cut from the central region of the lesion. Nonetheless, histology can give broad information on the structure of the pigmented skin region, because it can be assumed that the general morphology is similar throughout the

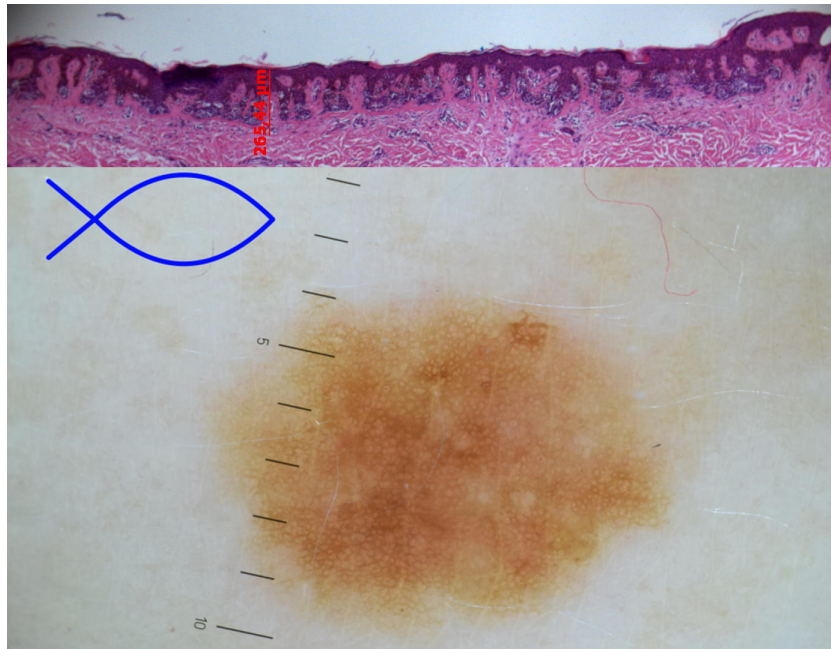


FIGURE 5.14: Photograph and histology of lesion W2-5-2. The histology at the top shows a penetration depth of $265.44\ \mu\text{m}$ as determined by the medical staff. The blue symbol at the top left of the photo represents the drawing of the surgeon indicating the orientation of the cuts and, thus, the orientation of the histology. In this case the histopathological cut is vertical in the picture. In comparison to W3-3-2-1 the lesion appears much lighter in the photograph with the dermal papillae showing as circular irregularities. At the edges of the histology inclusions of less colored regions are visible. The scale is measuring in mm.

lesion. Please note that this assumption is only appropriate for this benign skin mark and is unlikely to hold true in aggressive types melanoma where erratic growth might produce a variety of morphologies.

At the bottom of the lesion the transition into less pigmented tissue is not abrupt, especially when considering the extended area over which the measurements average the signal. These smooth fringes need to be considered to explain the signal presented earlier. Even though the model follows the measurements well, especially at the large slopes of the curves, the last part of the OA signal ($0.15\text{-}0.2\ \mu\text{s}$) appears to be underestimated by the simulation. This can be explained by the branching nature of the lesions lower boundary, as well as the non-zero absorption of the regular tissue beneath, which is not represented in the model.

Another adverse factor for creating an optimized model is the significant parasitic signal. In the region between $-0.2\text{-}0\ \mu\text{s}$ in Figure 5.13 large oscillations are visible, comparable in size to the OA signal. Although the oscillations seem to decay greatly before the OA signal arrives, they may still affect the measurement. For lesions located on the torso, in

this case on the belly, the method of grounding by wrapping a wire around the patient is impeded due to the large volume acting as an antenna for the noise. To manage these oscillations and make them negligible compared to the OA signal a fully encompassing cage would be needed including large area contact pads to ensure good conduction to the patient. However, for this prototype we had to rely on a belt of aluminum foil to assist the grounding wire.

OA Measurements of Lesion W3-2-2-2

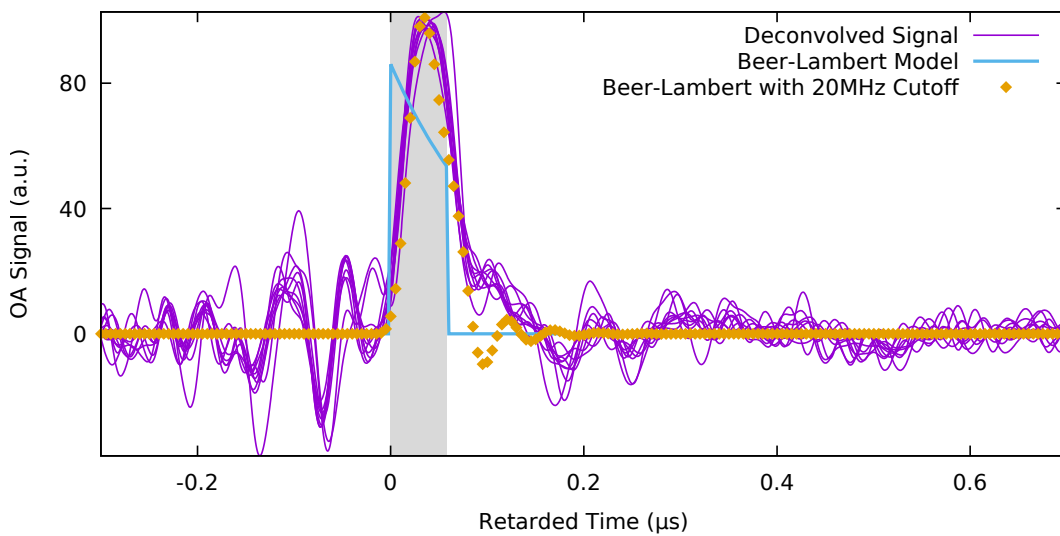


FIGURE 5.15: Post-processed signal of lesion W3-2-2-2 (purple). In the region from -0.2 to 0 μs large parasitic oscillations are visible. Estimated Beer-Lambert model assuming homogeneous absorption of the lesion is depicted in light blue. Yellow dots represent the model curve after a bandwidth cutoff at 20 MHz. The gray column represents the thickness of the lesion as determined by histopathology. The investigated lesion is very thin which leads to a single peak in the OA signal.

In the previous section the potential complexity of measurements on an inhomogeneous nevus is discussed. Due to the reduction from a 3-dimensional sample into a 1-dimensional measurement, not all the information can be retained. The main challenge would lie in the interpretation of the ambiguous results for the underlying melanin contribution. This problem is intrinsically coupled to the limited experimental resolution. With increasing resolution, the results would become more unambiguous. Here, a lesion is presented which is very thin, so that a single homogeneous absorption layer suffices to recreate the measurement in the model. This measurement is suitable to investigate the smallest resolvable depths of the OA measurement and the used post-processing.

The histopathology produced a thickness of only 95.65 μm which is close to the thinnest feature that can be sampled with the 20 MHz cutoff⁴.

In Figure 5.13, the main part of signal is a single, almost symmetric, peak. The strong oscillations caused by the parasitic pickup complicate the distinction between signal and noise. Thus, it is not possible to assert with certainty whether the bump succeeding the main peak is part of the signal. The value used for the absorption coefficient used for the simulation is 5 mm^{-1} which is more than a factor 3 smaller than expected for melanocytic nevi. In combination with the small depth of the absorber this yields a large drop at the end of the absorption profile, which in turn produces ringing in the bandwidth limited model signal. It is unrealistic that the absorption coefficient of the pigmented skin is that low, thus, other explanations must be considered. In theory the effect of the absorption coefficient is twofold, it determines the amplitude and the decay rate of the OA signal. Due to the method of deconvolution used here, the scaling factor is chosen to suite the height of the processed measurements. There are too many unknown in the procedure of the clinical measurements to quantitatively correlate this scaling factor to the absorption coefficient⁵. However, as can be seen in the Section 5.4.2, the progression of the signal decay can be correlated with the absorption coefficient, at least for the simplified model of a single homogeneous absorbing layer without backscattering. The low total absorption in the layer of the nevus investigated here, caused by its shallow penetration depth, allows for most of the light to pass through to the regular skin below. In these skin layers, back-scattering might play a bigger role. For this thin nevus, the resulting measurement curve does not allow to investigate the nature of its decay. In other word, it is not possible to deduce whether the original pressure profile follows the Beer-Lambert law.

The presented curve using the absorption coefficient of 5 mm^{-1} mainly distinguishes itself from data based on a more realistic value of 16 mm^{-1} by the ratio between the rising and the falling edge. So instead of using a lower underlying absorption coefficient, the model can be extended to allow light to reach the absorber through other paths, such as backscattering, to explain the convergence of the two edges . Even more complex light paths could be considered. The irradiation beam diameter exceeds the nevus distinctly,

⁴At least in skin.

⁵Hence, the use of arbitrary units.

allowing the possibility of the light travelling around the nevus through scattering (Presented for Melanoma in nude mice by [Zho14]). While these light delivery mechanisms qualitatively explain, how the pressure at the bottom of the nevus could be raised in relation to the pressure at the skin surface, they are highly unlikely to account for the amount of energy needed. For simplicity, we assume a model where the additional illumination from below yields an inverse Beer-Lambert profile superposing the absorption profile from above. In case of an absorption coefficient of 16 mm^{-1} it would require approximately half the intensity of the incoming beam. Due to lacking information on the specific morphology of the nevus, any further extension of the absorption model would be highly speculative. A depiction of the resulting curve of the superposed Beer-Lambert profiles can be found in the Appendix B.1.

In Figure 5.16 the lesion can be seen. In comparison to lesion W3-3-2-1 it appears saliently lighter. However, one has to be careful in attributing the appearance of the lesion with its melanin concentration and, thus, its absorption coefficient. Even moles with very high absorption may appear brighter when they are thin. To investigate thinner layers, the bandwidth problem would need to be addressed first. However, to assert the hazard of nevi with such small penetration depths is of no concern, because they are still contained in the epidermis, thus, unlikely to metastasize.

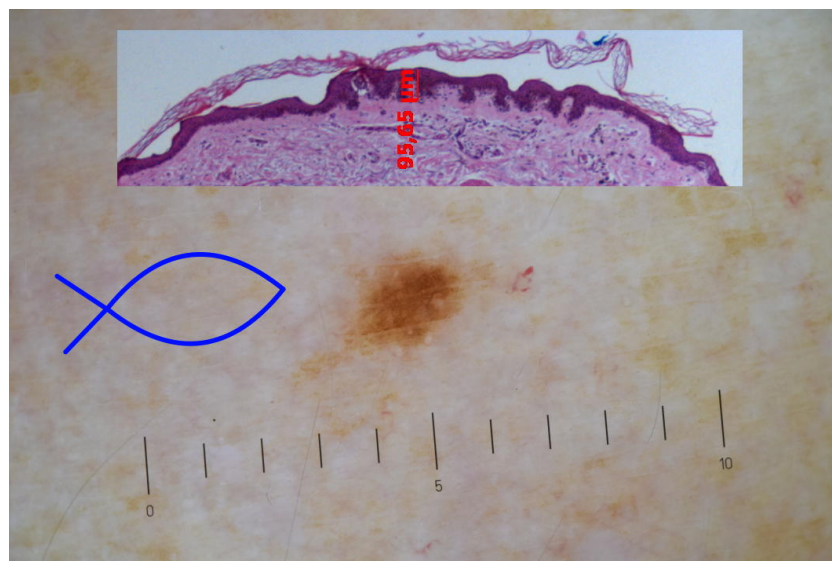


FIGURE 5.16: Photograph and histology of lesion W3-2-2-2. The histology at the top shows a penetration depth of $95.65 \mu\text{m}$ as determined by the medical staff. The blue symbol on the left represents the drawing by the surgeon indicating the orientation of the cuts and thus the orientation of the histology. In this case the histopathological cut is slightly off the vertical direction in the picture. The scale at the bottom is in mm.

OA measurement on lesion W2-5-1

As discussed earlier, the penetration depth of the irradiation is limited by the absorption coefficient. For human skin with a high concentration of melanin the absorption coefficient is about 17 mm^{-1} for a wavelength of 532 nm (see Section 2.2). Due to the exponential decay of the signal, again assuming a homogeneous distribution of absorbers, the depth in which the end of the pigmentation can be determined depends on the noise level. In theory, the kink representing a decrease in absorption, thus, the end of the pigmented region, can be determined at any depth. However, even if we assume the noise to be negligible small, inhomogeneities in the sample would impede the exact localization of the lower boundary. For a realistic measurement we can approximate that any signal with a 10th of the maximal intensity of the OA peak is not distinguishable from noise or small inhomogeneities. For an assumed absorption coefficient of 17 mm^{-1} this would correspond to a penetration depth of $135 \mu\text{m}$. Obviously, lesions can become much thicker than that. For dermatological investigation of malignant melanomas, the thickness range around 1 mm is the most interesting. Therefore, the limited penetration depth of the laser radiation poses a problem. In Figure 5.17 this case is depicted. A suspicious lesion with a thickness of $897 \mu\text{m}$ was investigated. Correspondingly the gray column in the plot was set to represent the run time of acoustic waves over that length.

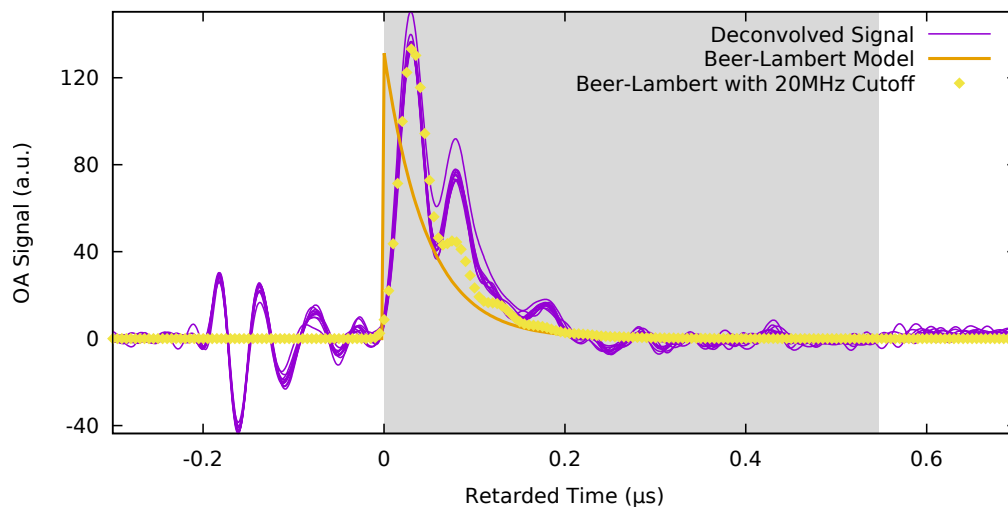


FIGURE 5.17: Post-processed signals of lesion W2-5-1 (purple). In the region from -0.2 – $0 \mu\text{s}$ in retarded time large parasitic oscillations are visible. Estimated Beer-Lambert model assuming homogeneous absorption of the lesion is depicted in orange. Yellow dots represent the model curve after a bandwidth cutoff at 20 MHz. The gray column in the background represents the thickness of the lesion as determined by histopathology. The OA signal ends long before the actual thickness of the lesion, according to histopathology, is reached.

The orange line represents the simple Beer-Lambert model which corresponds to a homogeneous absorber. Even with an absorption coefficient of 13 mm^{-1} , which is lower than expected for melanocytic tissue, the OA signal would decay below the noise level long before the bottom of the lesion is reached. This example clearly shows that a wavelength of 532 nm is too short for the investigation of melanoma into the depth of 1 mm. In addition, this specific nevus is highly irregular. Histopathological cuts determined very different thicknesses for different locations. The histology slice producing a thickness of 897 μm is depicted in Figure 5.18. Another histology slice (not shown) determined the thickness of the nevus to be 353 μm . In the photograph below the lesion can be seen. As before, the fish like mark on the top left represents the drawing of the surgeon determining the orientation of the histopathological slices. There are arguments to suggest a correlation between thickness and darkness, but there are too many factors to consider to rely on such rules of thumb. The measurements presented here are performed in the region of the dotted circle in the photograph.

It is well possible that the histopathology producing the 897 μm thickness was measured at a different position. Being limited by penetration depth at a wavelength of 532 nm it is only possible to confirm a thickness of more than 135 μm , as explained before. The histopathology slice in Figure 5.18 also shows that it is not realistic to use the intensity of the histology marker to determine the melanin concentration or the absorption behavior in general.

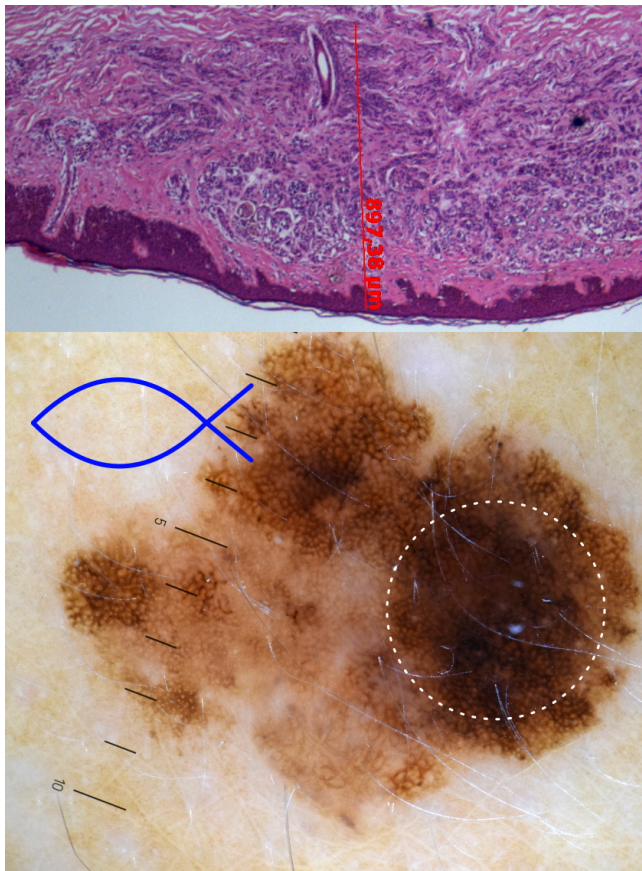


FIGURE 5.18: Photography and histology of lesion W2-5-1. Histology (top) shows a thickness of 897.38 μm . The blue symbol on the left represents the drawing by the surgeon indicating the orientation of the cuts and thus the orientation of the histology. Here, the histopathological cut is vertical in the picture. The scale is in mm. The white dashed circle indicates the area where the measurement was performed, it lies on top of the darker part on the right-hand side. The lesion is highly inhomogeneous. The form of the boundary deviates from a circle. Throughout the lesion the pigment concentration varies as visible by eye.

Chapter 6

Conclusion and Outlook

In this thesis a self-build handheld OA setup was developed. The goal was the creation of a handheld setup for clinical measurements on pigmented skin lesions, suitable to meet the demands imposed by day-to-day use. Centerpiece of this setup is a piezoelectric PMMA film on which ITO electrodes are sputtered to create an ultrasound transducer capable of recording OA signals. Optical transmission spectroscopy confirmed transparency of the detector in the infrared and visible wavelength range, down to 400 nm. For lower wavelengths transmission dropped to zero due to high absorption in the ITO layers.

To validate the functionality of intermediate detector setups and provide information on various features of the OA signal, phantom studies were conducted. Specimen composed of stackable PVA hydrogel layers with varying melanin concentrations facilitated measurements under laboratory conditions without the complications of in-vivo procedures. The resulting OA signals mapped the absorption depth profile of the phantoms and proved the fundamental capacity of this kind of transparent detector setup to determine the thickness of absorbing layers in the far field regime. To investigate the influence of acoustic diffraction on the OA signal, off-axis measurements were performed. For these measurements the OA source was moved to different locations underneath the detector, by tilting the illumination angle. It could be shown that small deviations from the detector axis ($<5^\circ$) produce only minor changes in comparison to on-axis signals. Therefore, far field measurements where the illumination occurs from the side of the detector, still can be regarded as on-axis.

In order to facilitate near field measurements, the illumination was performed through the detector. Due to the non-zero absorption in the active area of the detector itself, this produced a pyroelectric effect overlaying the OA signal. Comparison to the absorption spectrum of the detector film showcased the possibility to use the pyroelectric effect in the signal to monitor the energy of the incident laser pulse. Unfortunately, further investigations into the pyroelectric signal showed that its amplitude depends, among other factors, on the electrical capacity of the sample. In case of in-vivo measurements this parameter cannot be easily controlled, thus, this approach of energy monitoring was not pursued further. Nonetheless, the pyroelectric signal was used to determine the precise extent of the detector. The comparison between a microscope image and the mapping of the active area verified a precise fit to the area of overlap of the two ITO electrodes. Hence, the transducer production was shown to accurately reproduce the design of the sputter masks. This was not only important to validate production fidelity but allowed us to determine the position of the active area by eye, simplifying the measurement process greatly.

Different setup designs were tested for their viability in the clinical trials. The first prototypes were unsuited due to impractical handling. Prime examples for this are the hydrogel backing layers which in theory are the best choice with respect to their acoustic properties. However, it became obvious that using backing layers, which cannot be fixed to the detector and dry out in the course of hours, is not feasible for in vivo measurements. By contrast, regarding measurements on phantoms under laboratory conditions the PVA-H backing layers proved to be well suited, as is evident from the successful far field measurements on hydrogel samples presented in this thesis.

A PMMA backing layer provided a well-suited compromise of acoustical properties; similar enough to the PVDF film and not too different from living tissue, which is stable over time and can be fixed permanently on the detector.

In the end, successful OA measurements on pigmented skin lesions, in vivo under routine clinical conditions, were demonstrated. Thanks to the PMMA fronting layer used for the clinical setup, the detector was well protected from mechanical strain and offered reliable measurement conditions by creating a fixed time delay before the OA wave arrived at the detector. During this time window, which is constant for all measurements, only the pyroelectric effect is present and can be fitted reliably. This led to a

post-processing protocol which could be applied to any measurement performed with this detector setup. Only minor adjustments have to be made for individual samples, to optimize the fitting process to include all regions without an OA signal. In addition to the removal of the pyroelectric effect, the post-processing procedure entails deconvolving the instrument response function (IRF) from the signal. Due to high noise levels in the frequency range above 20 MHz during the back-transformation, this part of the spectrum had to be suppressed. A direct determination of the absorption profile in the near field measurements was prevented by oscillating artifacts produced by the Fourier transformation. Several experimental results agreed well with simulations by assuming a simplified absorption model following the Beer-Lambert law which was submitted to the same process of Fourier transformation and low-pass filtering.

As a result of these advances, it was possible to show the potential of OA measurements through a transparent piezoelectric detector. Especially in the medical field where the handling and usability of a device is very important, this technique might have a promising future. With future investigations with respect to the use of multiple detectors, imaging could be implemented as well. Due to the fast progress in the field of OAs and the vast wealth of knowledge already acquired, great synergy effects can be expected. Building on methods already implemented in OA technology, such as partial view image reconstruction, this new type of setup could become complementary to existing techniques. Even in a single detector setup this approach showed its potential in determining the thickness of skin lesions.

Limitations exist for the approach of using an optically transparent detector, which are unlikely to be overcome in the foreseeable future. While ITO has proven itself to be highly useful to create electrically conducting but optically transparent coating on layered structures, it fails in replacing metals in other aspects, such as wiring. Thus, ITO pathways must function as electrodes to connect the ITO detector to the data acquisition device, inhibiting miniaturization of the transparent detector setup and in consequence the use of multiple detectors in close vicinity.

However, there are a few realistic steps which could be taken to allow the setup presented here to reach its full potential. By rebuilding the setup in a metal case, higher stability could be accomplished. More importantly, the electromagnetic shielding could be realized

within the handheld device itself. This would not only improve signal quality but relieve the experimentalist as well as the patient from the restrictions of the grounding wires. A CCD camera could be installed above the OA detector to simplify its positioning on the lesion even more. Furthermore, a tunable and more stable laser source is needed to determine the thickness of pigmented nevi of 1 mm thickness or more, which is the most relevant tumor penetration depth in melanoma screening. In this work, a wavelength of 532 nm was chosen, to ensure a strong optical contrast of the OA measurements. However, with increasing knowledge about the signal properties in combination with the structural changes mentioned above, less contrast will be needed to evaluate the OA signal, allowing longer wavelengths to be used. Eventually, a single wavelength could be determined, that satisfies the compromise between penetration depth and contrast. If multiple wavelengths are still needed, pulsed laser diodes might present a cost-efficient alternative to tunable laser sources.

A conceivable future application for the technique presented in this thesis could be inside of an OA “pen” for dermatologist to enhance the established process of skin cancer screening. Instead of the dermatoscope, the CCD camera inside the pen can be used to allow close visual examination of lesions in accordance with medical practice. Therefore, very little training would be necessary on the part of the physicians. Furthermore, the OA measurement would facilitate real time depth inspection. In contrast to 3D-tomography, which needs large computing resources and careful interpretation by the clinician, the device could produce simple information. Depending on the location of the lesion, the device could give confidence values that the penetration depth is less than a certain limit relevant for the staging.

Appendix A

Clinical Measurements using the SYM Detector Setup

Here, all OA measurements utilizing the SYM detector setup in the context of the clinical trials of the MeDiOO project are presented. For each lesion¹ three figures are arranged in the following way. On the left-hand side, the OA signals after the removal of the pyroelectric effect are presented in turquoise and the resulting curve after the deconvolution of the instrument response function in purple. The gray column in the background corresponds to the thickness as determined by histology.

The histological cut is presented in the top right of the arrangement. Below a photograph of the lesion is shown. When available these photographs were taken by a digital dermatoscope which is specifically designed for closeups of the skin. Otherwise the picture was taken through the optics of an analog dermatoscope.

¹For some lesions two positions were measured. In those cases, both measurement series are shown on consecutive pages under the same headline.

A.1 W2-2-1

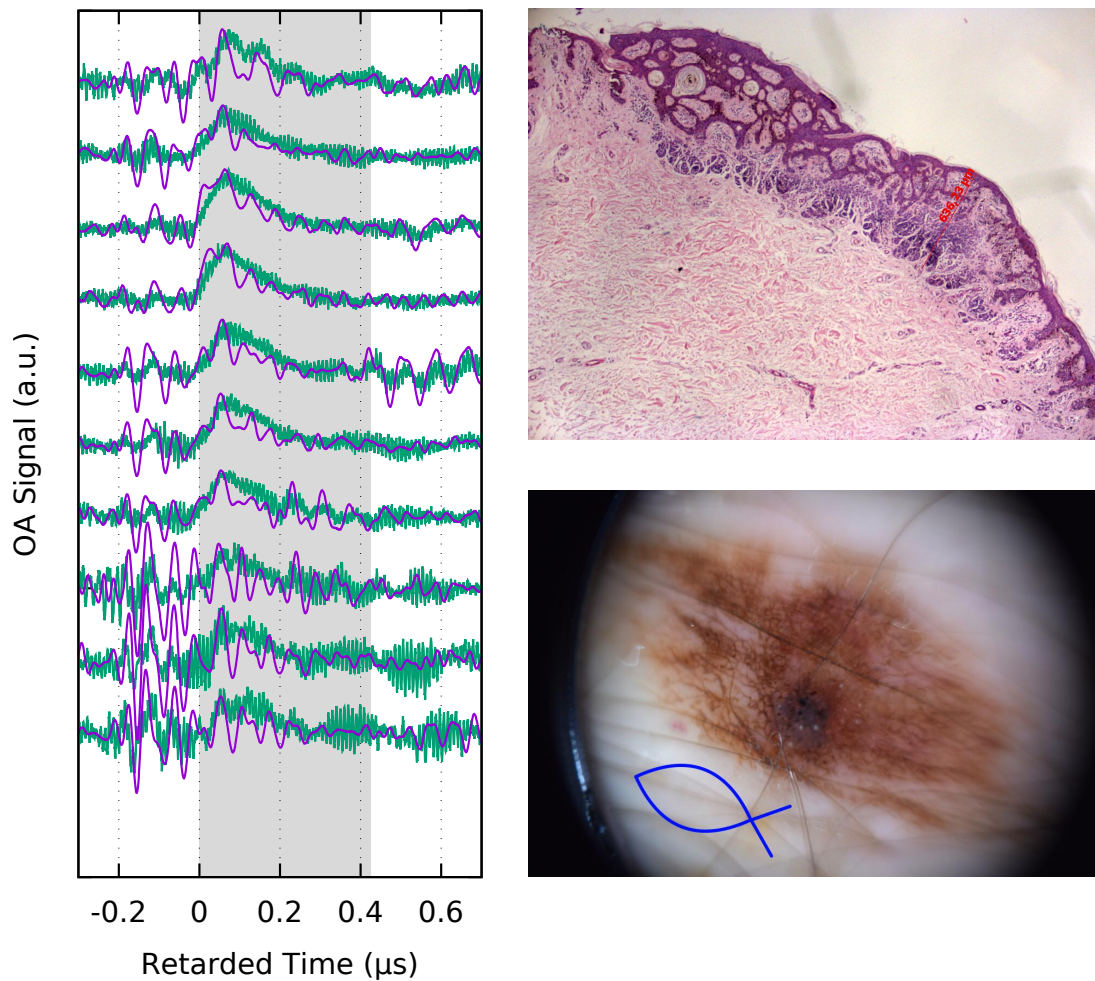


FIGURE A.1: W2-2-1. Noise dominates the OA signal. In contrast to later measurements the noise oscillations differ strongly in this set of signals, probably resulting from movements of the patient. Histological thickness is $636\ \mu\text{m}$. The special camera to take skin closeups was damaged. Thus, the photo was taken with a regular camera through the analog dermatoscope.

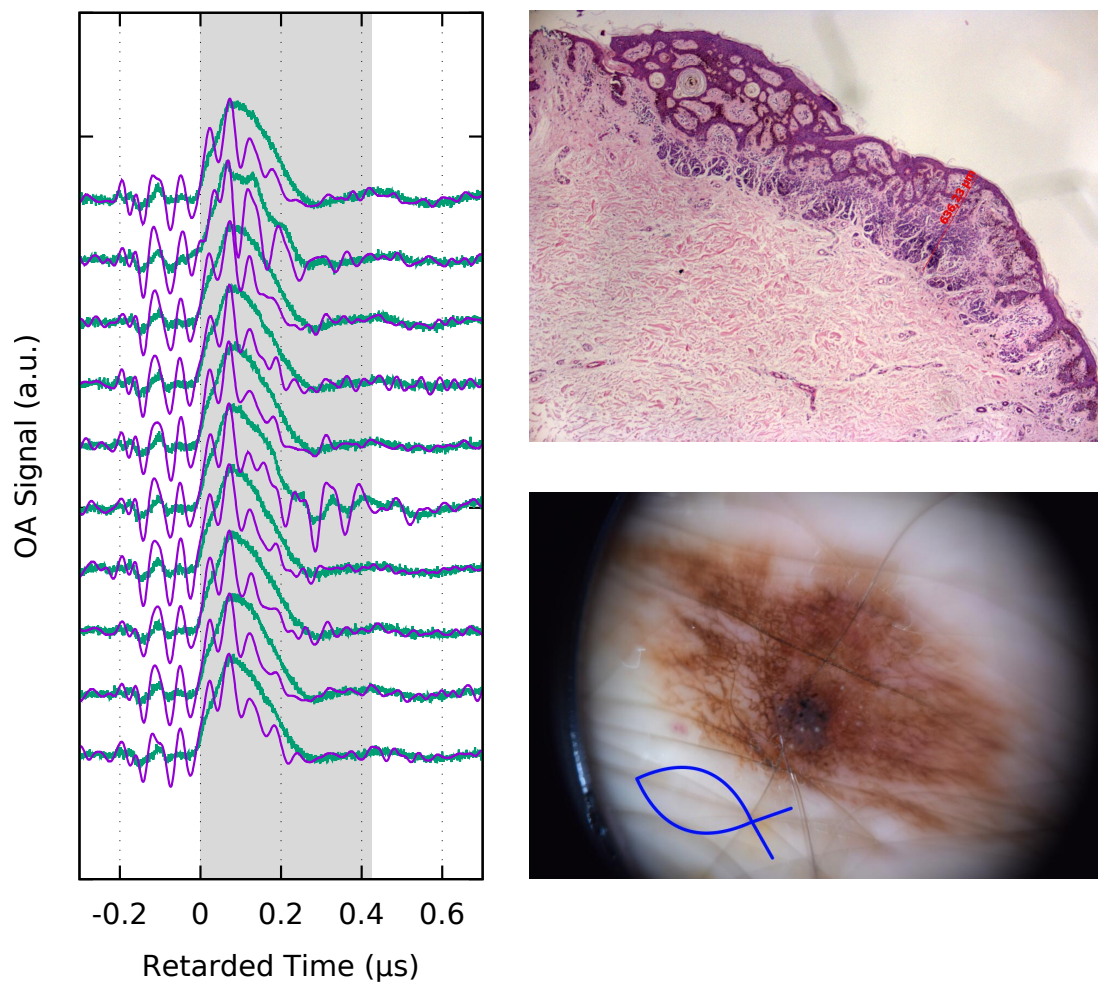


FIGURE A.2: W2-2-1. Measurements taken on top of the dark spot in the center of the lesion. Histological thickness is 636 μm .

A.2 W2-2-2-1

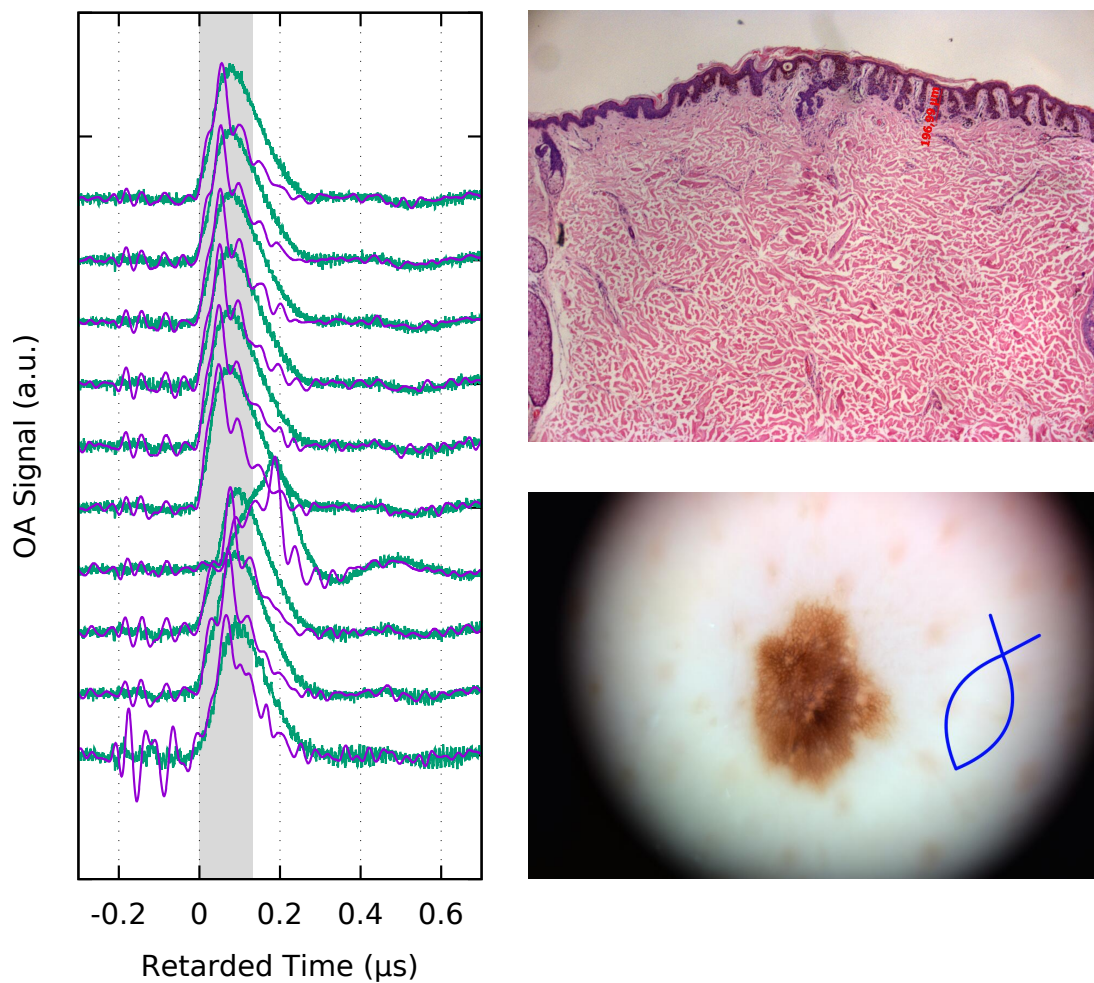


FIGURE A.3: W2-2-2-1. Histological thickness is $197\ \mu\text{m}$. The seventh OA measurement from the top was distorted through a handling error.

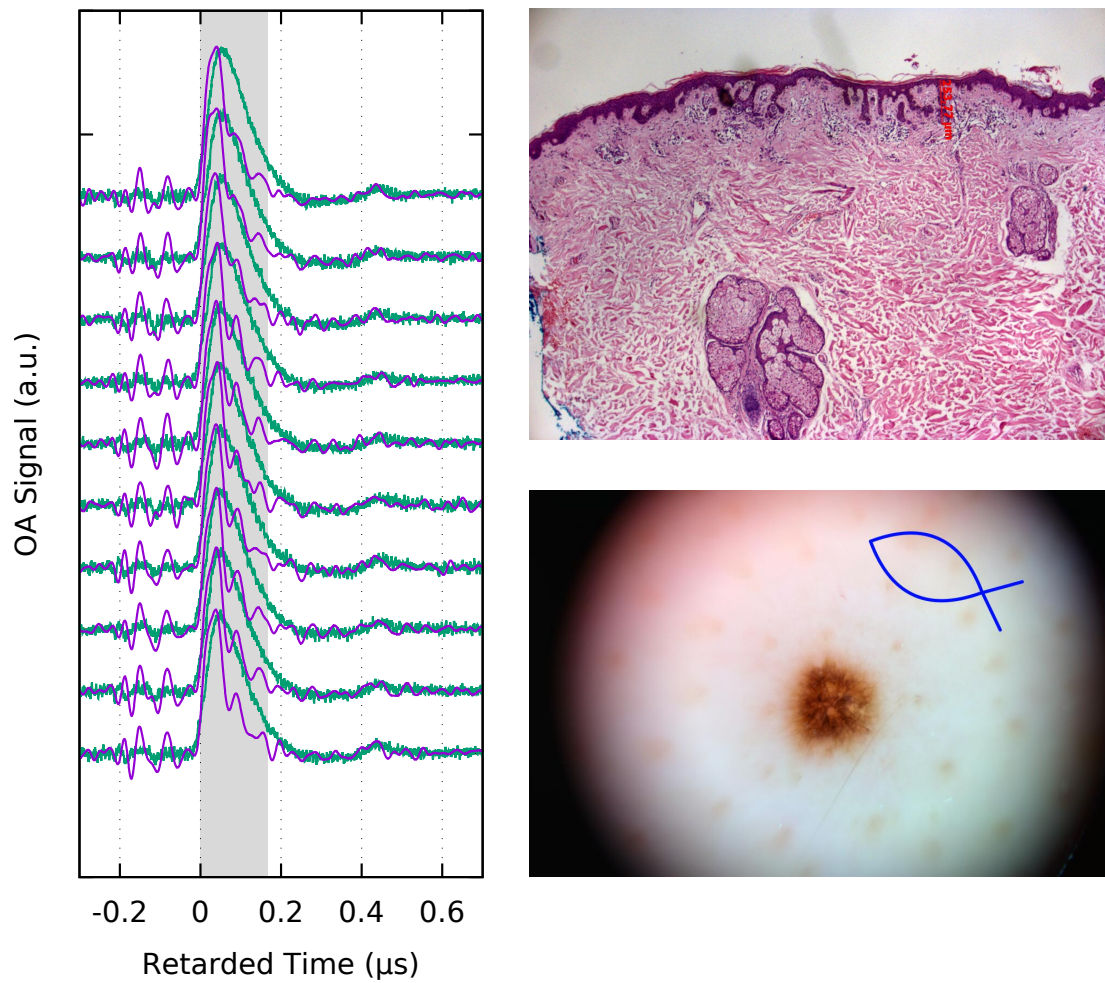
A.3 W2-2-2-2

FIGURE A.4: W2-2-2-2. Histological thickness is $254\ \mu\text{m}$. The special camera to take skin closeups was damaged. Thus, the photo was taken with a regular camera through the optics of an analog dermatoscope.

A.4 W2-3-1

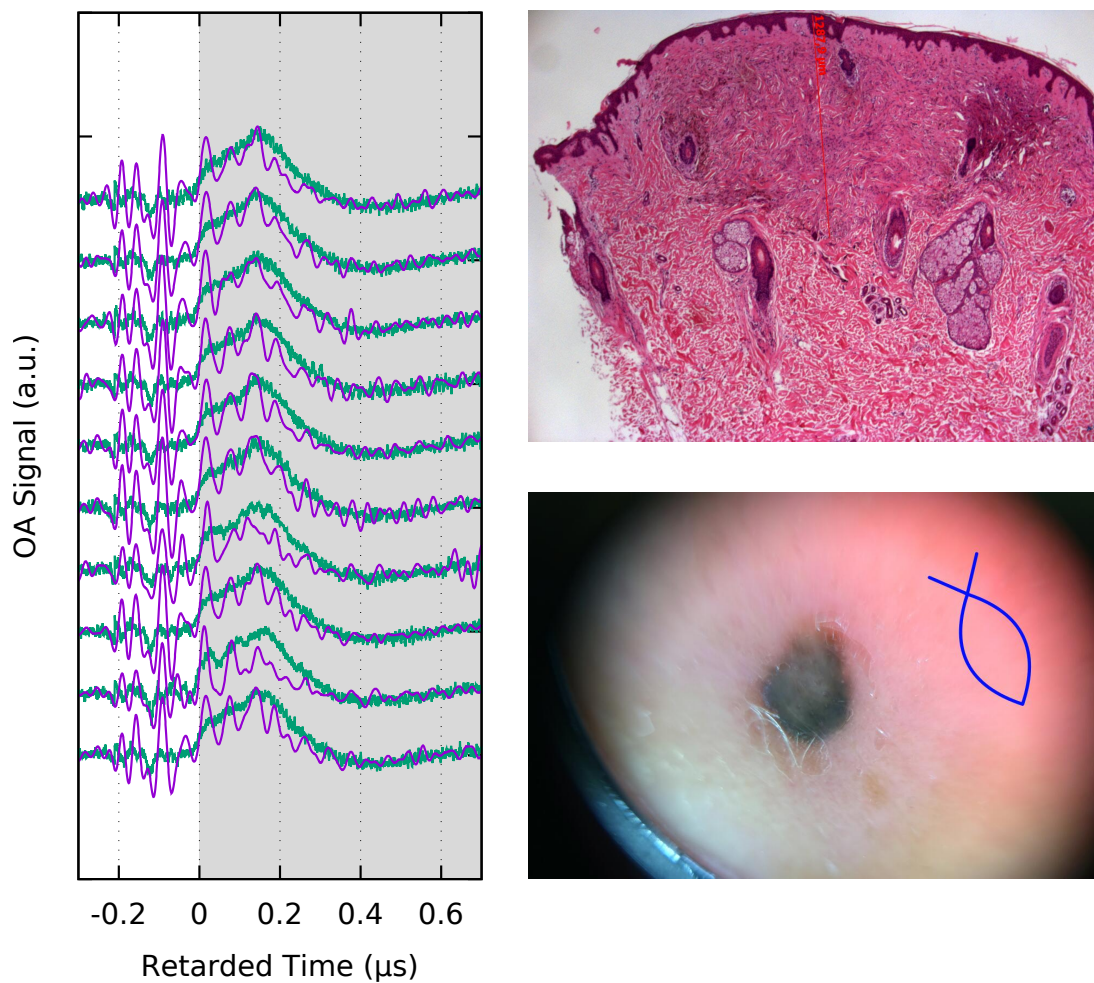


FIGURE A.5: W2-3-1. Histological thickness is $1.288\ \mu\text{m}$. The special camera to take skin closeups was damaged. Thus, the photo was taken with a regular camera through the optics of an analog dermatoscope. Noise dominates the OA signal impeding the further use of the data.

A.5 W2-3-2

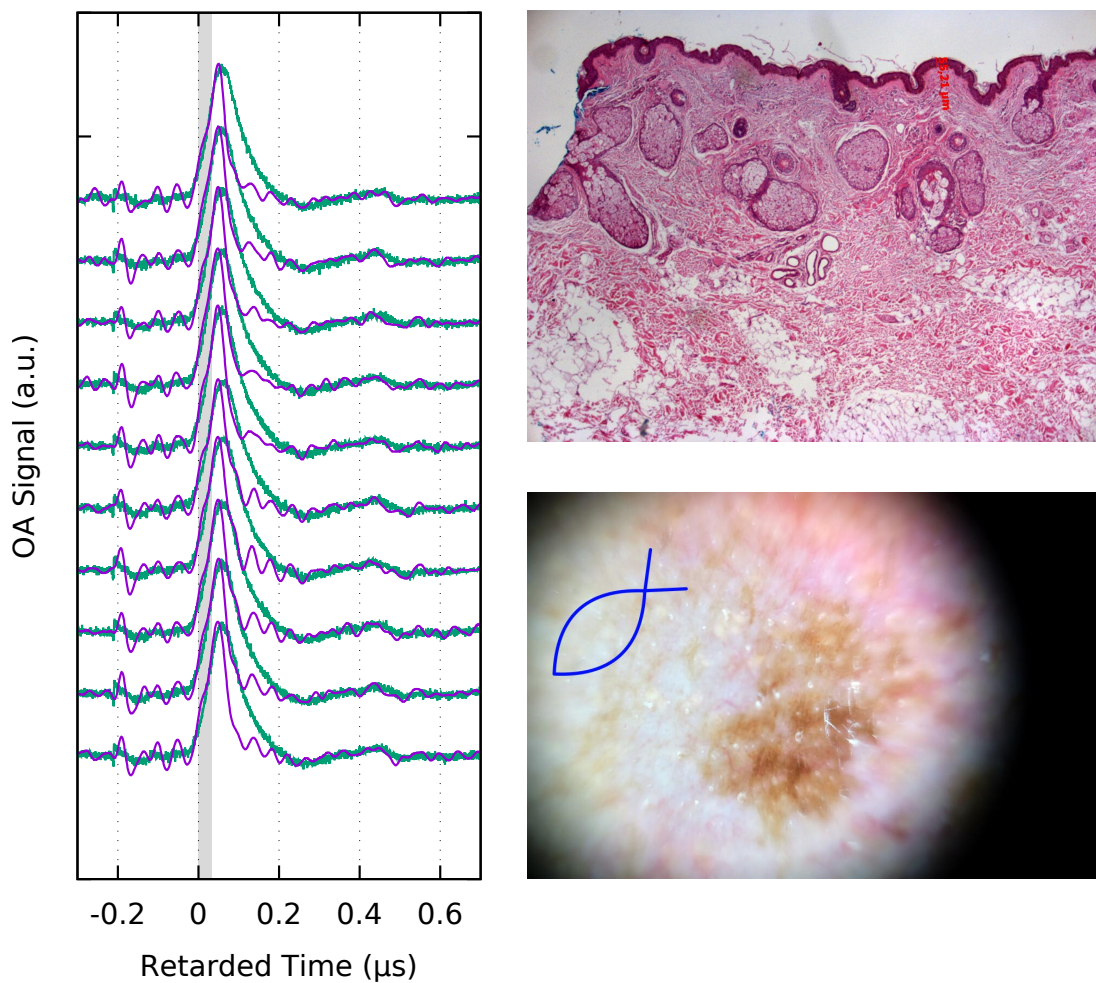


FIGURE A.6: W2-3-2. Histological thickness is 55 μm . The special camera to take skin closeups was damaged. Thus, the photo was taken with a regular camera through the analog dermatoscope. The surface of the lesion is very uneven prohibiting a proper acoustic connection with the detector setup.

A.6 W2-4-1

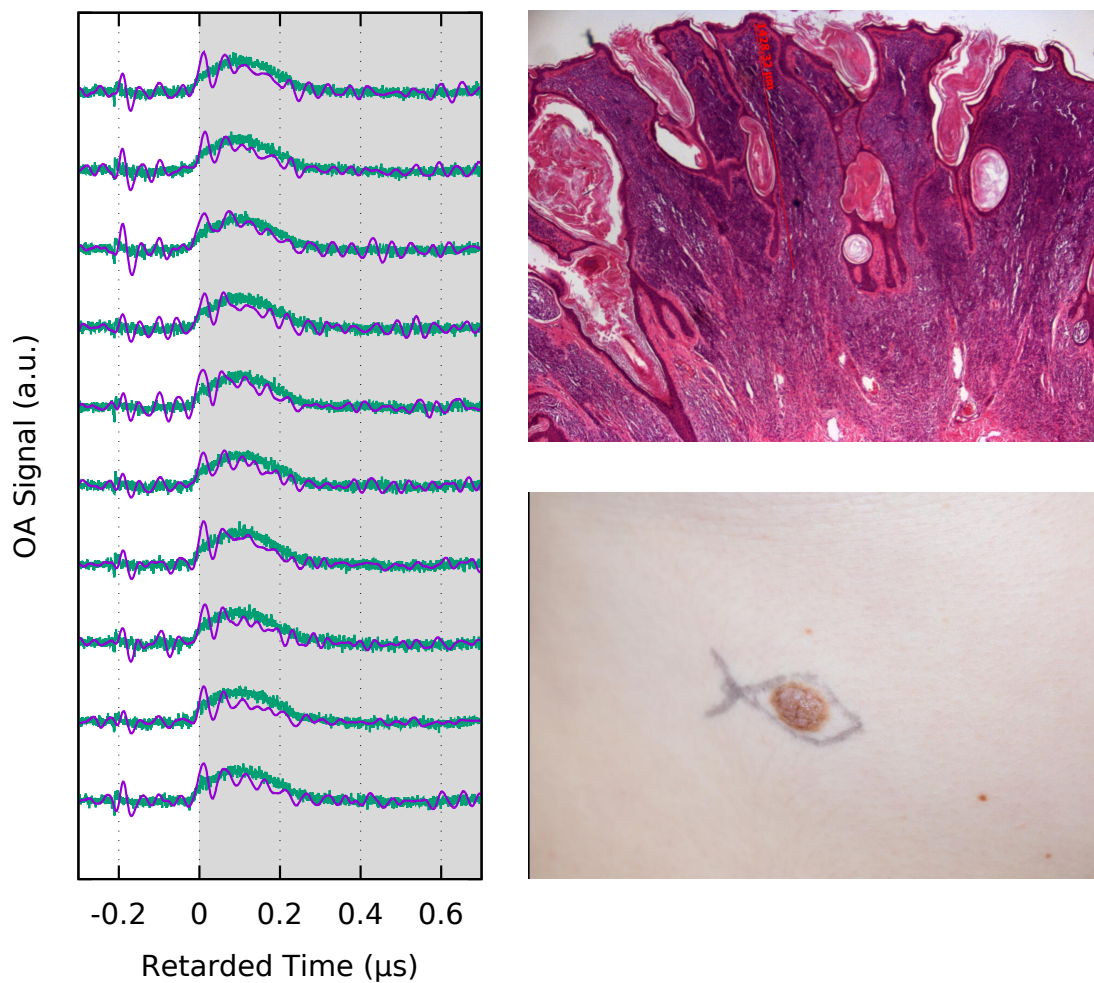


FIGURE A.7: W2-4-1. Histological thickness is 1.428 μm . The nevus extends several millimeters from the skin, which makes it unsuitable for the OA measurement setup designed in this work. Because the surface is highly uneven which impedes the inspection with the dermatoscope. The photograph was taken with a regular camera.

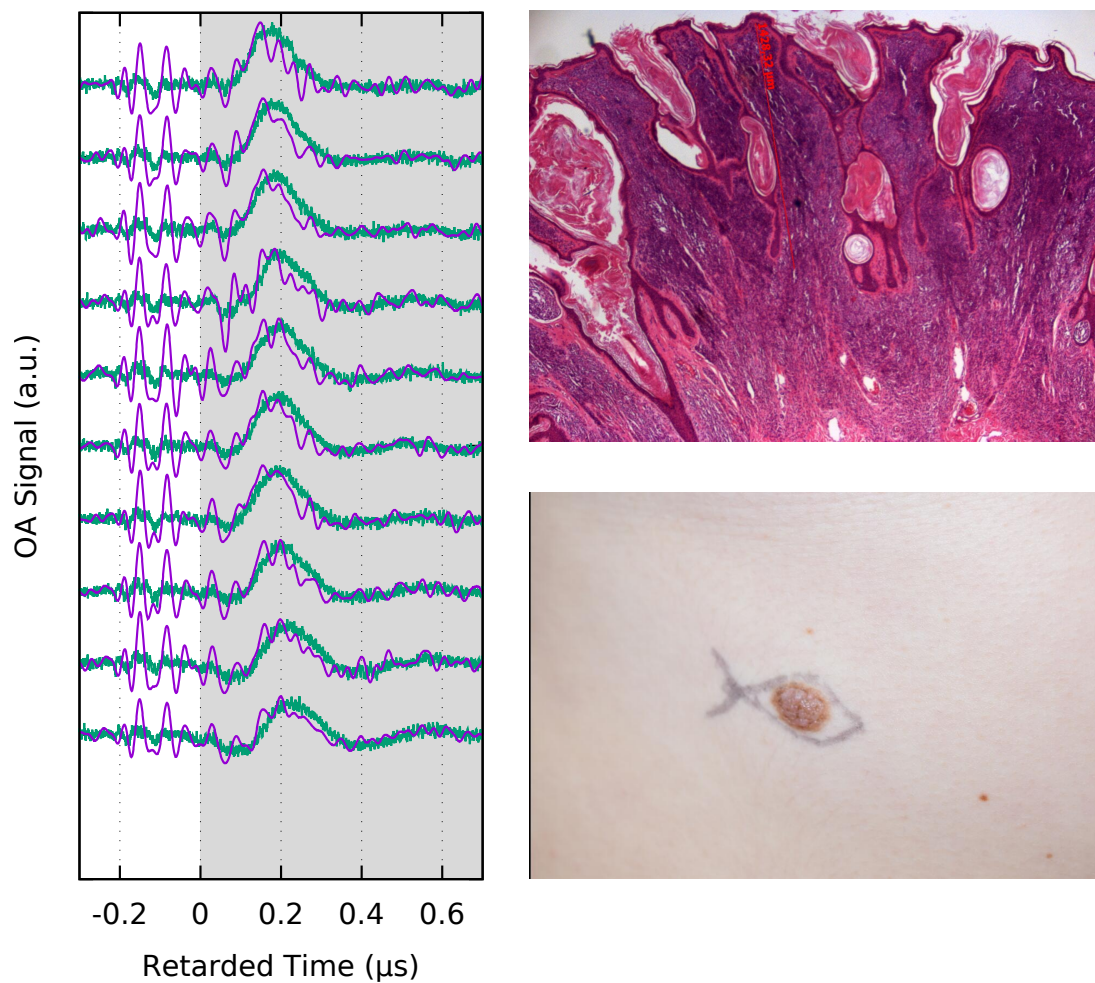


FIGURE A. 8: W2-4-1. Same lesion as before, see previous page. Here OA measurements were performed at the fringe of the lesion. Due to the curved nature of the surface, the sensor was not in direct contact with the nevus and the main feature in the OA signal begins approximately $0.1 \mu\text{s}$ after $t = 0$.

A.7 W2-4-2

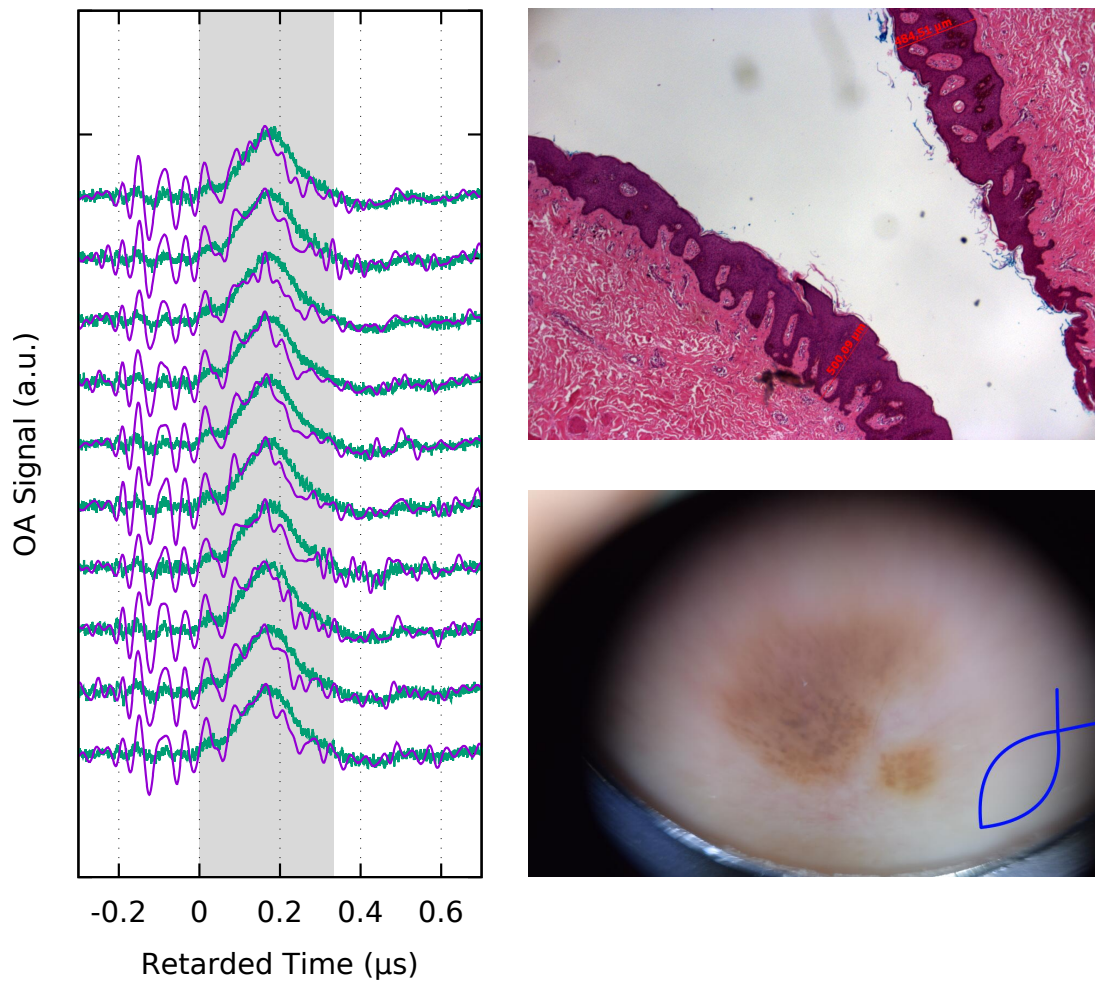


FIGURE A.9: W2-4-2. Histological thickness is 500 μm (left) and 485 μm (right), respectively. Noise strongly dominates the resulting signal. Not even the beginning of the lesion is distinguishable in the OA signal.

A.8 W2-5-1

Please note that the precise position of the histopathological cut is unknown. For lesion W2-5-1, two histopathological images were taken, and two sets of measurements were conducted at different positions. The images were assigned to the measurement they match better, respectively. At the location where the nevus is darker, it is assumed to be thicker. Further studies would be required with exact knowledge of the position of the histology to be able to directly compare the images to the OA measurements. The second measurement on this lesion can be found on the next page.

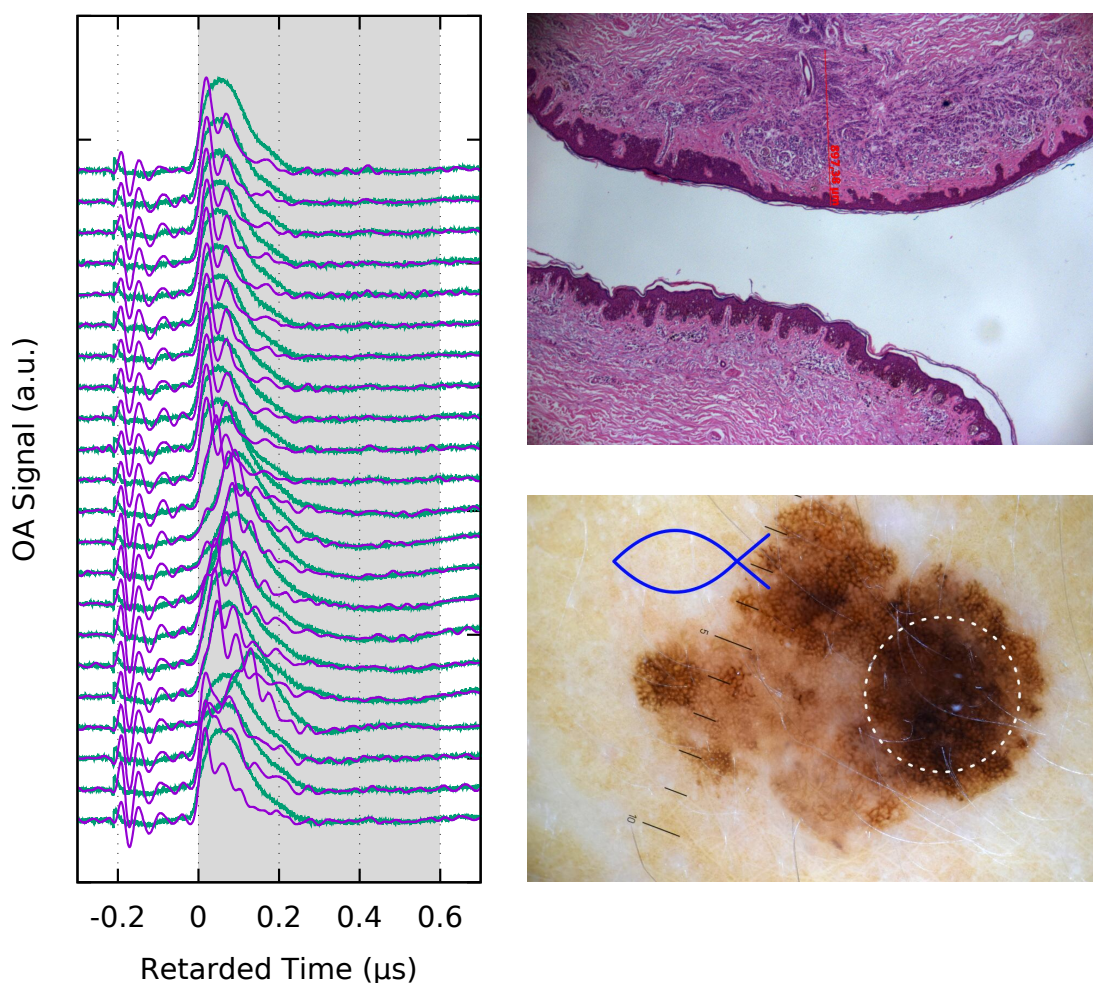


FIGURE A.10: W2-5-1. The top 10 OA measurements are discussed in detail in the results section. Due to handling errors the other measurement were rendered unusable. Histological thickness is $897\ \mu\text{m}$. The white dashed ring in the dermoscope picture indicates the approximate position of the measurements.

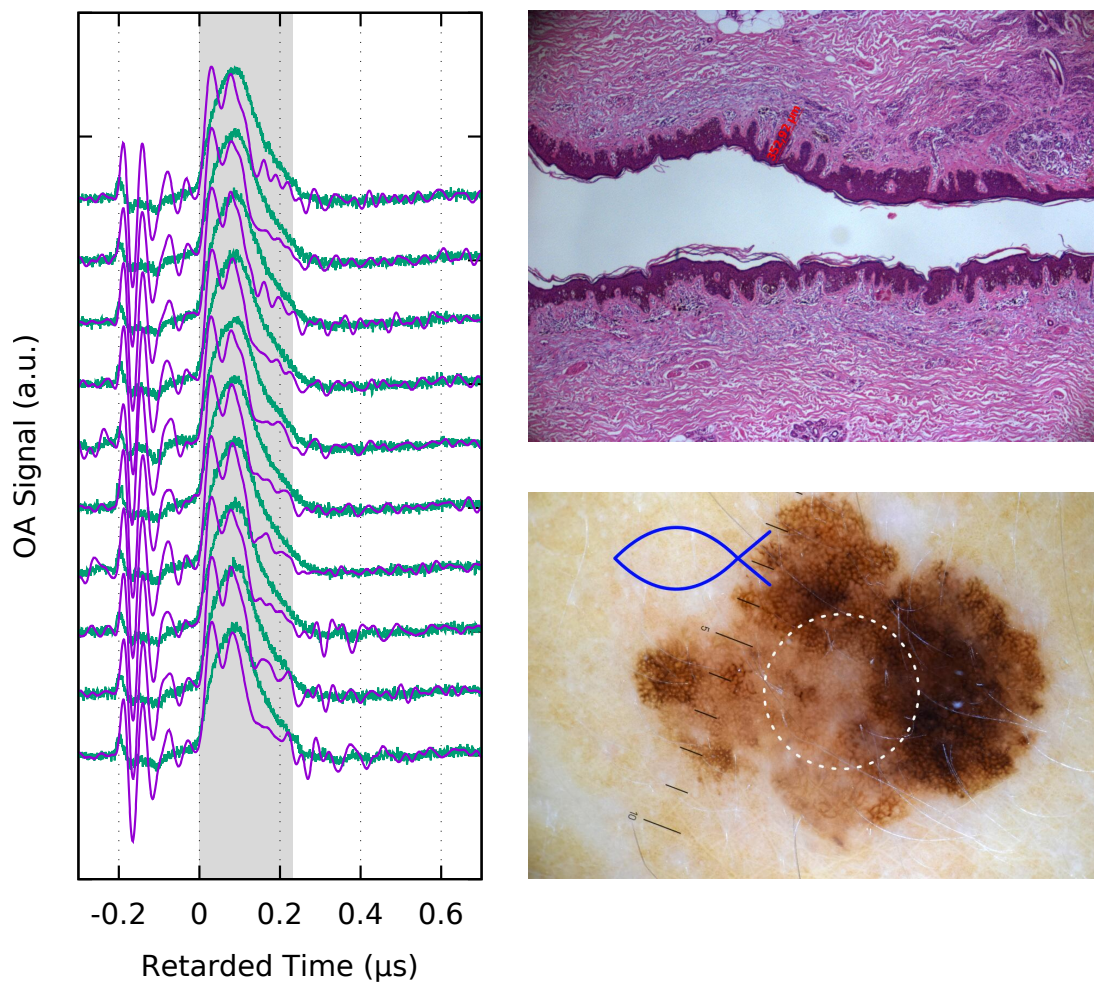


FIGURE A.11: W2-5-1 Light Middle. Histological thickness is 353 μm . The white dashed ring in the dermatoscope picture indicates the approximate position of the measurements.

A.9 W2-5-2

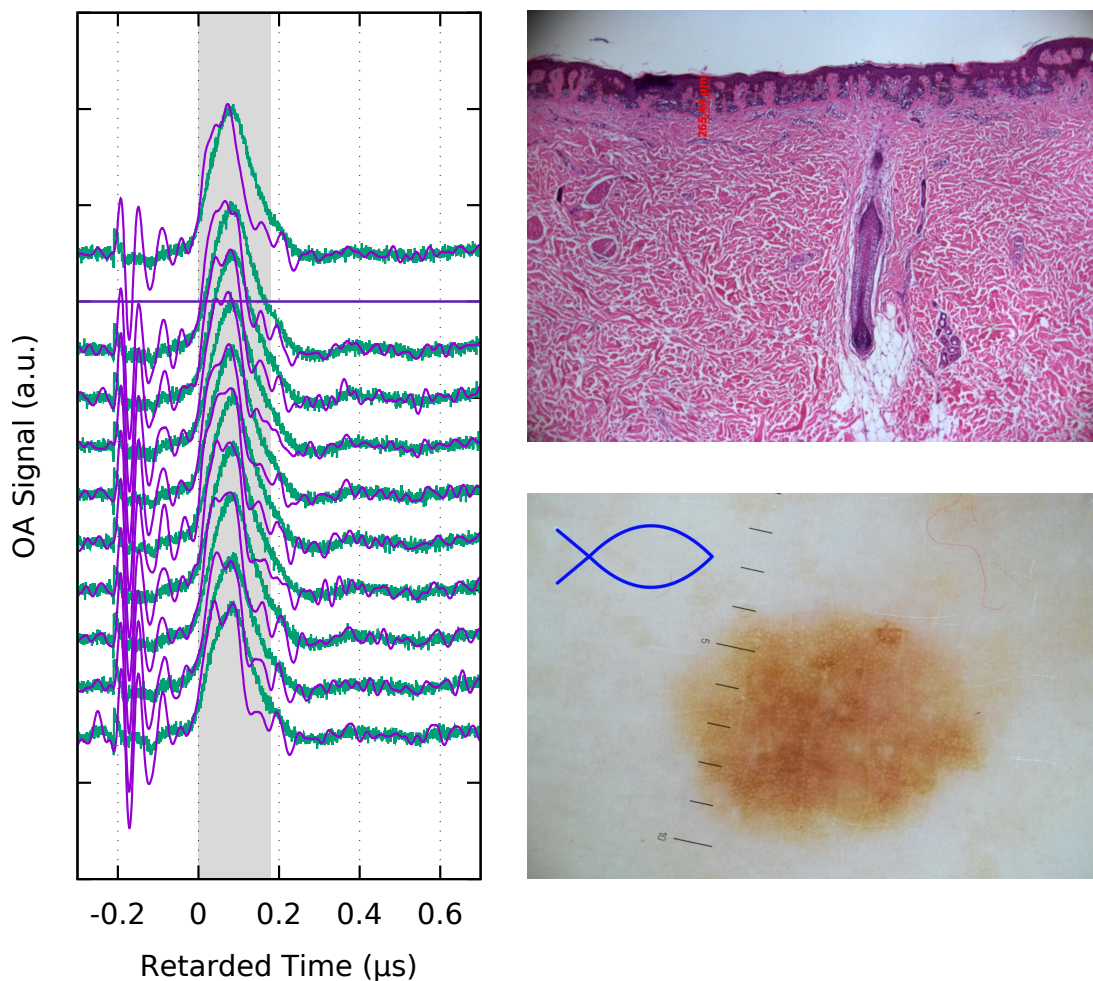


FIGURE A.12: W2-5-2. Discussed in detail in the results section. Strong pickup of the electromagnetic noise from the laser source. Fortunately, the signal is strong enough to be discerned nevertheless. Second measurement from the top: energy monitoring failed due to a handling error of the fiber, thus the energy normalized curve could not be calculated. Histological thickness is 265 μm .

A.10 W3-2-1-1

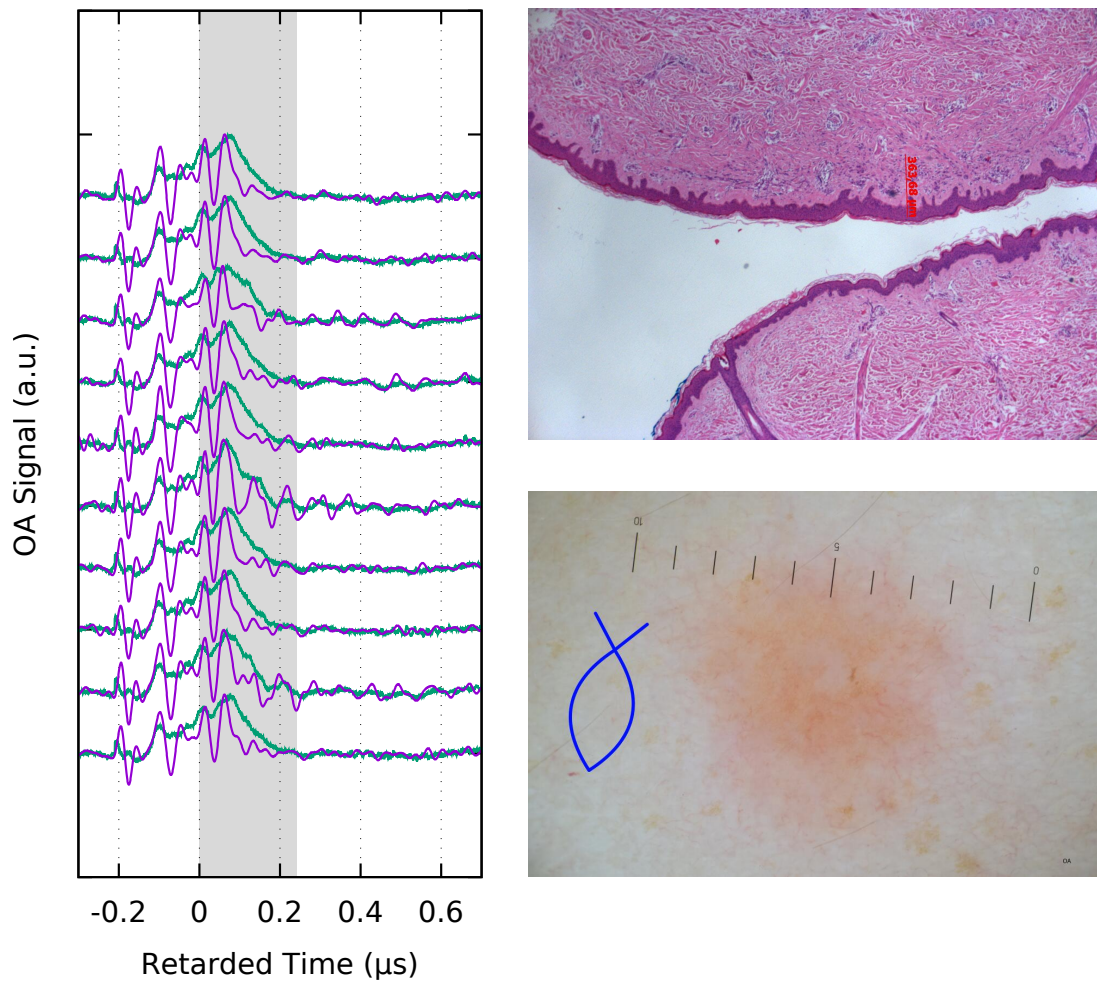


FIGURE A.13: W3-2-1-1. Very strong noise dominates the signal. Not even the beginning of the OA signal can be determined. Histological thickness is 364 μm . Dermatoscopy shows low contrast between nevus and the surrounding skin.

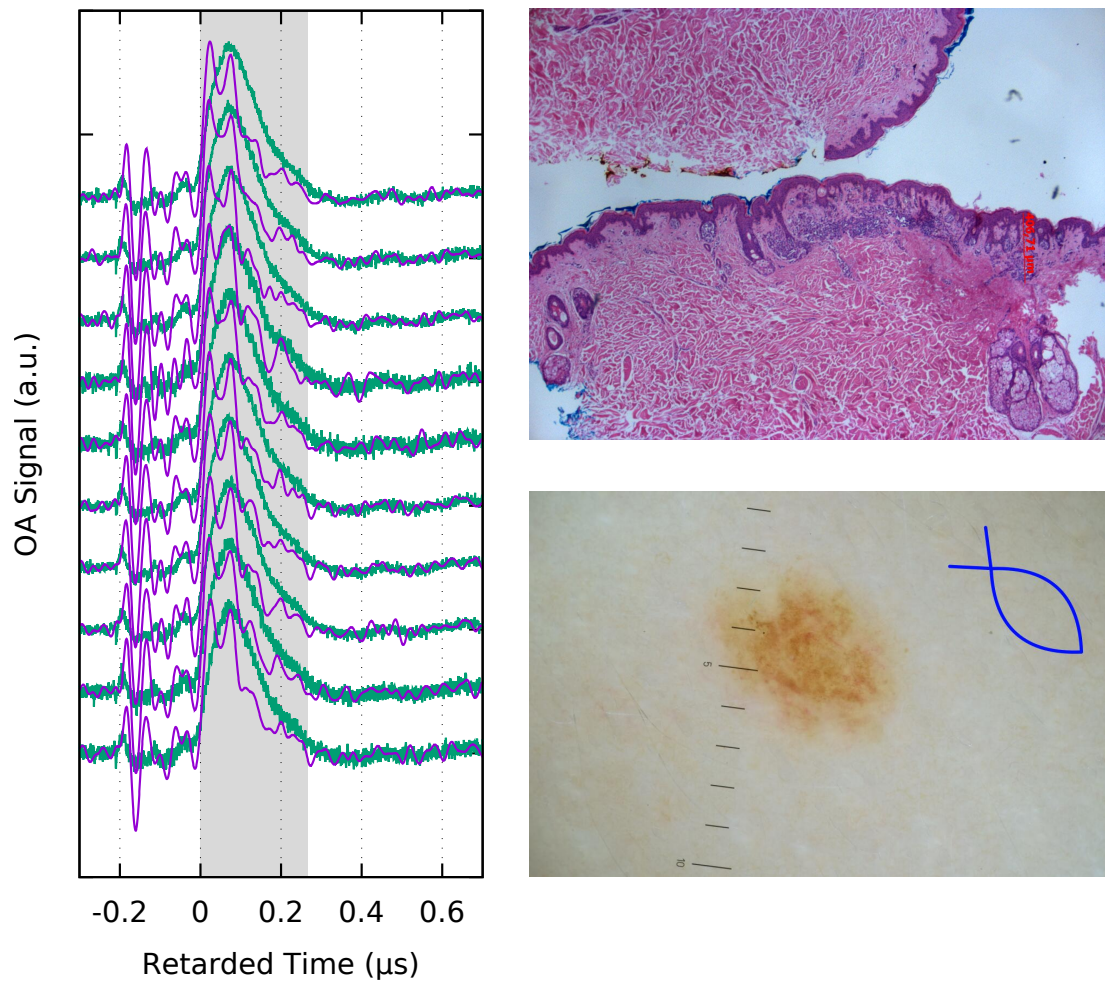
A.11 W3-2-1-2

FIGURE A.14: W3-2-1-2. Histological thickness is $407\mu\text{m}$. According to the histopathological cut the thickest part is at the fringe. However, the measurements are performed approximately in the middle of the lesion. This might explain why the prominent drop takes place significantly before the determined thickness. Noise levels comparable to the signal are further impeding the evaluation.

A.12 W3-2-2-1

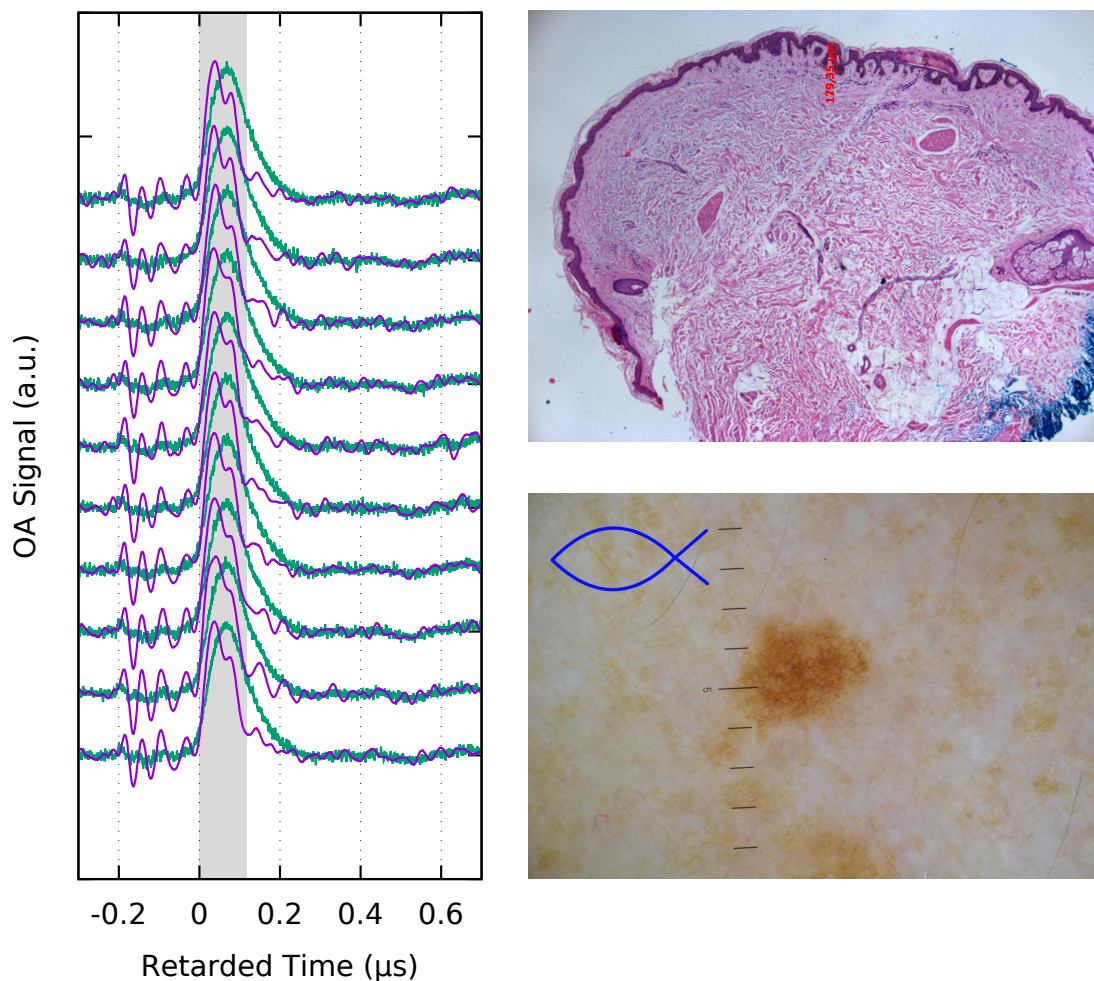


FIGURE A.15: W3-2-2-1. Histological thickness is $179\mu\text{m}$. At a first glance, the OA curve matches the thickness quite well. However, the two peaks of the main feature are too similar in height to be explained by the simple absorption model used in this thesis. A possible explanation might be found in the dermoscopy image where the center of the nevus exhibits spots of lighter skin. If we assumed direct correlation to the absorber concentration, these spots would result in a higher light distribution in deeper layers. This could also explain why the signal does not return to zero at the bottom of the nevus.

A.13 W3-2-2-2

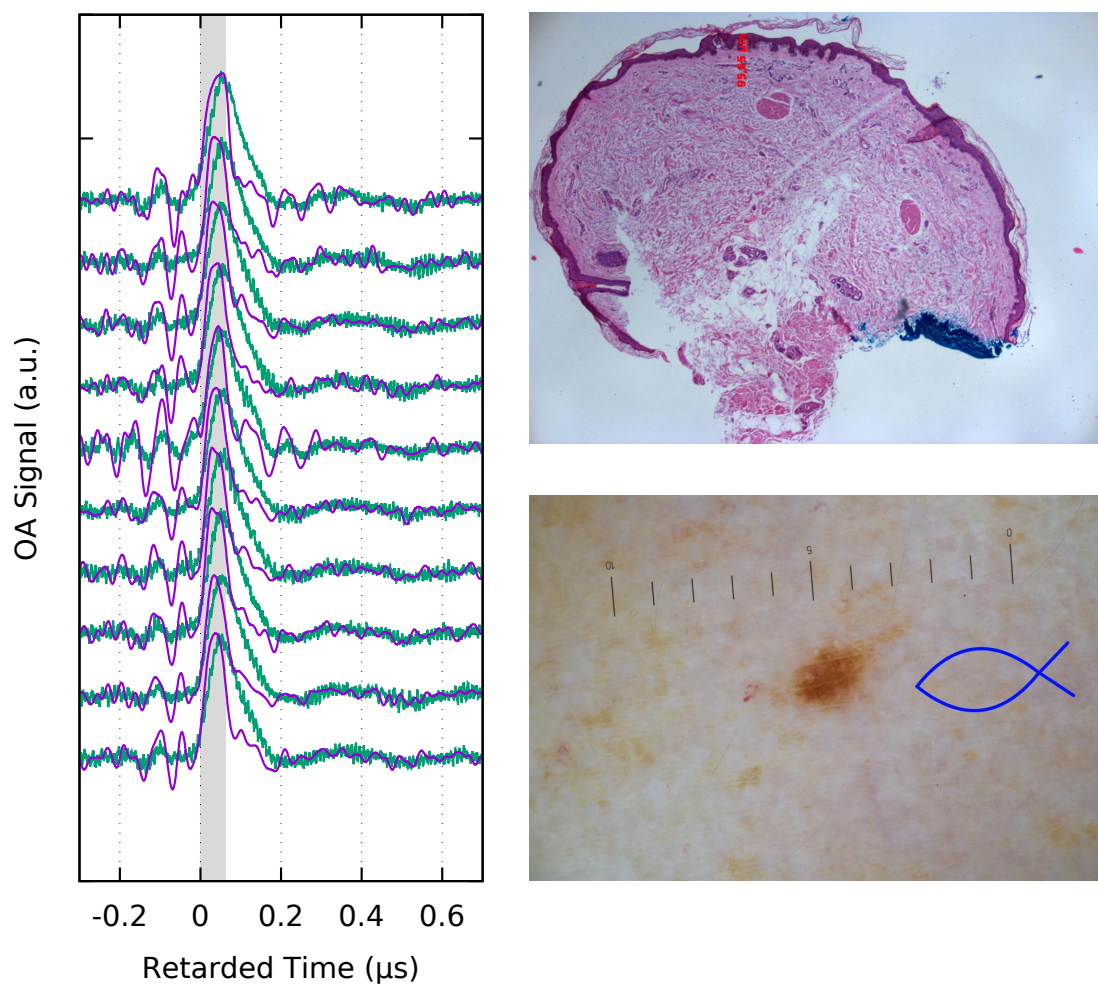


FIGURE A.16: W3-2-2-2. Discussed in detail in the results section. Histological thickness is 96 μm .

A.14 W3-3-1

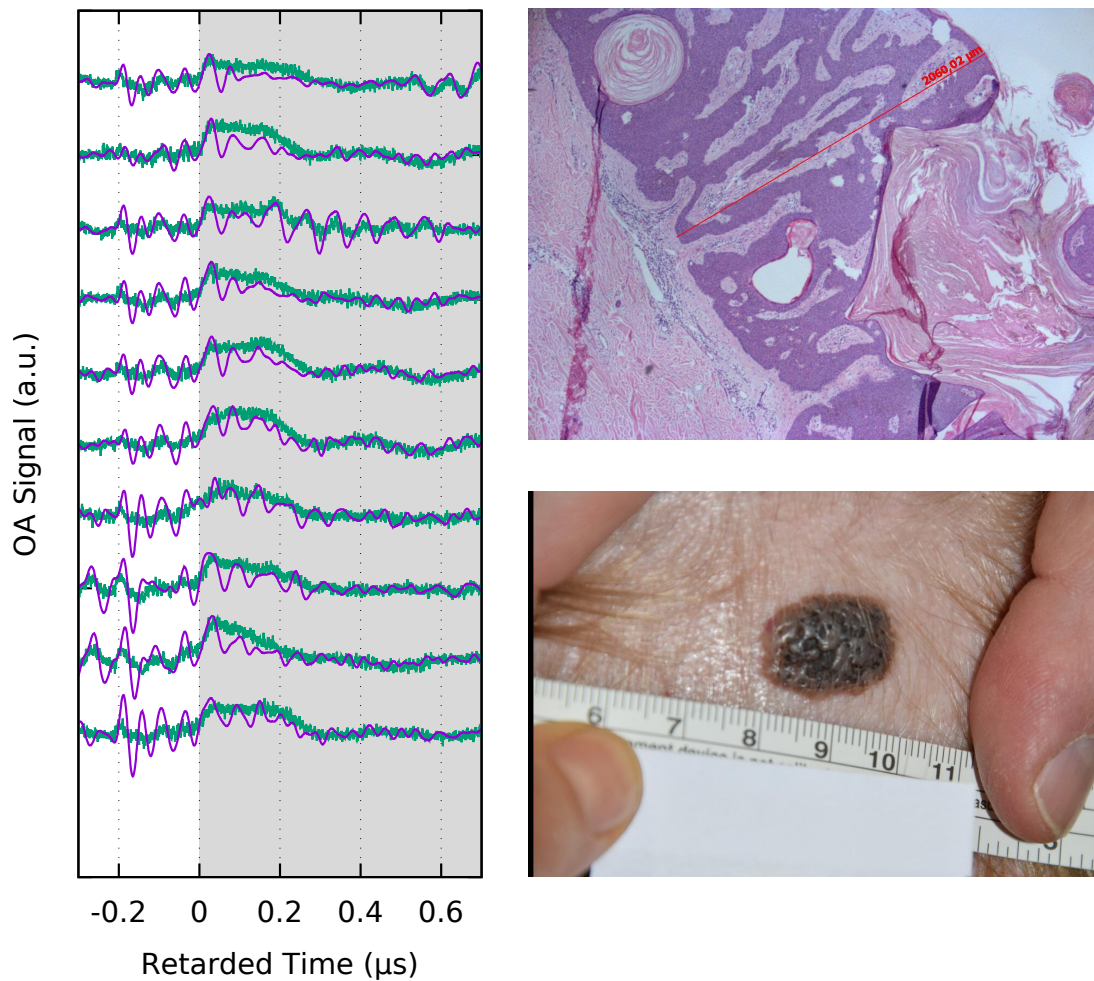


FIGURE A.17: W3-3-1. Histological thickness is 2.060 μm . Due to the large size of the lesion the digital dermatoscope could not be used. Instead the lesion was photographed next to a ruler. The OA measurements are dominated by noise. Main cause for the strong noise was the location of the lesion on the head, which is difficult to ground properly.

A.15 W3-3-2-1

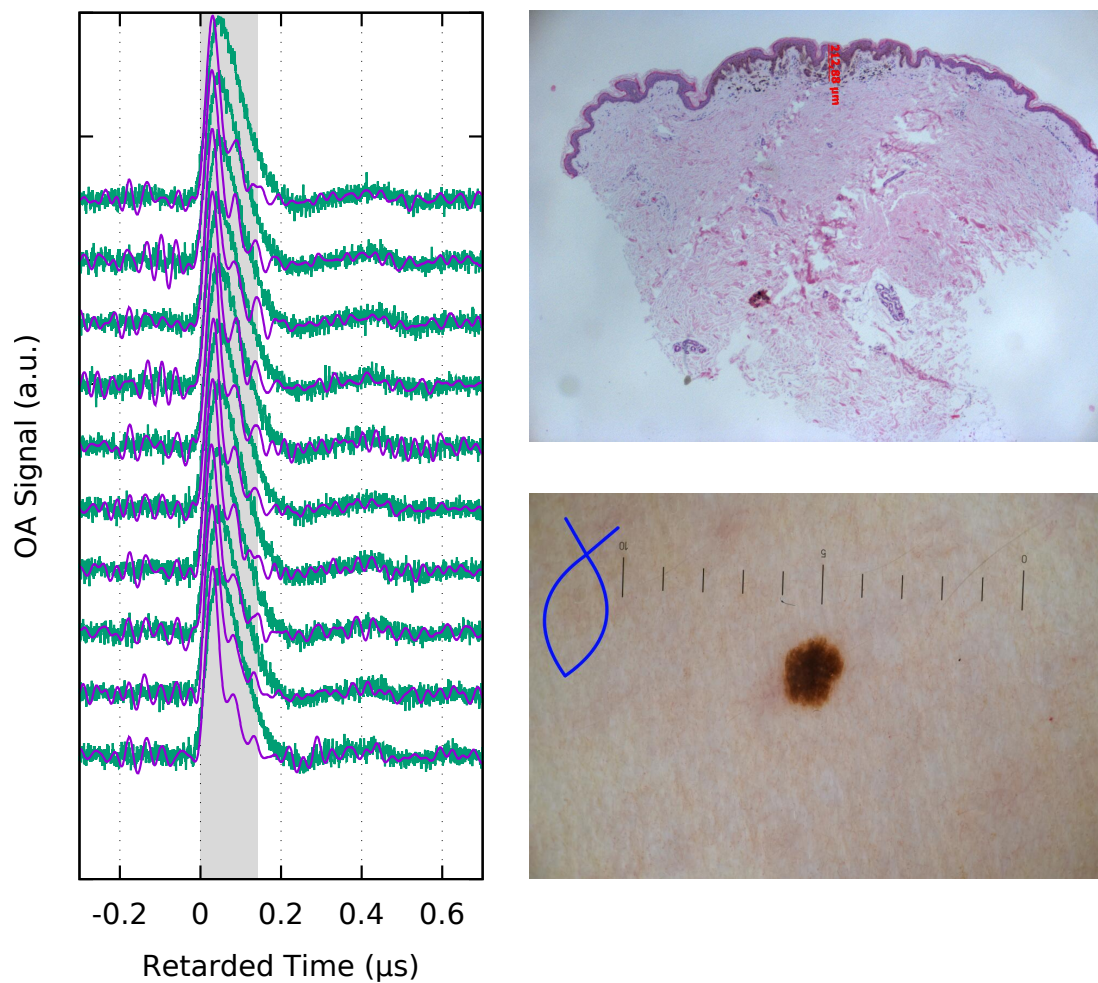


FIGURE A.18: W3-3-2-1. Discussed in detail in the results section. Histological thickness is 213 μm .

A.16 W3-3-2-2

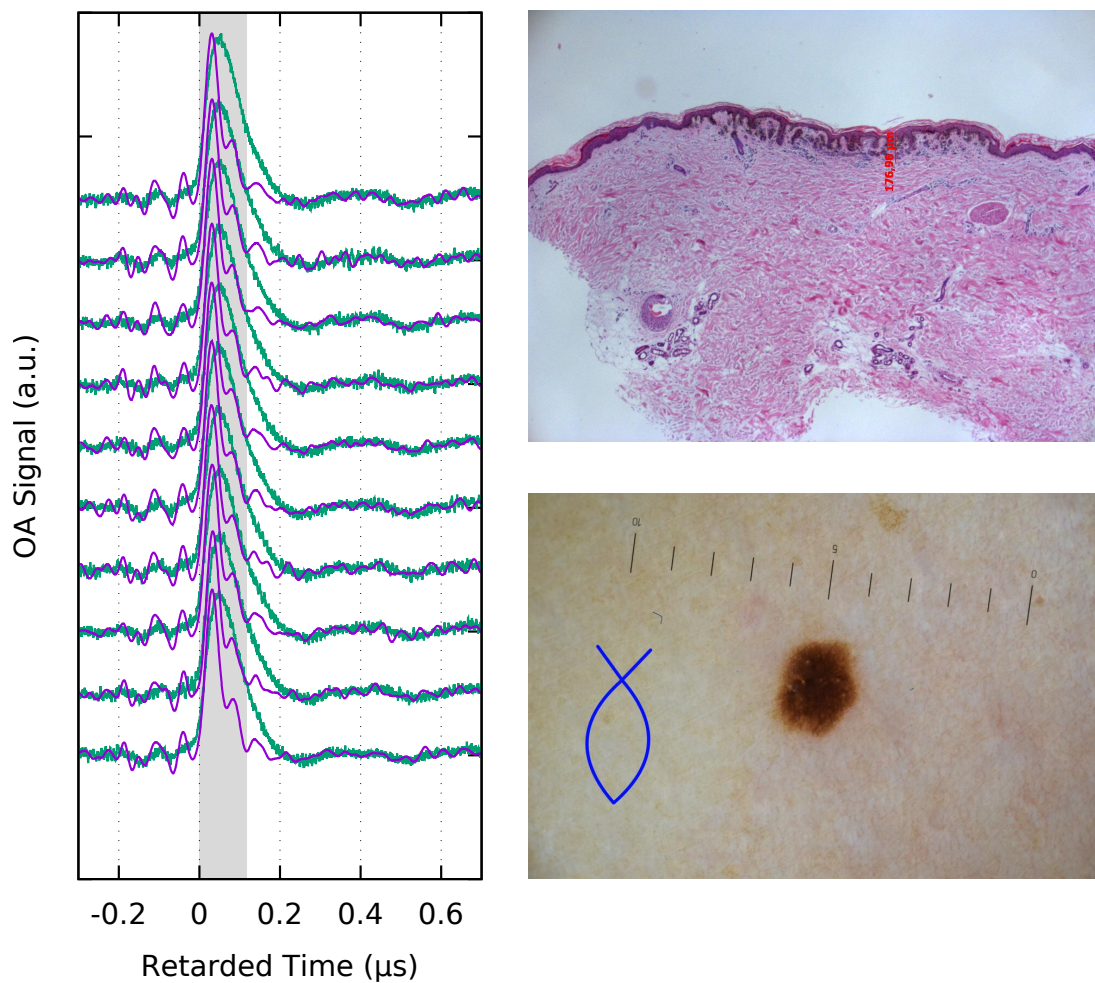


FIGURE A.19: W3-3-2-2. This lesion is similar to W3-3-2-1 which is discussed in detail in the results section. Histological thickness is 177 μm .

Appendix B

Appendix

B.1 Non Beer-Lambert Pressure Profiles

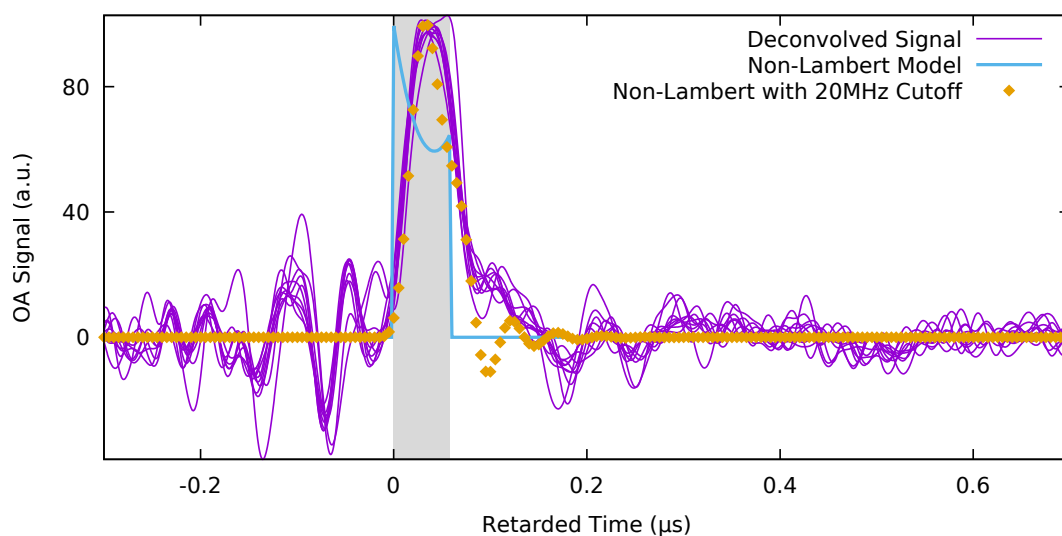


FIGURE B.1: Example of extended absorption profile, modelling additional irradiation form below.

The simplest OA sample, for nearfield measurements, is a single homogeneous absorber layer with a constant absorption coefficient, which is illuminated from one direction only. In that case, the pressure depth profile follows the Beer-Lambert law. Obviously, this is not likely to be the case in biologically grown structures such as melanocytic nevi. However, ethical concerns and medical necessities do not allow invasive testing on a nevus before or after the excision. Therefore, we are limited to two-dimensional slices of the histopathology, at the position of deepest penetration. It is not possible to

recreate the three-dimensional morphology of the absorber and approximations had to be made. In Section 5.4.2 a very thin nevus is presented, which increases the likelihood of the homogeneous absorber model to be valid. However, the small total absorption allows more light to reach the bottom of the nevus, which could be scattered into the absorbing layer from beneath. In this case the absorption profile becomes more complex. To showcase a possible profile, we assumed the illumination from below to behave like the one from above, only with less light and in the opposite direction. In Figure B.1, the Beer-Lambert profile of a single homogeneous absorbing layer with an absorption coefficient of 16 mm^{-1} is superposed with another Beer-Lambert profile from the bottom upwards with half of the intensity of the original profile.

B.2 Surface waves

When the illumination occurs through the detector it creates more than the OA signal of the investigated sample. One example is the pyroelectric effect which is discussed at several times throughout this thesis. By contrast, the OA signal from the detector film itself is not discussed. This is because its contribution is negligible, at least for the setups presented above. By facilitating the propagation of these OA transients as surface waves they can be detected.

To distinguish the pyroelectric signal created by the illumination of the detector itself from the surface waves created by the OA effect caused by the absorption in the detector film, a simple measurement setup was conceived. The detector film without fronting- or backing layer was mounted loosely on a plastic frame. That way OA surface waves could propagate unhindered through the polymer film.

A multimode fiber ($880 \mu\text{m}$ core diameter) was directed orthogonally at the detector film in a lateral distance of 3 mm to the active area. The fiber pointed at an area of uncoated PVDF, without ITO electrodes. While the lateral distance was constant the axial distance was changed in between measurements. Due to the diverging beam profile the illuminated area increased with distance. At a distance of 3 mm (red curve) the beam radius is not large enough to reach the detector. In that case one observes the electromagnetic noise from the Q-switched laser after the delay of approximately $1 \mu\text{s}$, followed by a small slope. Then follows a big dip leading a series of smaller oscillations.

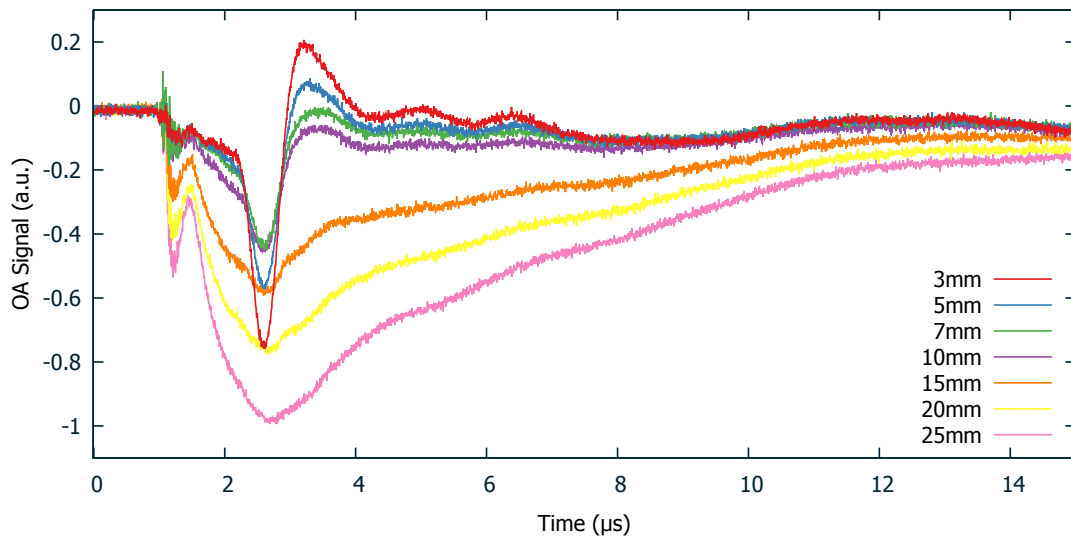


FIGURE B.2: Measurements of surface waves created by the absorption in the detector film. For all measurements the illumination fiber was placed at a lateral distance of 3 mm from the detector. The axial distances are listed in the legend. Amplitudes of surface waves decrease with axial distance. Pyroelectric signal and surface wave originating from the active area increase with axial distance.

This is the signal of the surface wave. With increasing distance, the surface wave dip decreases due to the smaller radiation density. At a distance of 3 mm only a small amount of stray light reaches the detector, which is visible in the small slope between 1 μ s and 2.5 μ s. This slope increases when more and more light reaches the detector area. At a distance of 15 mm the magnitude of the slope dominated the surface wave signal and over the whole time frame of 15 μ s we recognize the shape of the pyroelectric signal as presented in the main part of this thesis. In addition to the pyroelectric effect a smaller feature is visible at the beginning of the signal. This feature is the surface wave created by the OA effect in the active area.

By illuminating the detector directly, the absorbed energy is partly converted into OA pressure. For distances of more than 10 mm this feature is too large to be negligible and would be even larger if the illumination fiber would be placed directly above the active area. Fortunately, the pressure transients presented in Figure B.2 are surface waves. Thus, when the detector film is sandwiched in between acoustically better matched layers, i.e. fronting and backing layer, the OA signal from the detector itself almost vanishes. This can be seen in any measurement performed with the clinic detector setup. Presumably, if the OA pressure of the detector film can propagate in all three dimension it leaves the detector too fast to create a notable signal. Regarding the OA pressure

created in the detector film outside the detector itself, only a negligible fraction of the energy will travel along its surface to be detected.

In the master thesis of Jonas Kannengießer the properties of the detector film without fronting and backing layer are discussed in detail.

List of Figures

2.1	Diagram of OA generation	10
2.2	List of acoustic detection technologies	14
2.3	Schematic of the human skin. [WikiSkin]	18
2.4	Melanoma diagnoses in Germany 2005-2012	22
2.5	OCT image of a measurement standard with and without detector film.	23
2.6	Photograph of OA cart for clinical study	25
3.1	Sketch of model setup for near- and far field simulation	32
3.2	Near- and far field simulations	34
3.3	Influence of beam profile on OA signal	36
3.4	Beer-Lambert signal and Gibbs phenomenon	41
4.1	Process of PVA hydrogel preparation.	46
4.2	Photographs of PVA-H layers after freezing	47
4.3	Transmission spectra of PVDF detector film	49
4.4	Heckmann-diagram and piezoelectricity	50
4.5	Photograph of detector electrodes and sketch of sputter process	52
4.6	Microscopic view of active area	53
4.7	Geometry mapping of active area of OA detector	54
4.8	Photograph of the custom build preamplifier.	55
4.9	Layout of the circuit board for the preamplifier as used in this work.	56
4.10	Energy calibration	57
4.11	Photograph of the pyroelectric detector used to calibrate the system.	58
4.12	Beam profile after long fiber	59
4.13	Sketch of OA measurement setup	60
4.14	Sketch Angular study setup	61
4.15	Photograph of handheld clinical setup	63
4.16	Background signal subtraction	65
4.17	Removal of pyroelectric signal	66
5.1	Sketch of experimental setup for PVA-H layers	71
5.2	Far field OA signals of PVA-H layers	72
5.3	Sketch of Angular Study setup	74
5.4	Far field OA signals of Angular Study	75
5.5	Influence of parasitic capacity on pyroelectrical signal	76
5.6	Wavelength dependence of pyroelectric signal	78
5.7	Clinical setup, sketch and photograph	80
5.8	Deconvolution post-processing: plots of OA signal, IRF and simulation	82

5.9	Wavelength scan of mole	86
5.10	Overview of OA measurements from clinical study	89
5.11	Post-processed signal form W3-3-2-1 lesion including Beer-Lambert model	90
5.12	Histology and photograph of lesion W3-3-2-1	92
5.13	Post-processed signal of lesion W2-5-2	93
5.14	Photograph and histology of lesion W2-5-2	95
5.15	Post-processed signal of lesion W3-2-2-2	96
5.16	Photograph and histology of lesion W3-2-2-2	98
5.17	Post-processed signals of lesion W2-5-1	99
5.18	Photograph and histology of lesion W2-5-1	101
A.1	W2-2-1 Center	108
A.2	W2-2-1 Dark Spot	109
A.3	W2-2-2-1	110
A.4	W2-2-2-2	111
A.5	W2-3-1	112
A.6	W2-3-2	113
A.7	W2-4-1	114
A.8	W2-4-1	115
A.9	W2-4-2	116
A.10	W2-5-1	117
A.11	W2-5-1 Light Middle	118
A.12	W2-5-2	119
A.13	W3-2-1-1	120
A.14	W3-2-1-2	121
A.15	W3-2-2-1	122
A.16	W3-2-2-2	123
A.17	W3-3-1	124
A.18	W3-3-2-1	125
A.19	W3-3-2-2	126
B.1	Non Beer-Lambert pressure profile	127
B.2	Surface waves	129

Bibliography

- [Aga11] Pierre G. Agache and Philippe Humbert. *Measuring the skin. Non-invasive investigations, physiology, normal constants*. Translated from the French. Berlin and London: Springer, 2011. 1 volume. ISBN: 978-3-642-05691-8.
- [Bac82] D. R. Bacon. “Characteristics of a PVDF Membrane Hydrophone for Use in the Range 1-100 MHz”. In: *IEEE Transactions on Sonics and Ultrasonics* 29 (1 1982), pp. 18–25. ISSN: 0018-9537. DOI: 10.1109/T-SU.1982.31298.
- [Baer09] Günter Bärwolff and Gottfried Seifert. *Höhere Mathematik für Naturwissenschaftler und Ingenieure*. 2. Aufl., korr. Nachdr. Berlin: Springer, 2009. XIII, 970 Seiten. ISBN: 978-3827416889.
- [Bal01] C. M. Balch et al. “Final version of the American Joint Committee on Cancer staging system for cutaneous melanoma”. eng. In: *Journal of clinical oncology : official journal of the American Society of Clinical Oncology* 19 (16 2001). Consensus Development Conference Journal Article Research Support, Non-U.S. Gov’t Review, pp. 3635–3648. DOI: 10.1200/JCO.2001.19.16.3635. eprint: 11504745.
- [Bar14] Barmer GEK. *Durchschnittliche Anzahl von bösartigen in-situ-Neubildungen in Deutschland nach Geschlecht in den Jahren von 2005 bis 2012 (je 100.000 Einwohner)*. 2014. URL: <https://de.statista.com/statistik/daten/studie/291144/umfrage/anzahl-von-boesartigen-in-situ-neubildungen-in-deutschland-nach-geschlecht/> (visited on 10/06/2016).
- [Bas00] Alexey N. Bashkatov et al. In: *EOS/SPIE European Biomedical Optics Week*. (Amsterdam, Netherlands). Ed. by Valery V. Tuchin. SPIE Proceedings. SPIE, 2000, pp. 219–226. DOI: 10.1117/12.405946.

- [Blu16] E. Blumenrother et al. “Detection, numerical simulation and approximate inversion of optoacoustic signals generated in multi-layered PVA hydrogel based tissue phantoms”. eng. In: *Photoacoustics* 4 (4 2016). Journal Article, pp. 125–132. ISSN: 22135979. DOI: 10.1016/j.pacs.2016.10.002. eprint: 27833857.
- [Blu19] Elias Blumenröther et al. “Single Transparent Piezoelectric Detector for Optoacoustic Sensing-Design and Signal Processing”. eng. In: *Sensors (Basel, Switzerland)* 19 (9 2019). Journal Article. ISSN: 1424-8220. DOI: 10.3390/s19092195. eprint: 31083637.
- [Bra18] Freddie Bray et al. “Global cancer statistics 2018. GLOBOCAN estimates of incidence and mortality worldwide for 36 cancers in 185 countries”. eng. In: *CA: A Cancer Journal for Clinicians* 68 (6 2018). Journal Article, pp. 394–424. ISSN: 0007-9235. DOI: 10.3322/caac.21492. eprint: 30207593. (Visited on 04/06/2020).
- [Bre70] A. Breslow. “Thickness, cross-sectional areas and depth of invasion in the prognosis of cutaneous melanoma”. eng. In: *Annals of surgery* 172 (5 1970). PMC1397358 Journal Article, pp. 902–908. ISSN: 0003-4932. eprint: 5477666.
- [Bre90] Leonid M. Brekhovskikh and Oleg A. Godin. *Acoustics of Layered Media I. Plane and Quasi-Plane Waves*. eng. Vol. 5. Springer Series on Wave Phenomena. Berlin and Heidelberg: Springer, 1990. 240 pp. ISBN: 9783540647249. DOI: 10.1007/978-3-642-52369-4. URL: <http://dx.doi.org/10.1007/978-3-642-52369-4>.
- [Bue10] Andreas Buehler et al. “Video rate optoacoustic tomography of mouse kidney perfusion”. In: *Optics Letters* 35 (14 2010), p. 2475. ISSN: 0146-9592. DOI: 10.1364/OL.35.002475.
- [Bur07] Peter Burgholzer et al. “Exact and approximative imaging methods for photoacoustic tomography using an arbitrary detection surface”. eng. In: *Physical review. E, Statistical, nonlinear, and soft matter physics* 75 (4 Pt 2 2007). Journal Article, p. 046706. ISSN: 1539-3755. DOI: 10.1103/PhysRevE.75.046706. eprint: 17501015.

- [Cal05] G. Caliano et al. “Design, fabrication and characterization of a capacitive micromachined ultrasonic probe for medical imaging”. In: *IEEE Transactions on Ultrasonics, Ferroelectrics and Frequency Control* 52 (12 2005), pp. 2259–2269. ISSN: 0885-3010. DOI: 10.1109/TUFFC.2005.1563268. (Visited on 11/23/2017).
- [Cho15] Bernard Choi et al. “Assessment of cutaneous melanoma and pigmented skin lesions with photoacoustic imaging”. In: *SPIE BiOS*. (San Francisco, California, United States). SPIE Proceedings. SPIE, 2015, p. 930303. DOI: 10.1117/12.2078309.
- [Cos07] Gertrude-E Costin and Vincent J. Hearing. “Human skin pigmentation: melanocytes modulate skin color in response to stress”. eng. In: *FASEB journal : official publication of the Federation of American Societies for Experimental Biology* 21 (4 2007). Journal Article Research Support, N.I.H., Intramural Review, pp. 976–994. ISSN: 1530-6860. DOI: 10.1096/fj.06-6649rev. eprint: 17242160.
- [Dea12] X. Luís Deán-Ben et al. “Accurate model-based reconstruction algorithm for three-dimensional optoacoustic tomography”. eng. In: *IEEE transactions on medical imaging* 31 (10 2012). Journal Article Research Support, Non-U.S. Gov’t, pp. 1922–1928. DOI: 10.1109/TMI.2012.2208471. eprint: 23033065.
- [Deá13] X. Luís Deán-Ben and Daniel Razansky. “Portable spherical array probe for volumetric real-time optoacoustic imaging at centimeter-scale depths”. In: *Optics Express* 21 (23 2013), p. 28062. ISSN: 1094-4087. DOI: 10.1364/OE.21.028062.
- [Dem07] Wolfgang Demtröder. *Laserspektroskopie. Grundlagen und Techniken*. 5., erw. und Neubearb. Aufl. Berlin: Springer, 2007. XV, 726 Seiten. ISBN: 978-3-540-33792-8.
- [Don14] Biqin Dong et al. “Photoacoustic probe using a microring resonator ultrasonic sensor for endoscopic applications”. eng. In: *Optics letters* 39 (15 2014). PMC4560527 Journal Article Research Support, N.I.H., Extramural Research Support, U.S. Gov’t, Non-P.H.S., pp. 4372–4375. ISSN: 1539-4794. eprint: 25078180.

- [Dre04] Detlev Drenckhahn, ed. *Herz-Kreislauf-System, lymphatisches System, endokrines System, Nervensystem, Sinnesorgane, Haut*. 16., völlig neu bearb. Aufl. Vol. 2. Anatomie. Drenckhahn, Detlev, (Hrsg.) München [u.a.]: Urban & Schwarzenberg, 2004. XII, 876 S. ISBN: 3-437-42350-9.
- [Fri85] R. J. Friedman, D. S. Rigel, and A. W. Kopf. "Early Detection of Malignant Melanoma. The Role of Physician Examination and Self-Examination of the Skin". In: *CA: A Cancer Journal for Clinicians* 35 (3 1985), pp. 130–151. ISSN: 0007-9235. DOI: 10.3322/canjclin.35.3.130. (Visited on 10/27/2017).
- [Gie86] K. Giese et al. "Photoacoustic in vivo study of the penetration of sunscreen into human skin". In: *Canadian Journal of Physics* 64 (9 1986), pp. 1139–1141. ISSN: 0008-4204. DOI: 10.1139/p86-197.
- [Gor13] Myron Gordon. *Pigment Cell Biology. Proceedings of the Fourth Conference on the Biology of Normal and Atypical Pigment Cell Growth*. Burlington: Elsevier Science, 2013. 1 online resource (678). ISBN: 9781483274423.
- [Gra02] C. G. Granqvist and A. Hultner. "Transparent and conducting ITO films. New developments and applications". In: *Thin Solid Films* 411 (1 2002), pp. 1–5. ISSN: 00406090. DOI: 10.1016/S0040-6090(02)00163-3.
- [Gui08] P. Guitera et al. "Melanoma histological Breslow thickness predicted by 75-MHz ultrasonography". eng. In: *The British journal of dermatology* 159 (2 2008). Evaluation Studies Journal Article, pp. 364–369. ISSN: 1365-2133. DOI: 10.1111/j.1365-2133.2008.08681.x. eprint: 18565186.
- [Gus93] V. È. Gusev and A. A. Karabutov. *Laser optoacoustics*. eng rus. New York, N.Y.: American Institute of Physics, 1993. ISBN: 978-1563960369.
- [Hai14] Pengfei Hai et al. "Near-infrared optical-resolution photoacoustic microscopy". eng. In: *Optics letters* 39 (17 2014). Journal Article, pp. 5192–5195. ISSN: 1539-4794. DOI: 10.1364/OL.39.005192. eprint: 25166107.
- [Haj15] Parsin Hajireza et al. "In vivo optical resolution photoacoustic microscopy using glancing angle-deposited nanostructured Fabry–Perot etalons". In: *Optics Letters* 40 (7 2015), p. 1350. ISSN: 0146-9592. DOI: 10.1364/OL.40.001350.

- [Has00] Akihiro Abe et al., eds. *Biopolymers · PVA Hydrogels, Anionic Polymerisation Nanocomposites*. Vol. 153. Advances in Polymer Science. Berlin, Heidelberg: Springer Berlin Heidelberg, 2000. 1 online resource (x, 221. ISBN: 978-3-540-46414-3. DOI: 10.1007/3-540-46414-X_2.
- [Her12] Cila Herman. “Emerging technologies for the detection of melanoma. Achieving better outcomes”. eng. In: *Clinical, cosmetic and investigational dermatology* 5 (2012). PMC3508547 Journal Article, pp. 195–212. ISSN: 1178-7015. DOI: 10.2147/CCID.S27902. eprint: 23204850.
- [Hou15] Yi Hou et al. “Preparation of PVA hydrogel with high-transparence and investigations of its transparent mechanism”. In: *RSC Adv* 5 (31 2015), pp. 24023–24030. ISSN: 2046-2069. DOI: 10.1039/C5RA01280E.
- [Int14] International Agency for Research on Cancer and World Health Organization. *World cancer report 2014*. Stewart, Bernard W, (editor.) Wild, Chris, (editor.) Lyon France and Geneva Switzerland: International Agency for Research on Cancer and WHO Press World Health Organization, 2014. xiv, 630 pages. ISBN: 9789283204299.
- [Jac91] Steven L. Jacques and Daniel J. McAuliffe. “THE MELANOSOME. THRESHOLD TEMPERATURE FOR EXPLOSIVE VAPORIZATION AND INTERNAL ABSORPTION COEFFICIENT DURING PULSED LASER IRRADIATION”. In: *Photochemistry and photobiology* 53 (6 1991), pp. 769–775. ISSN: 1751-1097. DOI: 10.1111/j.1751-1097.1991.tb09891.x.
- [Jac98] Steven L. Jacques. *Skin Optics Summary*. 26.06.2014. URL: <http://omlc.org/news/jan98/skinoptics.html> (visited on 04/09/2015).
- [Jae05] Michael Jaeger et al. “Diffraction-free acoustic detection for optoacoustic depth profiling of tissue using an optically transparent polyvinylidene fluoride pressure transducer operated in backward and forward mode”. eng. In: *Journal of biomedical optics* 10 (2 2005). Journal Article Research Support, Non-U.S. Gov't, p. 024035. ISSN: 1083-3668. DOI: 10.1117/1.1891443. eprint: 15910108.
- [Jon16] Jonas Kanngießer. “Pyro- und piezoelektrische Antwort dünner PVDF-Folien auf kurze Laserpulse”. Hannoverschen Zentrum für optische Technologien. Masterarbeit. Hannover: Leibniz Universität Hannover, 2016-09-27.

- [Kar12] Aletta E. Karsten and Jacoba E. Smit. “Modeling and verification of melanin concentration on human skin type”. eng. In: *Photochemistry and photobiology* 88 (2 2012). Journal Article Research Support, Non-U.S. Gov’t, pp. 469–474. ISSN: 1751-1097. DOI: 10.1111/j.1751-1097.2011.01044.x. eprint: 22077284.
- [Kar84] A. Karbach, J. Röper, and P. Hess. “Computer-controlled performance of photoacoustic resonance experiments”. In: *Review of Scientific Instruments* 55 (6 1984), p. 892. ISSN: 00346748. DOI: 10.1063/1.1137860.
- [Kar96] A. Karabutov, N. B. Podymova, and V. S. Letokhov. “Time-resolved laser optoacoustic tomography of inhomogeneous media”. In: *Applied Physics B Laser and Optics* 63 (6 1996), pp. 545–563. ISSN: 0946-2171. DOI: 10.1007/BF01830994.
- [Kha03] Alexei Kharine et al. “Poly(vinyl alcohol) gels for use as tissue phantoms in photoacoustic mammography”. In: *Physics in Medicine and Biology* 48 (3 2003), pp. 357–370. ISSN: 0031-9155. DOI: 10.1088/0031-9155/48/3/306.
- [Kim99] H. Kim et al. “Electrical, optical, and structural properties of indium–tin–oxide thin films for organic light-emitting devices”. In: *Journal of Applied Physics* 86 (11 1999), p. 6451. ISSN: 00218979. DOI: 10.1063/1.371708. URL: <http://scitation.aip.org/docserver/fulltext/aip/journal/jap/86/11/1.371708.pdf?expires=1469005892&id=id&accname=2121141&checksum=C22841AF9C5816D1D93901F2DD4BBE50> (visited on 07/20/2016).
- [Kre10] Ronald Krebs. “Entwicklung eines optoakustischen Verfahrens zur Bestimmung der optischen Eigenschaften von menschlicher Haut in vivo mittels eines probabilistischen Ansatzes nach Bayes”. 2010. 231 pp.
- [Li14] Chiye Li et al. “Urogenital photoacoustic endoscope”. In: *Optics Letters* 39 (6 2014), p. 1473. ISSN: 0146-9592. DOI: 10.1364/OL.39.001473.
- [Li14] Hao Li et al. “A transparent broadband ultrasonic detector based on an optical micro-ring resonator for photoacoustic microscopy”. eng. In: *Scientific reports* 4 (2014). Journal Article Research Support, N.I.H., Extramural Research Support, U.S. Gov’t, Non-P.H.S., p. 4496. ISSN: 2045-2322. DOI: 10.1038/srep04496. eprint: 24675547.

- [Li14] Lei Li et al. “Fully motorized optical-resolution photoacoustic microscopy”. In: *Optics Letters* 39 (7 2014), p. 2117. ISSN: 0146-9592. DOI: 10.1364/OL.39.002117.
- [Lin07] Jennifer Y. Lin and David E. Fisher. “Melanocyte biology and skin pigmentation”. eng. In: *Nature* 445 (7130 2007). Journal Article Research Support, N.I.H., Extramural Research Support, Non-U.S. Gov’t Review, pp. 843–850. ISSN: 1476-4687. DOI: 10.1038/nature05660. eprint: 17314970.
- [Lis12] Tom Lister, Philip A. Wright, and Paul H. Chappell. “Optical properties of human skin”. eng. In: *Journal of biomedical optics* 17 (9 2012). Journal Article Review, pp. 90901–1. ISSN: 1560-2281. DOI: 10.1117/1.JBO.17.9.090901.
- [Loh98] Stefan Lohmann. “Optoakustische Tomographie mit laserinduziertem Ultraschall in der medizinischen Diagnostik”. PHD. 1998. 192 pp.
- [Lut13] Christian Lutzweiler and Daniel Razansky. “Optoacoustic Imaging and Tomography: Reconstruction Approaches and Outstanding Challenges in Image Performance and Quantification”. In: *Sensors* 13 (6 2013), pp. 7345–7384. ISSN: 1424-8220. DOI: 10.3390/s130607345.
- [Mac11] Machet, L., Samimi, M., Georgesco, G., Mourtada, Y., Naouri, M., Grégoire, J. M. *High Resolution Ultrasound Imaging of Melanocytic and Other Pigmented Lesions of the Skin*. Tanabe, Masayuki, (editor.) Rijeka, Croatia: InTech, 2011. 1 online resource (210. ISBN: 978-953-307-239-5.
- [Mag77] Knut Magnus. “Prognosis in malignant melanoma of the skin. Significance of stage of disease, anatomical site, sex, age and period of diagnosis”. In: *Cancer* 40 (1 1977), pp. 389–397. DOI: 10.1002/1097-0142(197707)40:1<389::AID-CNCR2820400155>3.0.CO;2-I.
- [Man16] Srirang Manohar and Daniel Razansky. “Photoacoustics. A historical review”. In: *Advances in Optics and Photonics* 8 (4 2016), p. 586. ISSN: 1943-8206. DOI: 10.1364/AOP.8.000586. (Visited on 09/19/2017).
- [Man84] Andreas Mandelis. “Frequency-domain photopyroelectric spectroscopy of condensed phases (PPES). A new, simple and powerful spectroscopic technique”. In: *Chemical Physics Letters* 108 (4 1984), pp. 388–392. ISSN: 00092614. DOI: 10.1016/0009-2614(84)85212-4. (Visited on 12/04/2017).

- [Mat14] Scott P. Mattison and Brian E. Applegate. “Simplified method for ultra high-resolution photoacoustic microscopy via transient absorption”. In: *Optics Letters* 39 (15 2014), p. 4474. ISSN: 0146-9592. DOI: 10.1364/OL.39.004474.
- [Maz10] Alida Mazzoli, Roberto Munaretto, and Lorenzo Scalise. “Preliminary results on the use of a noninvasive instrument for the evaluation of the depth of pigmented skin lesions. Numerical simulations and experimental measurements”. eng. In: *Lasers in medical science* 25 (3 2010). Evaluation Studies Journal Article Validation Studies, pp. 403–410. ISSN: 0268-8921. DOI: 10.1007/s10103-009-0724-x. eprint: 19763669.
- [Mel] O. Melchert et al. *Detection and numerical simulation of optoacoustic near- and farfield signals observed in PVA hydrogel phantoms*. 18 pages, 5 figures. URL: <http://arxiv.org/pdf/1702.07603v1>.
- [Mor95] C. M. Moran, N. L. Bush, and J. C. Bamber. “Ultrasonic propagation properties of excised human skin”. In: *Ultrasound in Medicine & Biology* 21 (9 1995), pp. 1177–1190. ISSN: 03015629. DOI: 10.1016/0301-5629(95)00049-6.
- [Nie05] J. J. Niederhauser et al. “Transparent ITO coated PVDF transducer for optoacoustic depth profiling”. In: *Optics Communications* 253 (4-6 2005), pp. 401–406. ISSN: 00304018. DOI: 10.1016/j.optcom.2005.05.005.
- [Nin15] Bo Ning et al. “Simultaneous photoacoustic microscopy of microvascular anatomy, oxygen saturation, and blood flow”. eng. In: *Optics letters* 40 (6 2015). Journal Article, pp. 910–913. ISSN: 1539-4794. DOI: 10.1364/OL.40.000910. eprint: 25768144.
- [Oh06] Jung-Taek Oh et al. “Three-dimensional imaging of skin melanoma in vivo by dual-wavelength photoacoustic microscopy”. eng. In: *Journal of biomedical optics* 11 (3 2006). Evaluation Studies Journal Article Research Support, N.I.H., Extramural Research Support, Non-U.S. Gov’t, p. 34032. ISSN: 1083-3668. DOI: 10.1117/1.2210907. eprint: 16822081.
- [Oma13] Murad Omar, Jérôme Gateau, and Vasilis Ntziachristos. “Raster-scan optoacoustic mesoscopy in the 25-125 MHz range”. eng. In: *Optics letters* 38

- (14 2013). Journal Article, pp. 2472–2474. ISSN: 1539-4794. DOI: 10.1364/OL.38.002472. eprint: 23939084.
- [Oma14] Murad Omar et al. “Ultrawideband reflection-mode optoacoustic mesoscopy”. In: *Optics Letters* 39 (13 2014), p. 3911. ISSN: 0146-9592. DOI: 10.1364/OL.39.003911.
- [Ome02] O. Oralkan et al. “Capacitive micromachined ultrasonic transducers. Next-generation arrays for acoustic imaging?” In: *IEEE transactions on ultrasonics, ferroelectrics, and frequency control* 49 (11 2002), pp. 1596–1610. ISSN: 0885-3010. DOI: 10.1109/TUFFC.2002.1049742. (Visited on 11/23/2017).
- [Ora06] Alexander Oraevsky et al. “In vivo testing of laser optoacoustic system for image-guided biopsy of prostate”. In: *Biomedical Optics 2006*. (San Jose, CA). Ed. by Alexander A. Oraevsky and Lihong V. Wang. SPIE Proceedings. SPIE, 2006, 60860B. DOI: 10.1117/12.658295. (Visited on 07/21/2017).
- [Pal00] G. Paltauf and H. Schmidt-Kloiber. “Pulsed optoacoustic characterization of layered media”. In: *Journal of Applied Physics* 88 (3 2000), p. 1624. ISSN: 00218979. DOI: 10.1063/1.373863.
- [Pal09] G. Paltauf, R. Nuster, and P. Burgholzer. “Characterization of integrating ultrasound detectors for photoacoustic tomography”. In: *Journal of Applied Physics* 105 (10 2009), p. 102026. ISSN: 00218979. DOI: 10.1063/1.3116133.
- [Pel07] Giovanni Pellacani et al. “The impact of in vivo reflectance confocal microscopy for the diagnostic accuracy of melanoma and equivocal melanocytic lesions”. eng. In: *The Journal of investigative dermatology* 127 (12 2007). Journal Article Research Support, Non-U.S. Gov’t, pp. 2759–2765. ISSN: 0022-202X. DOI: 10.1038/sj.jid.5700993. eprint: 17657243. (Visited on 12/01/2017).
- [Qi17] Weizhi Qi et al. “Inverted multiscale optical resolution photoacoustic microscopy”. eng. In: *Journal of biophotonics* 10 (12 2017). Journal Article, pp. 1580–1585. ISSN: 1864-0648. DOI: 10.1002/jbio.201600246. eprint: 28128537. (Visited on 01/04/2018).

- [Raj95] Milind Rajadhyaksha et al. “In Vivo Confocal Scanning Laser Microscopy of Human Skin. Melanin Provides Strong Contrast”. In: *Journal of Investigative Dermatology* 104 (6 1995), pp. 946–952. ISSN: 0022202X. DOI: 10.1111/1523-1747.ep12606215. (Visited on 12/01/2017).
- [Raj99] M. Rajadhyaksha et al. “In vivo confocal scanning laser microscopy of human skin II. Advances in instrumentation and comparison with histology”. eng. In: *The Journal of investigative dermatology* 113 (3 1999). Comparative Study Journal Article Research Support, Non-U.S. Gov’t Research Support, U.S. Gov’t, Non-P.H.S. Research Support, U.S. Gov’t, P.H.S., pp. 293–303. ISSN: 0022-202X. DOI: 10.1046/j.1523-1747.1999.00690.x. eprint: 10469324. (Visited on 12/07/2017).
- [Rig05] Darrell S. Rigel et al. “ABCDE—an evolving concept in the early detection of melanoma”. eng. In: *Archives of dermatology* 141 (8 2005). Comment Editorial, pp. 1032–1034. DOI: 10.1001/archderm.141.8.1032. eprint: 16103334.
- [Rob15] Robert Koch-Institut. “Krebs in Deutschland 2011/2012. Gesundheitsberichterstattung des Bundes. 10. Ausg. 2015”. ger. In: (2015). DOI: 10.17886/rkipubl-2015-004. URL: <http://edoc.rki.de/docviews/abstract.php?id=4119>.
- [Rub10] Krista M. Rubin. “Melanoma Staging”. In: *Journal of the Dermatology Nurses’ Association* 2 (6 2010), pp. 254–259. ISSN: 1945-760X. DOI: 10.1097/JDN.0b013e3181ffa393.
- [San16] Javier Sánchez-Monedero et al. “Classification of Melanoma Presence and Thickness Based on Computational Image Analysis”. In: 9648 (), pp. 427–438. DOI: 10.1007/978-3-319-32034-2_36.
- [Smi11] Jacoba E. Smit, Anne F. Grobler, and Raymond W. Sparrow. “Influence of variation in eumelanin content on absorbance spectra of liquid skin-like phantoms”. eng. In: *Photochemistry and photobiology* 87 (1 2011). Journal Article Research Support, Non-U.S. Gov’t, pp. 64–71. ISSN: 1751-1097. DOI: 10.1111/j.1751-1097.2010.00824.x. eprint: 21073475.

- [Smi79] S. W. Smith et al. “Angular Response of Piezoelectric Elements in Phased Array Ultrasound Scanners”. In: *IEEE Transactions on Sonics and Ultrasonics* 26 (3 1979), pp. 185–190. ISSN: 0018-9537. DOI: 10.1109/T-SU.1979.31085.
- [Suh05] Eun-Jung Suh, Young-Ah Woo, and Hyo-Jin Kim. “Determination of water content in skin by using a ft near infrared spectrometer”. In: *Archives of Pharmacal Research* 28 (4 2005), pp. 458–462. ISSN: 0253-6269. DOI: 10.1007/BF02977676.
- [Tam86] Andrew C. Tam. “Applications of photoacoustic sensing techniques”. In: *Reviews of Modern Physics* 58 (2 1986), pp. 381–431. ISSN: 0034-6861. DOI: 10.1103/RevModPhys.58.381.
- [Tar15] Adrian Taruttis and Vasilis Ntziachristos. “Advances in real-time multispectral optoacoustic imaging and its applications”. In: *Nature Photonics* 9 (4 2015), pp. 219–227. ISSN: 1749-4885. DOI: 10.1038/nphoton.2015.29. (Visited on 07/21/2017).
- [Tia11] He Tian et al. “Transparent, flexible, ultrathin sound source devices using Indium Tin oxide films”. In: *Applied Physics Letters* 99 (4 2011), p. 043503. ISSN: 00036951. DOI: 10.1063/1.3617462.
- [Tzo16] Stratis Tzoumas et al. “Eigenspectra optoacoustic tomography achieves quantitative blood oxygenation imaging deep in tissues”. eng. In: *Nature communications* 7 (2016). PMC4931322 Journal Article, p. 12121. ISSN: 2041-1723. DOI: 10.1038/ncomms12121. eprint: 27358000. (Visited on 07/21/2017).
- [Upp17] Paul Kumar Upputuri and Manojit Pramanik. “Recent advances toward preclinical and clinical translation of photoacoustic tomography. A review”. eng. In: *Journal of biomedical optics* 22 (4 2017). Journal Article, p. 41006. ISSN: 1083-3668. DOI: 10.1117/1.JBO.22.4.041006. eprint: 27893078. (Visited on 11/17/2017).
- [Vai09] Srikant Vaithilingam et al. “Three-dimensional photoacoustic imaging using a two-dimensional CMUT array”. eng. In: *IEEE transactions on ultrasonics, ferroelectrics, and frequency control* 56 (11 2009). Journal Article Research Support, N.I.H., Extramural Research Support, Non-U.S. Gov’t Research

- Support, U.S. Gov't, Non-P.H.S., pp. 2411–2419. ISSN: 0885-3010. DOI: 10.1109/TUFFc.2009.1329. eprint: 19942528. (Visited on 11/23/2017).
- [Var17] Arthur Varkentin et al. “Comparative study of presurgical skin infiltration depth measurements of melanocytic lesions with OCT and high frequency ultrasound”. eng. In: *Journal of biophotonics* 10 (6-7 2017). Journal Article, pp. 854–861. ISSN: 1864-0648. DOI: 10.1002/jbio.201600139. eprint: 28009131.
- [Wan08] Lihong V. Wang. “Photoacoustic Tomography and Microscopy”. In: *Optics and Photonics News* 19 (August 2008), pp. 36–41.
- [Wan09] Lihong V. Wang. “Multiscale photoacoustic microscopy and computed tomography”. In: *Nature photonics* 3 (9 2009), pp. 503–509. DOI: 10.1038/nphoton.2009.157.
- [Wan11] Tianyi Wang, Jinze Qiu, and Thomas E. “Determination of Melanoma Lateral and Depth Margins: Potential for Treatment Planning and Five-Year Survival Rate”. In: *In Tech*. DOI: 10.5772/26697. URL: <http://www.intechopen.com/books/skin-canceroverview/>.
- [Wan12] Lihong V. Wang and Song Hu. “Photoacoustic tomography: in vivo imaging from organelles to organs”. In: *Science (New York, N. Y.)* 335 (6075 2012), pp. 1458–1462. DOI: 10.1126/science.1216210.
- [War88] Ronald R. Warner, Mark C. Myers, and Dennis A. Taylor. “Electron Probe Analysis of Human Skin: Determination of the Water Concentration Profile”. In: *Journal of Investigative Dermatology* 90 (2 1988), pp. 218–224. ISSN: 0022202X. DOI: 10.1111/1523-1747.ep12462252.
- [Wat81] K. P. Watts et al. “Melanin content of hamster tissues, human tissues, and various melanomas”. eng. In: *Cancer research* 41 (2 1981). Journal Article Research Support, U.S. Gov't, Non-P.H.S. Research Support, U.S. Gov't, P.H.S., pp. 467–472. ISSN: 0008-5472. eprint: 7448793.
- [WikiSkin] Wikipedia: Madhero88 and M.Komorniczak. URL: https://en.wikipedia.org/wiki/File:Skin_layers.png.
- [Win11] Thomas Winkler. “Weisslicht mit einstellbarer Farbtemperatur auf Basis gestapelter und separat ansteuerbarer OLEDs. Sputteranlage ab Seite 32”. 155 pp.

- [Wol06] Merve Wollweber. “Optoacoustic Characterization of Optical Properties of Human Skin in Vivo in the Ultraviolet Wavelength Range. skin phototypes, uv-adaptations and effects of sunscreen”. 2006. 168 pp.
- [Wol14] Merve Meinhardt-Wollweber et al. “Tissue phantoms for multimodal approaches: Raman spectroscopy and optoacoustics”. In: *SPIE BiOS*. (San Francisco, California, United States). SPIE Proceedings. SPIE, 2014, 89450B. DOI: 10.1117/12.2038354.
- [Xia13] Wenfeng Xia et al. “Design and evaluation of a laboratory prototype system for 3D photoacoustic full breast tomography”. In: *Biomedical Optics Express* 4 (11 2013), p. 2555. ISSN: 2156-7085. DOI: 10.1364/BOE.4.002555.
- [Xia13c] Wenfeng Xia et al. “An optimized ultrasound detector for photoacoustic breast tomography”. In: *Medical Physics* 40 (3 2013), p. 032901. ISSN: 00942405. DOI: 10.1118/1.4792462.
- [Yan14] Zhenyuan Yang et al. “Multi-parametric quantitative microvascular imaging with optical-resolution photoacoustic microscopy in vivo”. In: *Optics Express* 22 (2 2014), p. 1500. ISSN: 1094-4087. DOI: 10.1364/OE.22.001500.
- [Yao13] Junjie Yao and Lihong V. Wang. “Photoacoustic microscopy”. In: *Laser & Photonics Reviews* 7 (5 2013), pp. 758–778. ISSN: 18638880. DOI: 10.1002/lpor.201200060.
- [Zha06] Hao F. Zhang et al. “Functional photoacoustic microscopy for high-resolution and noninvasive in vivo imaging”. In: *Nature Biotechnology* 24 (7 2006), pp. 848–851. ISSN: 1087-0156. DOI: 10.1038/nbt1220.
- [Zha08] Edward Zhang, Jan Laufer, and Paul Beard. “Backward-mode multiwavelength photoacoustic scanner using a planar Fabry-Perot polymer film ultrasound sensor for high-resolution three-dimensional imaging of biological tissues”. In: *Applied Optics* 47 (4 2008), p. 561. ISSN: 0003-6935. DOI: 10.1364/AO.47.000561. URL: [ao-47-4-561.pdf](#) (visited on 07/22/2015).
- [Zha11] Edward Z. Zhang et al. “Multimodal photoacoustic and optical coherence tomography scanner using an all optical detection scheme for 3D morphological skin imaging”. In: *Biomedical Optics Express* 2 (8 2011), p. 2202. ISSN: 2156-7085. DOI: 10.1364/BOE.2.002202.

- [Zho14] Yong Zhou et al. “Handheld photoacoustic microscopy to detect melanoma depth in vivo”. ENG. In: *Optics letters* 39 (16 2014). JOURNAL ARTICLE, pp. 4731–4734. ISSN: 1539-4794. DOI: 10.1364/OL.39.004731. eprint: 25121860.
- [Zho15] Yong Zhou et al. “Handheld photoacoustic probe to detect both melanoma depth and volume at high speed in vivo”. eng. In: *Journal of biophotonics* 8 (11-12 2015). Journal Article Research Support, N.I.H., Extramural Research Support, Non-U.S. Gov’t, pp. 961–967. ISSN: 1864-0648. DOI: 10.1002/jbio.201400143. eprint: 25676898.